2023

Experimental and theoretical studies of fluid-solid coupling processes of tight rock media

Tao Zhang

Experimental and theoretical studies of fluid-solid coupling processes of tight rock media

by

TAO ZHANG

DISSERTATION

Submitted in partial fulfilment of the requirements

for the degree of Doctor of Philosophy at

The University of Texas at Arlington

August 2023

Arlington, Texas

Supervising Committee:

Qinhong Hu, Ph.D. Supervising Professor

Majie Fan, Ph.D.

Xinbao Yu, Ph.D.

Behzad Ghanbarian, Ph.D.

Abstract

Experimental and theoretical studies of fluid-solid coupling processes of tight rock media

Tao Zhang, Ph.D.

The University of Texas at Arlington

Supervising Professor: Qinhong Hu

This study covers the application of continuum mechanics in the realm of rock work in geological studies. Continuum mechanics encompasses two major branches: fluid mechanics that deals with fluid behavior, and solid mechanics pertaining to the behavior of rock media. The research focuses on comprehending the mechanical behavior of rocks as a continuous mass, offering a comprehensive perspective for analyzing geological structures, fluid flow, and rock mechanics. Under the framework of continuum mechanics applied to rock media, following the sequence of the rock/solid properties, fluid flow properties, and the fluid-solid coupling behavior, this dissertation is divided into four sections, each addressing a unique aspect of the subject matter stated above.

The dissertation presents an analysis of true-triaxial hydraulic fracturing of granite samples for fluid-solid coupling processes during the rock failure, followed by an integrated technique for rapid gas permeability measurement of tight rock media. Then, this works elucidates shale wettability using a contrast-matching technique of Small Angle Neutron Scattering (SANS), investigating the heterogeneity and overturning of wettability at different pore intervals. This

research is significant in the field of geo-energy stewardship, which involve fluid-solid coupling phenomena in poromechanics, includes shale petroleum development, enhanced geothermal stimulation, CO_2 sequestration, H_2 storage, nuclear waste repository, and underground water management.

Keywords: hydraulic fracturing; permeability; wettability; small angle neutron scattering; continuum mechanism

Acknowledgements

I want to express my heartfelt gratitude to my supervisor, Dr. Qinhong Hu, who has not only guided me in my academic research but also been a guiding light in my life. His critical thinking in research and self-discipline in daily life have been a constant source of motivation and encouragement for me. I am deeply thankful for his patience, support, and invaluable wisdom of academic and daily lives that he has shared with me!

Meanwhile, I am immensely grateful to Dr. Behzad Ghanbarian at Kansas State University for his discussions and guidance in the permeability study. I also want to extend my appreciation to Drs. Gergely Nagy and Wei-Ren Chen at Oak Ridge National Laboratory, who assisted me with the (U)SANS research but also provided critical help with the user-proposals, scholarship applications, and actual experiments for my stays at ORNL. Special thanks also go to Drs. Zhiming Lu, Yushu Wu, Andrzej Radlinski, and Hanqiu Jiang for their insights on theoretical analyses on fluid dynamics and SANS studies. I am also thankful to the faculty members at UTA, especially Dr. Majie Fan for her daily support during my studies, and Dr. Xinbao Yu for his guidance throughout my PhD studies as the committee member.

Additionally, I have been fortunate to meet and collaborate with many colleagues and visiting scholars at UTA who have become not only good friends but also valuable academic partners. I cherish the happy moments shared with Drs. Chen Zhao, Longhui Bai, Xiaoguang Yang, Jingyi Wang, Xianglong Fang, Jhaber Dahsan Yacoub, and Yuta Fukatsu. I had many happy times with my fellow colleagues including Ogochukwu Azike, and Neil Handique. Last but not least, my good friend, Qiming Wang and Iltaf Khawaja Hasnain have provided me with selfless assistance during my PhD studies, and I really appreciate their camaraderie.

This research used resources at the Spallation Neutron Source, a DOE Office of Science

User Facility operated by the Oak Ridge National Laboratory.

July 23, 2023

Dedication

This dissertation is dedicated to my parents, my sisters, and my wife. I am deeply grateful for their unwavering support throughout my academic journey. To my wife, Ruirui Yuan, she is my soulmate, and her dedication and encouragement have been instrumental in my research endeavors.

To time, love, and my forthcoming daughter.

Table of Contents

Chapter 1: Introduction

Continuum mechanics (Coussy, 2011) is divided into two major branches: fluid mechanics (Darcy, 1856) that deals with the behavior of fluids, and solid mechanics (Biot, 1935, 1941) that covers the behavior of solid materials. Both branches utilize the fundamental laws of physics, such as the conservations of mass, momentum, and energy, to describe the behavior of materials. In the context of rocks, continuum mechanics (Coussy, 2004) can be used to understand and predict the behavior of geological structures under various conditions. The studies presented in this dissertation primarily focus on the continuum mechanics in the field of tight rock (sedimentary rock with low permeability).

Fillunger (1933) first introduced the concept of liquid-saturated porous solids in the 1910s, paving the way for further studies of differences between effective and general stress behaviors in ground samples. Building upon this concept, Terzaghi established the principles of effective stress in the 1920s (Terzaghi, 1923). Similar to Terzaghi's theory, Biot's theory explores the interaction between interstitial fluid (fluid inside of the porous media) and permeable porous materials in porous system after 1930s (Biot, 1941). For the fluid- solid coupling process, the structural properties of the porous media, the wettability and fluid-flow properties will both influence the poromechanics behavior. Thus, this dissertation is divided into four chapters (pieces of research), each addressing a unique aspect of the subject matter under the frame of continuum mechanics with a particular focus on the poromechanics of tight rock media.

Chapter one investigates the fracturing behavior of enhanced geothermal systems (EGS) reservoirs under field-relevant temperature and stress conditions (Atkinson, 2015; Hu et al.,

2020; Wong & Brace, 1979; Yong & Wang, 1980). Hydraulic fracturing tests on granite samples were conducted at different temperatures, and the results show weakening of granite at high temperatures. The failure pattern of grains during fracturing did not differ much at high and room temperatures. However, due to upscaling issues from the laboratory to field, the laboratory experiment will not directly provide some critical parameters needed for an EGS field exploration.

Chapter two presents an integrated technique for nano-Darcy level permeability measurements in porous media (Cui et al., 2009; Sakhaee-Pour & Bryant, 2012; Singh & Javadpour, 2016), such as nano-porous mudrocks. Rigorous mathematical solutions for transient and slightly compressible spherical flow are developed for early- and late-time responses (mathematical solution in Chapter 3). The technique is applicable to different sample characteristics and evaluated based on essential considerations. A practical workflow of solution selection and data reduction for permeability determination is provided for samples with different permeability and porosity at various granular sizes.

Chapter three focuses on the wetting properties in shale and their influence on fluid flow and mass transport (Anovitz & Cole, 2015). Using small angle neutron scattering (SANS) experiments and contrast-matching technique, this work employs various deuterated chemical liquids to quantify pore-space variation and identify wetting characteristics. The results reveal a complex and dynamic wettability for different ranges of pore diameters, with nanopores more amiable to oil than water. An antecedent contact with specific liquids can convert the initial wetting status and organic solvents can induce physical matrix expansion and swelling, resulting in changing pore size distribution. SANS method and contrast-matching technique

demonstrate practical utilization in understanding the interplay of pore structure and wetting characteristics in confined nano-pores space.

In conclusion, this dissertation experimentally and theoretically advances the knowledge of the characterization and application of continuum mechanics in the field of tight rock studies. The findings offer valuable insights into complex rock systems, fluid flow behavior, and rock mechanics behavior, providing significant contributions to the understanding of porous media in various geological fields.

Chapter 2: Analyses of true-triaxial hydraulic fracturing of granite samples for geothermal study

Abstract

The fracturing behavior of enhanced geothermal systems (EGS) reservoirs merits investigation under field-relevant temperature and stress conditions, in order to understand the creation of an extensive fracture network that helps achieve a high heat exchange efficiency. In this work, hydraulic fracturing tests were conducted on two 300 mm-sized cubic granite samples at room (32^{o}C) and field-relevant (250°C) temperatures under true triaxial compression conditions. The failure behavior and fracturing plane were studied using acoustic emission (AE) testing, μm-scale computed tomography (μm-CT), and scanning electron microscopy (SEM), in addition to the monitoring and analyses of pressure-flow curve during fracturing. The results show that: 1) at the macroscale, the strength of the granite sample was weakened at high (field-relevant) temperature, as shown by a decrease in the breakdown pressure and increase in closure pressure from the pressure-flow curve; 2) at the microscale, the failure pattern of grains during fracturing did not differ much at high and room temperatures for both intergranular and transgranular fractures; and 3) due to upscaling issues from the laboratory to field, however, the laboratory experiment will not directly provide some critical parameters (e.g., mud window pressure needed for fracture initiation and borehole failure avoidance) needed for an EGS field exploration.

Published as Zhang, T., Q.H. Hu, W.Y. Chen, Y. Gao, D. Li, and X.T. Feng. 2022. Analyses of true-triaxial hydraulic fracturing of granite samples for an enhanced geothermal system. Lithosphere, Volume 2022, Article ID 3889566, 13 pages. DOI: 10.2113/2022/3889566.

2.1. Introduction

Enhanced geothermal systems (EGS) have been promoted over the past several decades for their considerable potential as a renewable energy source (Entingh, 1999; Tester et al., 2006; Polsky et al., 2008; Lund et al., 2011; Kelkar et al., 2016;). The U.S. Department of Energy has recently initiated the FORGE (Frontier Observatory for Research in Geothermal Energy) project for the study of geothermal energy extraction from crystalline rocks, such as diorite and granite (Mellors et al., 2019). The EGS reservoir is created by the application of hydraulic stimulation, widely used for unconventional reservoir enhancement, through either hydro-fracturing or -shearing to enable efficient heat extraction (Mackie et al., 1988; Tester et al., 2006; Gischig and Preisig, 2015; Zhang and Hu, 2018).

The rock failure mode and development of resulting thermal fracture networks depend on the original stress distribution, as well as the original natural fracture distribution. It is desirable to generate hydro-shearing induced from the slip with pre-existing fractures during fracturing, as hydro-shearing tends to generate cracks which are not easily closed (Zoback, 2010; Riahi and Damjanac, 2013; Gischig and Preisig, 2015). Therefore, after locating and characterizing the natural fractures in dry hot rocks using, for example, a formation micro-imager (FMI), it is important to know how to create a controllable fracture network connected to the natural fractures in the continuous rock mass, for the prediction of fracture expansion and connectivity (Feng et al., 2019; Wang et al., 2020). Developing such an understanding is difficult, but key in preventing lost fluid circulation (Goodman, 1981; Feng et al. 2016), premature thermal breakthrough (Shook, 2001; Grant and Garg, 2012; Jung, 2013), and low heat exchange efficiency (Jiang et al. 2014; Huang et al. 2017; Asai et al., 2019).

The reservoir rocks of EGS typically lie deeper than 1,000 meters and exhibit temperatures exceeding 100°C under field stress conditions (Olasolo et al., 2016; Pan et al., 2019). Their mechanical behavior at high reservoir temperatures differs from room temperature. The influence of temperature on brittle failure of a sample has been observed at the macroscale, such that a small decrease in strength occurs with an increase in temperature (Kumar, 1968; Perkins et al., 1970; Fischer and Paterson, 1989; Paterson and Wong, 2005; Guo et al., 2021). These studies have reported that the damage during brittle failure could be induced by thermal cracking, or even mineral melting, which can promote the transition from brittle to ductile behavior at high temperatures.

At the microscale, thermal damage results in the slip or the dislocation of grain minerals at their boundary, induced by the difference in the thermal expansion coefficient of crystals during heating. This effect will cause dislocation blocking and mechanical failure of rock (Cho et al., 2009; Atkinson, 2015). In contrast, the initiation and growth of fractures stimulated by hydraulic fracturing in EGS reservoirs are controlled by three different principal stresses (Haimson and Fairhurst, 1967; Yew and Weng, 2014; Zhao et al., 2020). However, laboratory experiments involving hydro-shearing of slip or dislocation, especially under true tri-axial pressure conditions, are difficult to simulate field/reservoir conditions in terms of sample scale and equipment setting. As a result, an understanding of the actual heat storage and exchange mechanisms in the field is limited (Park et al., 2002; Cao et al., 2016; Nadimi et al., 2019; Zhuang et al., 2019; Hu et al., 2020), and is mostly limited to modeling studies rather than laboratory experiments (Sun et al., 2017; Yao et al., 2018; Zhou et al., 2018; Wu et al., 2019).

Since most laboratory-scale fracturing experiments have been performed at room

temperatures using conventional triaxial systems, where the intermediate principal stress equals the minimum principal stress, the laboratory research mimicking field pressure and temperature conditions is much needed. In this work, we present and discuss our recent studies of rock failure behavior during hydraulic fracturing under field stress conditions in a true-triaxial system for two granite samples at room- and high-temperature conditions. We employed acoustic emissions (AE) testing for fracture characterization during heating, as well as visual observations of a fluorescent tracer, thin sections, μm-Computed Tomography (CT), and scanning electron microscopy (SEM), to delineate the fracture networks after rock failure. We then discuss the difference in fracturing behaviors at both macro- and micro-scales.

2.2. Samples and methods

2.2.1 Sample description and methods for property characterization

The outcrop granite sample was collected from Zhangqiu in Shandong province in China. The granite body expanded in northeast-southwest direction by invasion in the Mesozoic Lower Cretaceous (K1C1) formed at the early Yanshan second stage (Ni et al., 2013). Two granite samples CH (high temperature loading) and CL (room temperature loading) were used for the hydraulic fracturing experiments cut from a same integral body. We deem they share the same properties for CH and CL as they were connected with each other before cutting and their physical and mechanical experiment was tested once from a parallel sample of CH and CL, including X-ray Diffraction (XRD), thin section, and uniaxial compression test (UCS).

The thin section sample was prepared for observing mineral structures of grains through regular microscopy on plain polarized and crossed polarized model, and the thin section was

dye-casted with a colored resin. XRD was performed on powder-sized samples at 300 mesh using a Bruker D8 Advance powder X-ray diffraction system. Basic rock mechanical parameters of the granite samples were obtained through uniaxial and Brazilian splitting experiments, including compression and tensile strength. The UCS was performed using triaxial equipment fitted through strain-stress curve for a maximum compression strength at 400 MPa**.**

2.2.2 Methodologies for true triaxial hydraulic fracturing tests

Two cubic granite samples, each 300 mm in length and without any visible cracks, were used in this work for hydraulic fracturing using water. A small cylindrically-shaped hole with a diameter of 10 mm was drilled in the top at Position A in Fig. 1a, and this was used to install the impression packer (Fig. 1b) for hydraulic injection. The Teflon rubber ring of the impression packer in Fig. 1b was designed to endure a maximum 70 MPa failure pressure. Note that the diameter and roughness of the drilled hole at Position A need to be strictly controlled, as they are the key to a good sealing. A temperature transducer was plugged into a 5 mm-hole in diameter at Position C in Fig. 1c in order to monitor the sample temperature during the heating and fracturing process.

The true-triaxial equipment with heating module shown in Fig. 1d was used to simulate field conditions. A maximum stress of 100 MPa can be applied in terms of the major (σ_1), intermediate (σ_2), and minor (σ_3) principal stress separately in three different directions at up to 400°C, a heating module was set at the four sides (positions labelled D in Fig. 1c) and also the top and bottom of the sample.

The true-triaxial equipment was integrated with an AE monitoring system. A wave transmission pole at Position E in Fig. 1c was specially designed to assist with signal acquisition and prevent the damage of the AE transducers under high temperatures. A total of 15 transducers were symmetrically installed at the eastern (the direction of $X<0$) and western (the direction of $X>0$) sides of the sample, meanwhile, the direction of $Y<0$ is North.

The brittle fractures generated from rock failure are accompanied with energy release and AE signals through elastic waves, which can be used for fracture source locating and failure magnitude analysis (Lockner, 1993). An acoustic emission can be induced and monitored through AE equipment during the thermal heating process of rock (Wong and Brace, 1979; Yong and Wang, 1980); during the heating, signals normally generated after the temperature breaks through the thermal heating threshold, which is 60 to 70°C for granite and has no relationship with the heating rate (Yong and Wang, 1980). In our experiments, efforts were made to heat gradually up to 250°C to avoid the thermal cracking, with the heating rate strictly controlled at 5°C/hr and 48 hours spent in total from the 32°C during the experiment. For the AE system used for crack monitoring in this experiment, the acoustic signals have a sensitive response during the heating process. However, for large volume deformation associated with stress release over a short period of time, the AE transducers were unable to sensitively capture the released signals, and only a few AE signal points were collected instead of a complete signal network after removing the noisy signals; this issue is being addressed with a design of a new and versatile system. Thus, the AE system was mainly used for thermally induced cracking research in this work.

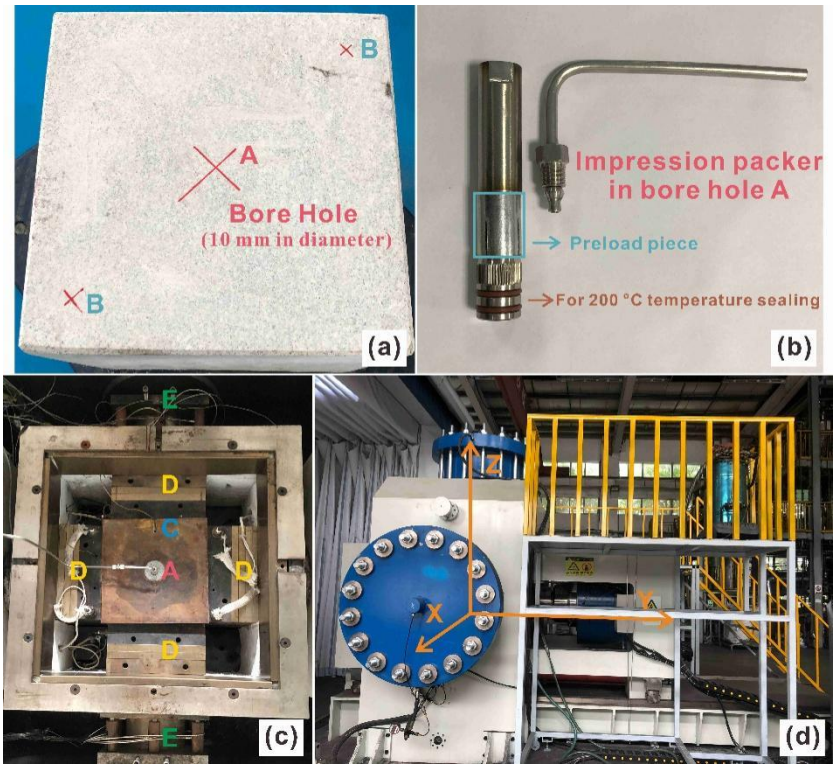

Fig. 1 Equipment and sample set-up of the true-axial experiment. For Fig. 1c, the hole in Position A is wellbore and Position C is for temperature transducer; Slab in Position D is heating module and the AE module has been set in Position E. For Fig. 1d, the direction of Y<0 is North, the direction of X>0 is West, and the direction of X<0 is East.

For samples tested in this work, the stress status of the EGS reservoir in the FORGE site was applied at a field-relevant temperature (at 250°C) and stress (Table 1) conditions for simulating the field-scale thermal conditions (Allis et al., 2019). The designed stress conditions in Table 1 are three principal stress which are independently and mutually orthogonal to each other, and the stresses were loaded at a constant rate of 0.5 MPa/s up to the designed pressure shown in Table 1.

Table 1 Stress condition loaded for samples CH and CL

Stress and direction in Fig. 1d	σ_1	σ_2	σ_3
Applied stress	50 MPa	40 MPa	30 MPa
Direction loaded for CH	Z-axis	Y-axis	X-axis
Direction loaded for CL	Z-axis	X-axis	Y-axis

2.2.3 Methodologies for fracture observation after failure

The fracturing fluid was purified water mixed with fluorescing dye 7Y-B310N which has a similar density (1.0-1.05 g/cm^3) to water and is completely miscible with water (http://www.tonixchem.com/detail2.asp?id=804).

For the original hydraulic fracturing experiment, where the temperature in the true-triaxial equipment was set at 250°C for sample CH, the fluorescent colors cannot be observed after the cooling finished and the sample unloaded, as most of the fluorescent dye has been vaporized at a high temperature. Thus, we used the hand pump connected to the embedded impression packer (Fig. 1b) to re-inject the fluorescent dye for both samples CH and CL. Note that the re-injection was performed gently to avoid the secondary damage of the failure plane that could complicate the observation of CT for the original failure of rock if extra artificial crack generated after hydraulic fracturing.

During the experiment, the sample was fractured at a constant injection flow rate, and after the rock failure, the SEM and CT images were used to identify the failure behavior and the fracture networks. For CT studies, the sample was cut into three blocks of 300 mm × 300 mm × 100 mm vertical to the direction of wellbore, as the X-rays of the CT equipment cannot

penetrate the whole sample in a 300 mm-sided cube. Before the CT analyses, samples CH and CL were reinjected, as described above, with the fluorescent dye for crack observation.

The CT tests were performed with a SOMATOM Definition AS CT Scanner from Siemens, to characterize the inner failure plane and distribution of artificial cracks. The CT has a spatial resolution of 0.1-1 mm for a scanning thickness of 0.4-20 mm. After cutting into 100 mm slabs for CT scanning, the three parts of sample CH were named as Part 1, Part 2 and Part 3 from the top, middle and bottom respectively, with each direction of the three blocks has been marked by the green letter on Fig. 2, and the north direction is consistent with the direction marked in Fig. 1 for Y<0. That is, from the top perspective, the northern direction pointed to the L orientation of the sample shown in Fig. 2. For data processing, the whole crack map was obtained from the 3D images provided from the CT scanning; CT data were reconstructed through MATLAB and RadiAnt software (https://www.radiantviewer.com/en/).

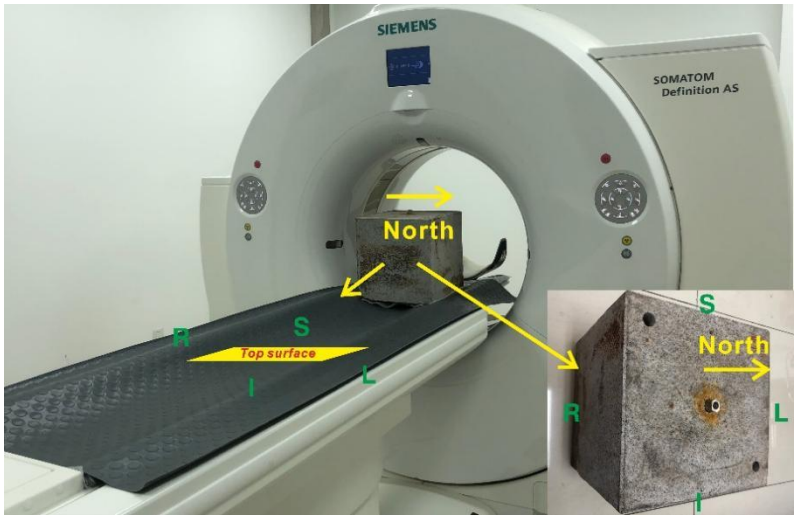

Fig. 2 Position and CT scanning direction of granite sample CH. The direction of R, S, I, and L (L close to the north direction) will consist with the direction of the scanning results in Fig. 9, and North is the direction of Y<0 in Fig .1d.

Finally, the mineral failure behavior near the crack surface after the hydraulic fracturing for CH and CL were observed from SEM images, in order to make a comparison of failure behavior and appearance of fracture between samples CH and CL, the SEM sample was the fresh fracture surface without any polishing. The surface scanning of SEM was performed to observe the distribution of different elements using Energy Dispersive Spectrometer (EDS) on the SEM instrument, and in combination with the XRD data, minerals on the failure plane were identified.

2.3. Results

2.3.1 Mineralogical and structure properties of sample

The two samples in this experiment are whole crystalline granite with granular and massive structure of sesame-grey color which cut from the integral body. The minerals of the granite sample are mainly plagioclase and quartz, with minor amounts of orthoclase and biotite as well as a small amount of clay minerals, XRD results are shown in Table 2.

Table 2 Mineral composition of the granite

Mineral	Quartz	Orthoclase	Plagioclase	Biotite	Clays
Percentage	16.8%	10.8%	59.2%	10.9%	2.3%

Natural micro-fractures in granite tend to diminish its strength. However, granite's strength improves with a consistent grain size compared to a discrete one, as smaller crystal sizes result in less vitric composition. In specific, while natural micro-fractures in granite diminish its strength, a consistent grain size improves its strength. Smaller crystal sizes can lead to a more vitric composition, which might weaken the rock. This observation is particularly evident in intermediate to acidic granite types, and the sample used in this experiment aligns with the

intermediate type.

From the polarized (upper) and crossed (bottom) photomicrographs of regular microscopy shown in Fig. 3, minerals in the granite sample can be observed to be discontinuous, and the crystals are inequigranular, as well as randomly distributed. From the polarized photomicrographs (two pictures at the top of Fig. 3), the shape of biotite was easily identified to be amorphous with colors ranging from light brown to dark brown, and its grain size is normally smaller than the feldspars and quartz. Plagioclase is also recognizable as it is “dirtier” (with more sheet structures present in grains) than quartz and orthoclase, while quartz tends to be in regular column. From the crossed photomicrographs (two pictures at the bottom of Fig. 3), it is clearly shown that minerals overlap with each other with hypidiomorphic texture (i.e., no fixed shape). Besides, almost no pores can be observed in the granite sample, indicative of ultra-low porosity and small pore size of the sample.

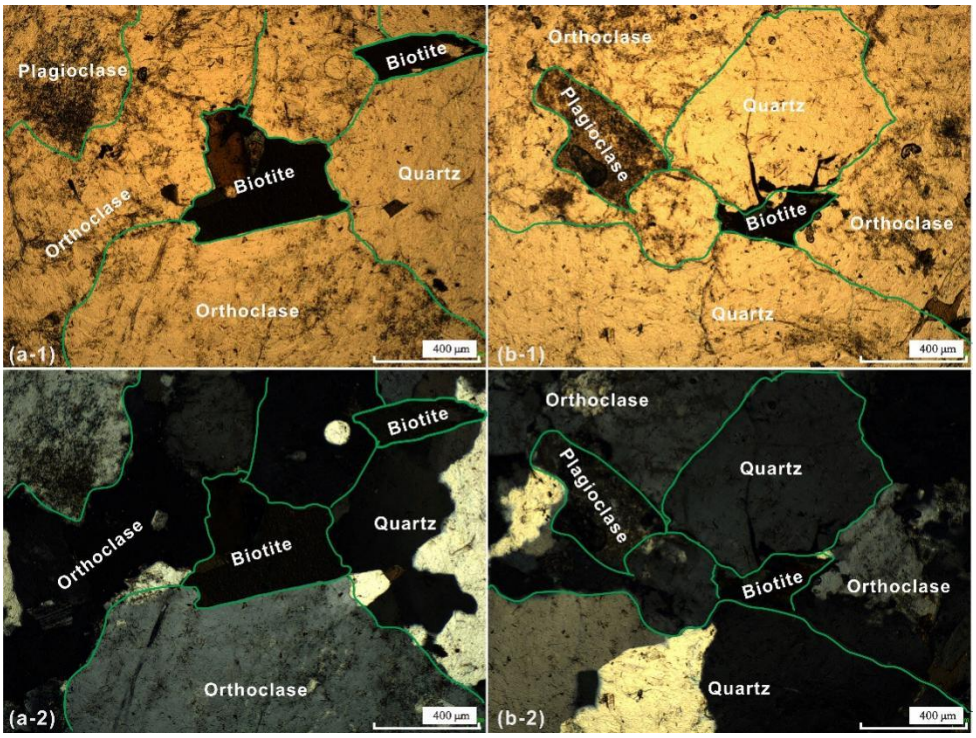

Fig. 3 Plain polarized (upper) and crossed polarized (bottom) photomicrographs of granite sample used in the experiments; Areas (a-1 & a-2) and (b-1 & b-2) are the same region in each case.

2.3.2 Rock mechanical properties

The rock mechanical properties of the parallel sample of CH and CL have been measured using UCS, and the results compiled in Table 3, where σ and τ are normal stress and tensile stress when failing in Fig. 4c, μ is the coefficient of internal friction, θ is the angle between the normal of fracture surface and σ_1. The tensile stress is used to calculate the failure pressure of hydraulic fracturing in Section 2.5.2.1. The rock failure pattern in the uniaxial experiments is the typical conjugate shear plane shown as in Fig. 4c. From the stress-strain curve in Fig. 5, there is a four-stage failure process that includes Stage I (compression stage), Stage II (linear elastic deformation stage), Stage III (stable deformation stage) and Stage IV (unstable

deformation stage). Notably, the sample used is of typically brittle nature, as the total volumetric strain V is less than 0.3, and the dilatancy between line V and line Ve generated in Stage III is less than 0.04.

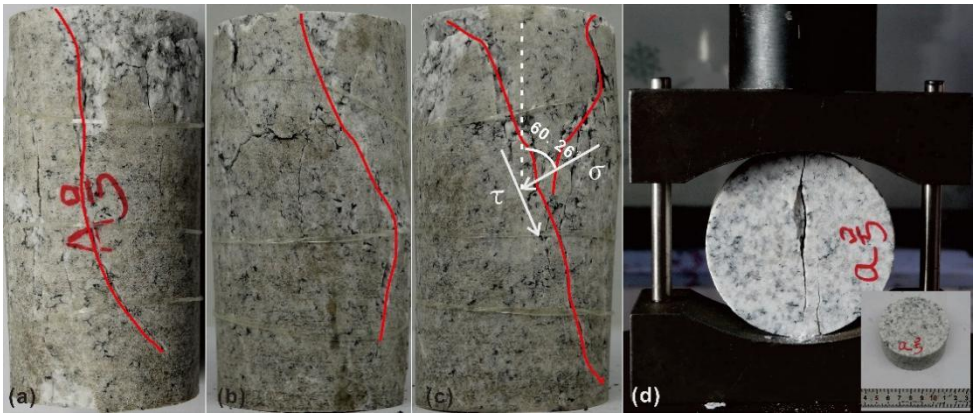

Fig. 4 UCS experiment (a)-(c) and the Brazilian splitting test (d).

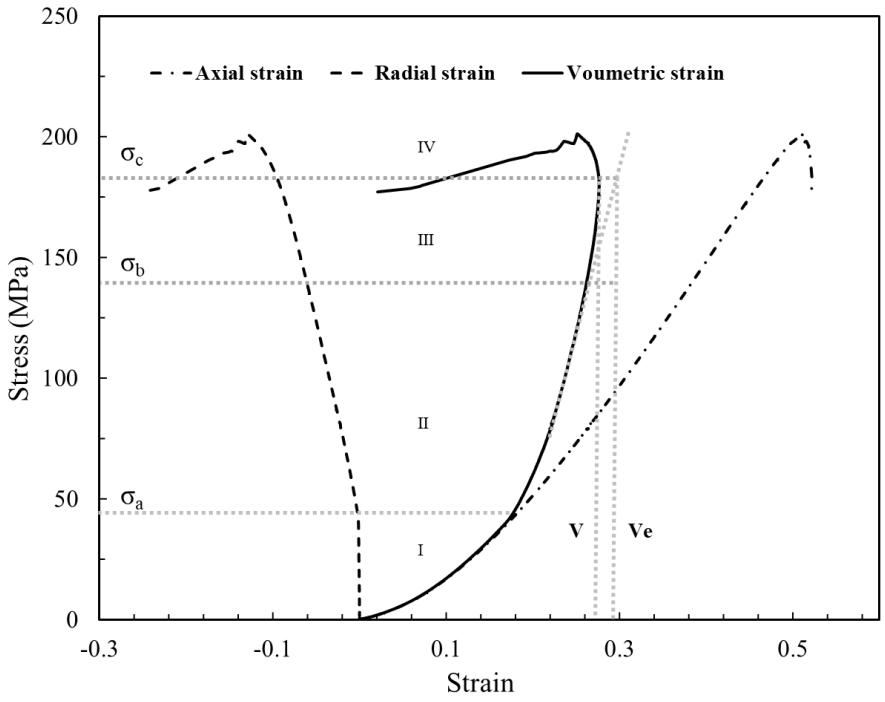

Fig. 5 Stress and strain curve of UCS experiment.

Table 3 Mechanical properties of granite sample

UCS (MPa)	E-modulus (GPa)	Poisson's ratio	Tensile strength (MPa)	Density (g/cm^3)	σ(MPa)	T (MPa)	μ	θ
201.18	41.09	0.18	10.7	2.61	50.3	87.0	1.40	60.26°

2.4. Thermal behavior and hydraulic properties of samples

2.4.1 Monitoring of the thermal behavior of the granite sample during heating

From Fig. 6, the captured AE signals indicate that some thermal cracks appeared during the heating process for the sample heated to 250°C. Two fracturing zones appeared along Line A and Line B of the tested sample, and the signal zones were mainly concentrated at the northern sides for Y=0 of the sample (shown in Fig. 6) and more concentrated at Zone A. The axis of X, Y, and Z in Fig. 6 is the same as those marked in Fig. 1d. Zone A cracking was initiated at the bottom sides of the borehole and extended towards the origin (X, Y, Z = 0); Zone B was also initiated at the bottom of borehole but extended in the direction of X=240, Y=0, and Z=0. For granite, when the thermally induced expansion stress of minerals exceeds the compression stress loaded on the sample, micro-fissures and cracks will converge together and come into macroscopic scale under a temperature gradient. For sample CH, as observed in Fig. 2, the mineral distribution is non-uniform, and most minerals are inequigranular with hypidiomorphic texture which may cause stress concentration during the heating, owning to the anisotropy of thermal expansion between each mineral and fluid inclusion. Sample CH had only four major types of minerals except for clays (2.3% in the sample we used; clays are easier to crack than mineral grains at low temperatures), however, the thermally induced cracks cannot be ignored as they may induce predominant fracturing channels and promote the failure process of rock during fracturing. Even though there were no extensive AE signals in other areas except for

Zones A and B, a single crack would be enough to accelerate the sample failure.

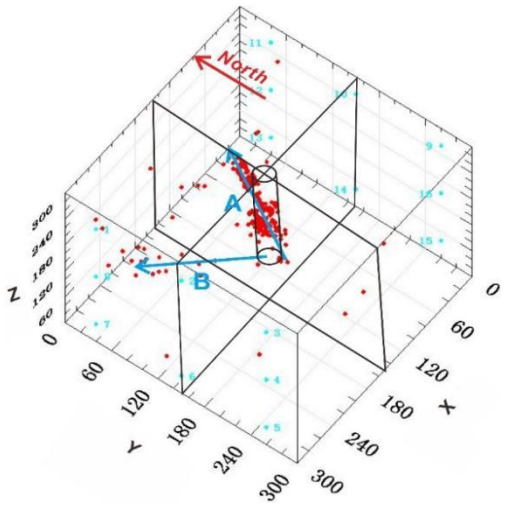

Fig. 6 AE signals during the heating process. The axis of X, Y, and Z is consistent with the direction marked in Fig. 1d.

2.4.2 Granite failure during fracturing

Figs. 7a-7b show the relationship between injection pressure and fluid flow used under different temperature conditions during the fracturing process, and the experiment for sample CH was conducted at 250°C and the sample CL was conducted at 32°C. The pressure-flow curve for two samples is divided into three stages, Stages I, II and III (as shown in Fig. 7a-7b) based on the fracturing behavior of pressure, while Stages I is pre-fracturing period, Stages II is propagation period, and Stages III is post-fracturing period.

For sample CH (shown in Fig. 7a), in Stage I, fluid was smoothly injected into the empty pipe system for hundreds of seconds before the total void volume of the pipe and borehole was filled. Proceeding to Stage II, fractures began to propagate after the void volume of the pipe system was nearly fully saturated, and a sharp linear rise of pressure appeared to indicate that

the fluid began to be injected into the sample through connected pores. The sharp rise stage of pressure sustained for about 35 s, then the sample failed when the pore pressure was raised to 13.1 MPa (the breakdown pressure). After the sample failure, the fluid pump was still opened for 35 s in Stage II, and around 35.8 mL (volumes at point C minus point A) of fluid was consumed in this stage. Continuing to Stage III, the pump was closed, however, the hydrostatic pressure did not decrease to zero, as a part of the injected fluid has been stored in the pore or crack systems in such high effective pressure and could not be released smoothly; therefore, the pressure maintained at 6.4 MPa.

For sample CL, in Stage II, we did not change the injection rate, which was still maintained at 15 mL/min as in Stage I; meanwhile, the loaded confining pressure for sample CL was the same as sample CH at 50 MPa, 40 MPa, and 30 MPa. At the injection rate of 15 mL/min, the sharp rise stage of pressure curve was much longer for sample CL (50 sec) than sample CH (35 sec) and around 14.9 mL (Point C minus Point A) of fluid was consumed in Stage II, which is less than half of the case for sample CH. Meanwhile, after the failure of sample CL, the injection pump was still operated in Stage III, and even the pump was closed, the pressure was maintained at 1.6 MPa for Equilibration in stage III.

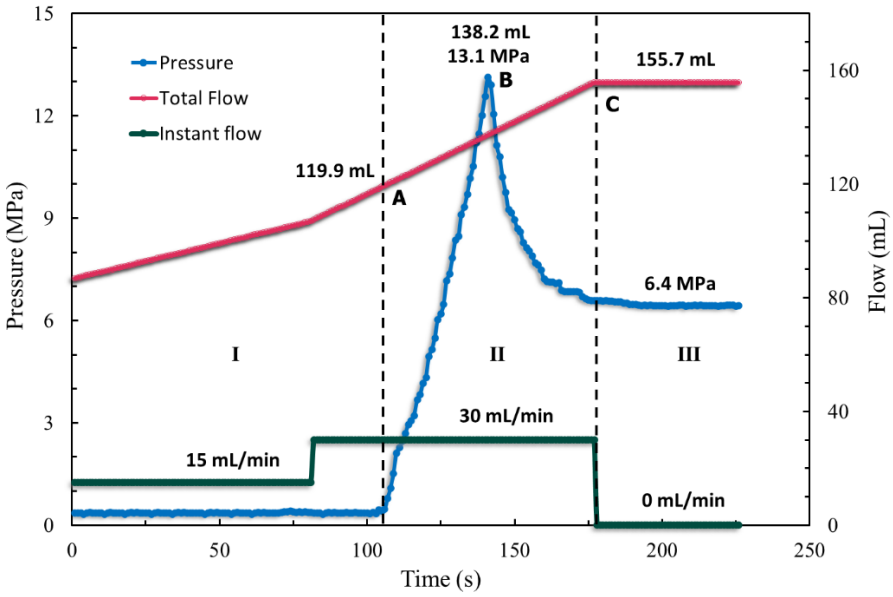

Fig. 7a Relationship between flow and pressure of sample CH under 250°C during hydraulic fracturing.

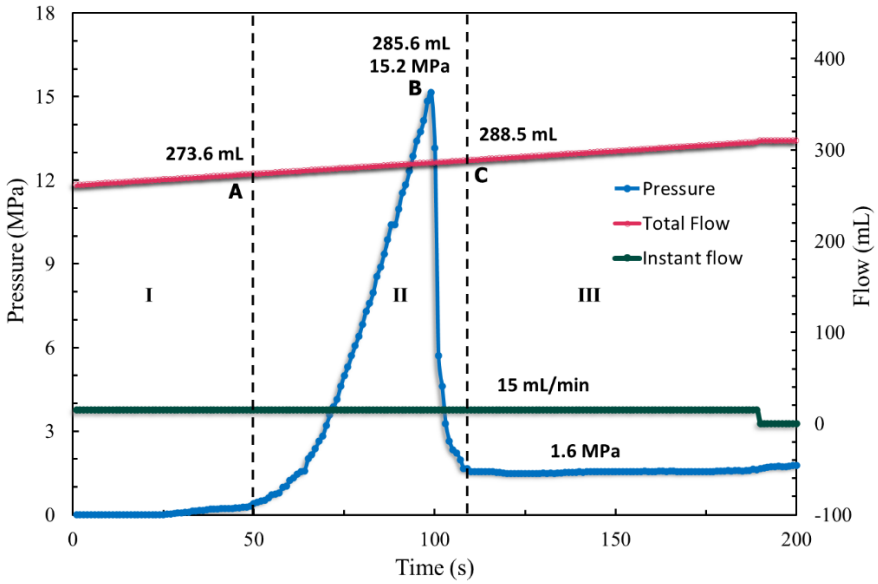

Fig. 7b Relationship between flow and pressure of sample CL at 32°C during hydraulic fracturing.

2.4.3. Description of fracturing system after rock failure

2.4.3.1 Reinjection of the fluorescent dye

After the re-injection of sample CH, it can be noticed that a part of the fluorescent dye flowed out at the floor, and some visible cracks can be observed on the sidewall, which means that fractures formed from the borehole are connected to the sample surface, meanwhile, those visible cracks on the surface have been remarked by the blue line in Fig. 8. Three axes marked on Fig. 8 were consistent with the directions marked in Fig. 1. For sample CH, there were three apparent surface cracks to appear at the eastern sides which nearly parallel to the Z-axes. Meanwhile, some cracks appeared near the bottom of the sample as a huge amount of fluorescent dye flowed out from the bottom, and the interior cracks were also observed from subsequent CT scanning. Sample CL roughly shared a same failure pattern as CH, however, the fractures in CL were more complex as they extended to both southern (X-Z surface on the southern side) and western (Z-Y surface on the western side) surface (shown in Fig. 8b). The surface crack behavior will be investigated with the inside crack again through the 3D CT characterization.

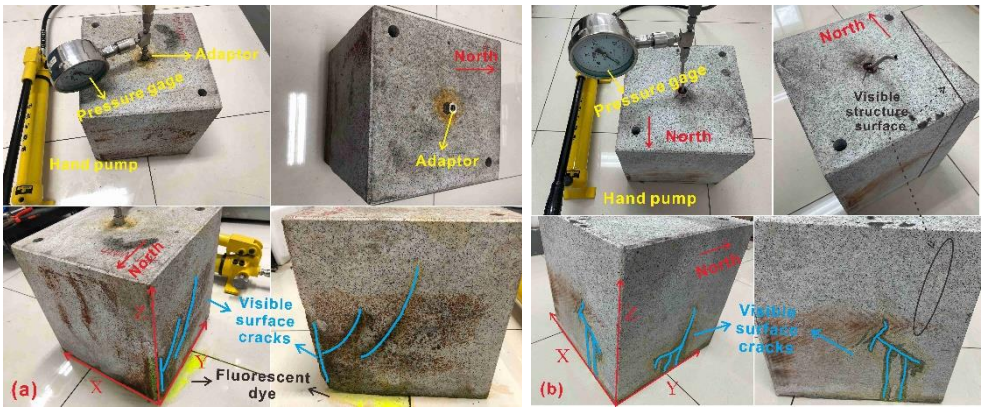

Fig. 8 Observed fractures on samples after hydraulic fracturing through the re-injection of fluorescent dye for sample CH in (a) and CL in (b); the black line in (b) shows the mineral structure in sample CL.

2.4.3.2 3D characterization of fractures

The 3D CT results were consistent with the observation from the appearance of fluorescent dye on the sample surface, that the failure plane has run through the sample and extended to the bottom side. The cracks after hydraulic fracturing were visible on the surface at mm-scales, then the fracturing network was compatible with the CT images and shown a good resolution in the 3D characterization.

The hydraulic fractures from CT scans are shown in Fig. 9. The upper (Part 1), middle (Part 2), and bottom (Part 3) parts of sample CH are all shown in lateral, top, and 3D perspectives, respectively. The profile position of the top perspective is marked by the yellow line in the images of lateral perspective, respectively in the upper, middle, and bottom parts. For the upper part of sample CH (Part 1), only a few fine (~0.1 mm resolution of CT scans) cracks can be observed in both samples of CH and CL either from the top perspective or the lateral perspective. Meanwhile, the whole impression packer (about 10 cm) was inserted into Part 1 which has not been taken out during CT scanning, thus the crack signals were interfered from the metal impression packer for the upper part of sample.

As for the middle part (Part 2) of samples CH and CL, the amounts of cracks appeared to be mainly distributed in the middle of both samples and paralleled to the east-west direction near the bottom. It was obvious that, in the lateral perspective, cracks were inclined to initiate from the bottom of the borehole, paralleling to the Z-axes, and go through Part 2 and further extend to Part 3. Cracks in Part 2 were slender for both samples as signals in 3D tomography are vague, however, from the lateral perspective, it is clear that the generated cracks in Part 2 for sample CL were more concentrated than sample CH.

For the bottom part (Part 3), more clear signals were captured for both samples of CH and CL. In this part, fine cracks finally converged to a single plane with a greater width, which is shown with a better resolution. The failure plane in sample CH is nearly parallel to the Y-axes with an angle of 30°and vertical to the X-Y plane, however, the failure plane in sample CL is parallel to X-axes but also vertical to the X-Y plane.

From those images captured from CT tests, it is clear that the main failure plane was generated from the borehole bottom with several cracks and finally converged into a single plane. As mentioned, the Z-axis was the maximum stress direction applied with 50 MPa, and the X-axis is the minimum stress direction applied for CH while Y-axis is the minimum stress direction applied for CL. Thus, from the middle to the bottom of the sample, the failure plane was always parallel to the maximum stress direction, however, for 300 mm cubic granite samples, though the difference of horizontal stress conditions was up to 10 MPa for both CH and CL, the failure plan has shown different behaviors that the failure plane in CH was presented in 30 degrees with the minimum stress direction while the failure plane in CL was totally vertical to the minimum stress.

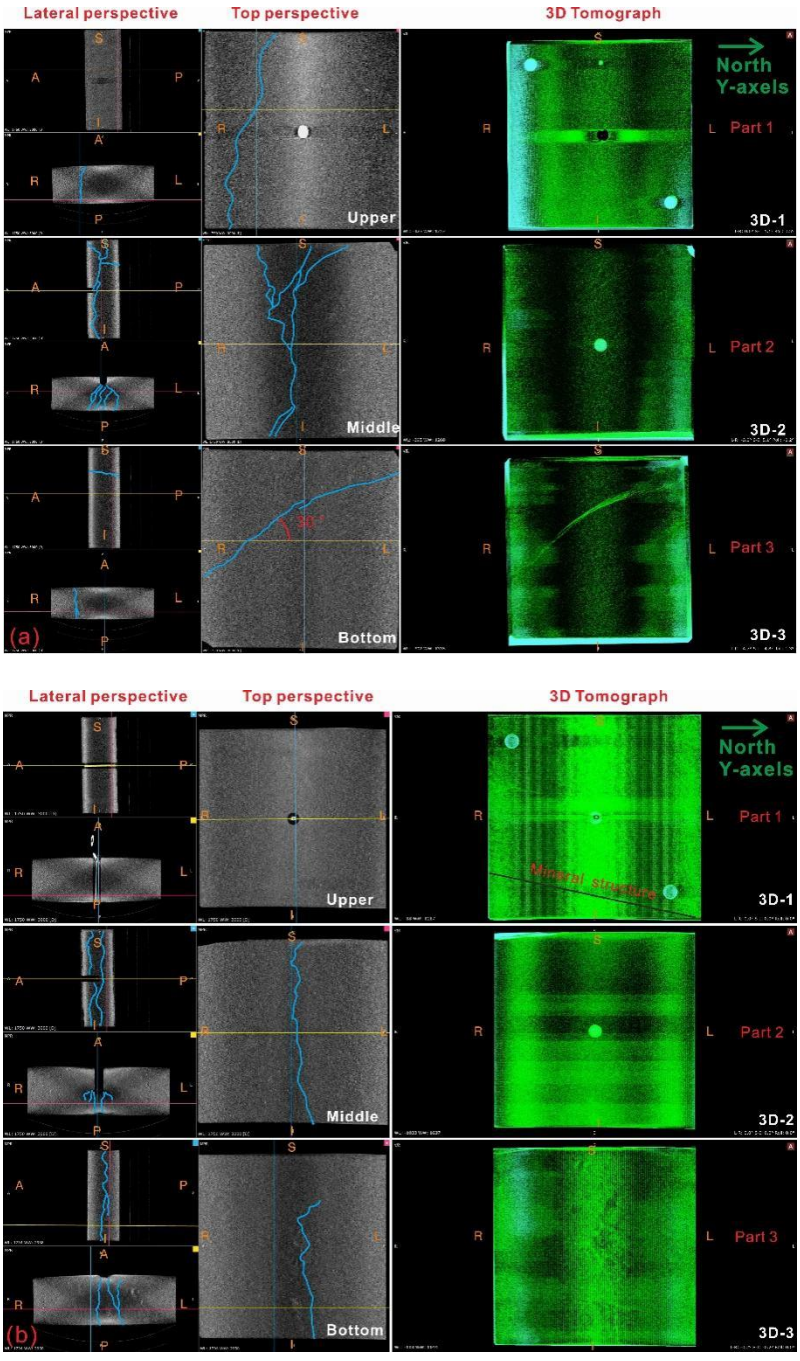

Fig. 9 3D tomographs of three parts of sample CH (a) and CL (b).

2.5. Thermal effects & indoor experimental indication for field development

2.5.1 Thermal effects on sample failure during hydraulic fracturing

2.5.1.1 Failure comparison for high- and room-temperature conditions

In this work, samples CH and CL are typical brittle rocks, as shown from the UCS experiment in Section 2.2.2. Some thermal effects, with associated decreasing strength, on rock failure appeared from the analysis of hydraulic fracturing pressure-flow curve, which has also been verified from the AE and CT results. Key parameters during fracturing of Fig. 7 are presented in Table 4.

Table 4 Key parameters of pressure-flow curve during fracturing

Sample	Failure pressure (MPa)	Closure pressure (MPa)	Flow of A-B (mL)	Flow of A-C (mL)	Flow of B-C (mL)	Time of A-B (s)	Time of A-C (s)	Time of B-C (s)	Flow rate in Stage II (mL/min)
CH	13.1	6.4	18.3	35.8	17.5	35	72	36	30
CL	15.2	1.6	12	14.9	2.9	50	58	10	15

Initially, during Stage II, the strength of the sample subjected to high temperature fracturing (13.1 MPa) was lower than that of the room-temperature sample (15.2 MPa). Conversely, in Stage III, the closure pressure of the high-temperature sample (6.4 MPa) exceeded that of the sample at 32°C (1.6 MPa). That is, under high temperature conditions, the sample was easier to be broken during fracturing, it was also easier to be closed after the pump closed, which shows a weakened tensile or shear strength, and also a lower Young's modulus (therefore, easier to be deformed under certain confining pressure) than sample under room-temperature environment. Secondly, as mentioned, two signal zone appeared in Fig. 3; however, to our surprise, the CT observations in Fig. 7a (especially in Part 3) show that the main failure plane coincided with Zone B instead of Zone A, even though more thermal signals appeared from AE monitoring in Zones A than B. The heating rate did not have a significant impact on the thermal damage, but the thermal effect is still irreversible to have potential effects on rock

failure as they may cause a weak structure and potentially preferential failure plane during fracturing (Wong and Brace, 1979; Freire-Lista et al., 2016).

Meanwhile, except for the thermal cracking, during the coupled process of injecting the cold fluid into the hot granite sample of CH, the heat expansion and cold shrinking phenomenon would accelerate the failure and weaken the extension strength of granite sample. The temperature difference between the fluid and the sample can induce stress concentration and cause mineral crystals to shrink. Notably, after water was injected into the pipe to make contact with the heated sample, the liquid water existed in a subcritical state. Furthermore, a larger volume of water was used for the sample under high temperature (18.3 mL) compared to the one at 32°C (12.0 mL) to reach the peak pore pressure in Stage II. Though the flow rate for sample CH doubled from 15 mL/min to 30 mL/min; however, time in each stage in Fig. 7 for CH (shown as in Table 4) were still greater than or even double than time used for sample CL. Meanwhile, as the subcritical water has lower viscosity and surface tension than water in 32°C, subcritical water may move farther away than liquid to microfractures or weaken rock surface, to cause stress concentration at the tip of fine nature cracks in rock to exceed the stress intensity factor of rock. However, after the pump was turned off, the closure pressure for CH in Stage III had been maintained at a constant value without any supplementary injection, which showed that the subcritical water was also easily trapped in fractures and cannot escape easily, as the closure pressure for CH was higher than CL.

2.5.1.2 Micro-scale observations of failure plane

In Fig. 10, the left-side six pictures were from CH while the right-side six pictures were

from CL, and the colored four pictures were the distribution of typical elements of Na and K. Fig. 10a-c were magnified 200 times from the image in Fig. 10 (CH), and Fig. 10d-f were magnified 200 times from the image in Fig. 10 (CL). These enlarged areas were marked by the rectangular region, and the identified minerals were marked on the picture as well.

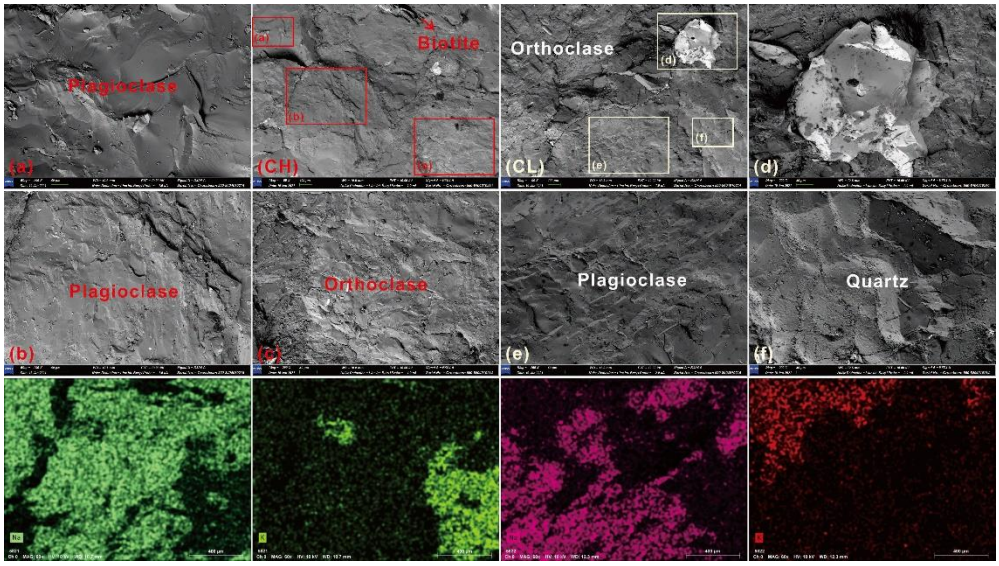

Fig. 10 SEM-observed failure surface where CH for a-c marked by red color and CL for d-f marked by white color.

Several failure features can be observed from Fig. 10. Firstly, the failure plane of different minerals is different from each other. The rupture surface of quartz is smoother than plagioclase, while plagioclase is also smoother than orthoclase. For orthoclase, the surface is wrinkled with fine cracks without a regular arrangement, while the texture on the rupture surface for plagioclase obey to one direction. Secondly, the same minerals in samples CH and CL share roughly the same failure pattern of minerals which did not change obviously under 250°C for sample CH. At macroscales, the high temperature tends to promote the brittle-ductile transition of granite sample during the deformation, while at microscales, the failure model of mineral

crystals inclines to be changed from transgranular to intergranular fractures. The transgranular fracture resembles the rupture surfaces of Fig. 10c and Fig. 10e, where grain boundaries are discernible. However, these surfaces are relatively smooth, lacking the pronounced texture seen in Fig. 10d. The transgranular fracture resembles the ruptured surfaces of Fig. 10c and Fig. 10e, where grain boundaries are discernible. Regarding the microscale failure pattern, we did not discern a noticeable thermal effect on sample CH. Both CH and CL exhibited the same failure model on each mineral grain, and they also displayed similar crack densities, as illustrated in Fig. 10.

2.5.2 Insights of laboratory hydraulic fracturing experiment for field development

2.5.2.1 Fracture initiation and containment

For rock fracture mechanics, mature empirical and theoretical understandings have been developed in these two aspects of fracture initiation and containment. Among these empirical criteria, the Mohr-Coulomb criterion is extensively employed to predict rock properties and to determine the failure patterns of rocks at macroscales., however, this mechanism assumed that the intermediate principal stress has no relation with the final failure pattern and strength. For theoretical criterion, Griffith (1921) proposed the brittle failure criterion of materials from the standpoint of energy and in combination with the thermodynamics, which has been further developed into non-linear and ductile failure model (Irwin, 1957; Rice, 1968; Dugdale, 1960; Barenblatt, 1962). Notably, the theory of Griffith was developed from the failure of single fracture at microscales, however, the angle of crack predicted by the Griffith theory is well consistent with the failure plane predicted by Mohr-Coulomb criterion (Brace, 1960). For

hydraulic fracturing, fluid exists in the pores of rocks, and the deformation and failure would be controlled both by fluid pressure and stress conditions, so the well-known practical mechanism for fracture initiation and extension has been deducted from the porous elastic theory as Eq. (1) (Haimson and Fairhurst, 1967).

$$P_1 = 3\sigma_{Hmax} - \sigma_{Hmin} + T \quad (1)$$

where $\sigma_{H_{max}}$ is the maximum horizontal stress, $\sigma_{H_{min}}$ is the minimum horizontal stress, and T is the tensile strength of rock.

The confining pressure condition applied in our experiments conforms to the typical normal faulting situation that the vertical stress (S_v) in Z-axes is the maximum stress applied on sample based on the classification of Anderson faulting theory (Anderson, 1905). Since the minimum stress condition wasn't applied in the Z-axes direction, horizontal fractures didn't form. Consequently, the failure planes were roughly parallel to the least principal stress and approximately perpendicular to the minimum horizontal stress (Anderson, 1905). As discussed in Section 3.3.2, the screenshot of the 3D tomography picture (the green picture in Fig. 9) for both samples CH and CL were given from the top view, and the failure plane shown were roughly parallel to the Z-axis (the maximum principal stress direction) and roughly vertical to the minimum stress for both samples of CH and CL. As observed from Section 2.3.3.2, the failure plane conformed to Anderson's theory that fractures are always parallel to the maximum stress direction and roughly vertical to the minimum stress direction.

The strength contrast from weak interface is the most essential factor to suppress the growth height of fracture, which was both observed from laboratory experiments (El Rabaa, 1987;

Jeffrey et al., 2009; Figueiredo et al., 2017) and simulation work (Dontsov and Peirce, 2015). The stress difference among three principal stresses is still the most important factor to control the fracture growth. As depicted in Fig. 8, a visible mineral structure, 1 mm in width, is evident on sample CL. However, this structure did not alter the inclination of the failure plane, as the final fracture surface extended across the structure to the sample's edge.

2.5.2.2 Sample size effects and influence of fluid leak-off

The laboratory experiments cannot fully simulate the engineered fracturing activities owning to the size effect which cannot provide sufficient fluid leak-off behaviors in the field (Yew and Weng, 2014). During field activities, the pumping fluid escapes from the hydro-fractures into the adjacent formation. This penetration into the rock creates new fractures on a circular surface, leading to a decrease in rock pressure. Fractures can be induced from hydro-fracturing or hydro-shearing, with tensile breaking or slip-on small pre-existing faults (Zimmermann et al., 2009; Zoback, 2010). A typical fracturing leak-off curve in field conditions is given in Fig. 11 with a constant flow rate, comparing with the laboratory fracturing curves of Fig. 7a-b.

For the laboratory experiments in Figs. 7a-7b, the pressure-flow curve is much more “concise”, especially in Stage III, the multiple stage phenomenon did not manifest as depicted in Fig. 11, following the FBP (formation breakdown pressure, also defined in Fig. 11). The first difference for laboratory and field leak-off experiments is that, before pressure comes to the breakdown pressure of FBP, the slope of pressure line changed after point LOP (leak-off point) for the field experiments, which means that more deformation and a possible leak-off occurred

before reaching the breakdown pressure. This phenomenon is more like the uniaxial compression test that the deformation evolves from the elastic deformation to stable development of cracks before rock failure. However, in our experiments with both CH and CL samples, changes in the slope before breakdown were not observed. The deformation of the granite remained uniform until reaching Point B in Fig. 7.

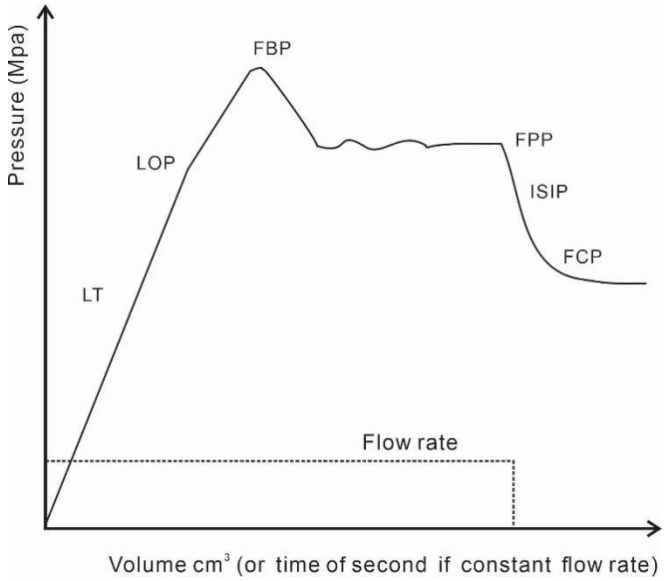

Fig. 11 Pressure vs. time (volume) during mini-frac or extended leak-off tests (Gaarenstroom et al., 1993; Zoback, 2010).

Secondly, the instantaneous shut-in pressure (ISIP) in Fig. 11 does not equal to its fracture propagation pressure (FPP), as the FPP is the sum of the minimum stress pressure and the pressure induced from the fluid viscosity in reservoirs. When fracturing in the field breakdown, as shown in Fig. 11, the ISIP is equal to its minimum stress applied after the pump is closed instantaneously, a few moments later the final and stable fracture closure pressure (FCP) appeared, which is lower than ISIP. However, for the laboratory experiments, no matter under high- or room-temperature environment, when pressure comes to its breakdown pressure of

Point B, the pressure will decrease sharply just to the stable value (the post-failure pressure) and will not change anymore. That is, for the laboratory experiments, after the propagation finishes, no matter the pump is closed or not, the pressure just becomes a final and stable value (the closure pressure of FCP as the threshold value). The over threshold pressure will be released, and for pressure under FCP, its value will be maintained. As the FPP has just become the FCP owing to the existence of fluid leak-off for the laboratory-scale experiments in Fig. 7a-b, the laboratory-scale experiment is difficult to provide mud window pressure of FPP needed for field development (Aghajanpour et al., 2017). Meanwhile, the higher loading pressure will induce higher closure pressure for FCP. This can be determined from the relationship between pressure and flow rate, as the pressure vs. the square root of time can be the linear decay curve (Zoback, 2010).

When reaching to the fracture propagation stage during fracturing, the sample size effect brings significant influence on laboratory experiments, especially on post-failure behavior. A larger sample ensures not only the observation of failure but also the degradation of rock during the post-failure stage. However, samples for laboratory hydraulic fracturing experiments are typically less than 1 m^3. Even in this experiment, what is considered a relatively larger sample, having a cubic form with each side measuring 30 cm, was used. In this research, the loss of circulation appeared obviously both for samples CH and CL, and after the fracture was formed from the borehole to the sample edge, the pumping liquid was leaked-off easily since there was not much geo-reservoir zone need to be fractured. For laboratory experiments, the leak-off behavior for sample CH and sample CL was also different, as water in samples CH and CL were at different phases.

2.6. Conclusions

True triaxial hydraulic fracturing tests were performed by using granite samples both in 32°C (for sample CL) and high temperature (for sample CH) up to 250°C. Lithologic and mechanical properties of samples were analyzed to help the interpretation of fracturing experiments, where the difference in failure curve and cracking pattern was observed between CH and CL.

The research found that (1) for brittle granite used in this study, the strength of sample under high temperature decreased shown in a lower break down pressure (point B in Fig. 6) and higher closure pressure (pressure in Stage III in Fig. 6) during hydraulic fracturing; (2) however, we did not observe a huge difference of fracturing failure pattern of mineral grains at microscales, samples exhibited transgranular fractures at both high and room temperatures; (3) the orientation of fractures during hydraulic fracturing was controlled by the stress conditions; (4) the sample size effect used under laboratory-scale experiments cannot be ignored as they are difficult to provide the realistic parameters needed for field studies such as strata stress condition and mud window pressure.

References

1. Aghajanpour, A., Fallahzadeh, S.H., Khatibi, S., Hossain, M.M., & Kadkhodaie, A., 2017. Full waveform acoustic data as an aid in reducing uncertainty of mud window design in the absence of leak-off test. Journal of Natural Gas Science and Engineering, 45, 786-796.
2. Allis, R.G., Gwynn, M., Hardwick, C., Hurlbut, W., & Moore, J., 2018. Thermal characteristics of the FORGE site, Milford, Utah. Geothermal Resources Council Transactions, 42, 15. Anderson, E.M., 1905. The dynamics of faulting. Transactions of the Edinburgh Geological Society 8(3), 387-402.
3. Asai, P., Panja, P., McLennan, J., & Deo, M., 2019. Effect of different flow schemes on heat recovery from Enhanced Geothermal Systems (EGS). Energy 175, 667-676.
4. Atkinson, B.K., 2015. Fracture Mechanics of Rock, Elsevier.
5. Barenblatt, G.I., 1962. The Mathematical Theory of Equilibrium Cracks in Brittle Fracture, Elsevier, pp. 55-129.
6. Brace, W.F., 1960. An extension of the Griffith theory of fracture to rocks. Journal of Geophysical Research 65(10), 3477-3480.
7. Cao, W., Huang, W., & Jiang, F., 2016. A novel thermal–hydraulic–mechanical model for the enhanced geothermal system heat extraction. International Journal of Heat and Mass Transfer. 100, 661-671.
8. Cho, W.J., Kwon, S., & Choi, J.W., 2009. The thermal conductivity for granite with various water contents. Engineering Geology, 107(3-4), 167-171.
9. Dontsov, E.V., & Peirce, A.P., 2015. Proppant transport in hydraulic fracturing: crack tip screen-out in KGD and P3D models. International Journal of Solids and Structures, 63, 206-218.
10. Dugdale, D.S., 1960. Yielding of steel sheets containing slits. Journal of the Mechanics and Physics of Solids, 8(2), 100-104.
11. El Rabaa, W., 1987. Hydraulic fracture propagation in the presence of stress variation, Society of Petroleum Engineers.
12. Entingh, D.J., 1999. Enhanced Geothermal Systems (EGS) R&D Program. No. EGS-Report

2000-4B (Final), Princeton Energy Resources International, Rockville, MD.

13. Feng, X. T., Haimson, B., Li, X., Chang, C., Ma, X., Zhang, X., & Suzuki, K., 2019. ISRM suggested method: determining deformation and failure characteristics of rocks subjected to true triaxial compression. Rock Mechanics and Rock Engineering, 52(6), 2011-2020.
14. Figueiredo, B., Tsang, C. F., Rutqvist, J., & Niemi, A., 2017. The effects of nearby fractures on hydraulically induced fracture propagation and permeability changes. Engineering Geology, 228, 197-213.
15. Fischer, G.J., & Paterson, M.S., 1989. Dilatancy during rock deformation at high temperatures and pressures. Journal of Geophysical Research: Solid Earth, 94(B12), 17607-17617.
16. Freire-Lista, D.M., Fort, R., & Varas-Muriel, M.J., 2016. Thermal stress-induced microcracking in building granite. Engineering Geology, 206, 83-93.
17. Gaarenstroom, L., Tromp, R., & Brandenburg, A., 1993. Overpressures in the Central North Sea: Implications for trap integrity and drilling safety, pp. 1305-1313, Geological Society of London.
18. Gischig, V.S., & Preisig, G., 2015. Hydro-fracturing versus hydro-shearing: A critical assessment of two distinct reservoir stimulation mechanisms, International Society for Rock Mechanics and Rock Engineering, ISRM-13CONGRESS-2015-103.
19. Goodman, M.A., 1981. Lost circulation in geothermal wells: survey and evaluation of industry experience (No. SAND-81-7129). Enertech Engineering and Research Co., Houston, TX (USA).
20. Grant, M.A., Garg, S.K., 2012. Recovery factor for EGS. In Proceedings of the 37th Workshop on Geothermal Reservoir Engineering, Stanford University, Stanford, California, USA, pp. 738-740.
21. Griffith, A.A., 1921. VI. The phenomena of rupture and flow in solids. Philosophical Transactions of the Royal Society of London. Series A, containing papers of a mathematical or physical character, 221(582-593), 163-198.
22. Guo, T.Y., Wong, L.N.Y., & Wu, Z., 2021. Microcracking behavior transition in thermally treated granite under mode I loading. Engineering Geology, 282, 105992.

23. Haimson, B., & Fairhurst, C., 1967. Initiation and extension of hydraulic fractures in rocks. Society of Petroleum Engineers Journal, 7(03), 310-318.
24. Hu, L., Ghassemi, A., Pritchett, J., Garg, S., 2020. Characterization of laboratory-scale hydraulic fracturing for EGS. Geothermics, 83, 101706.
25. Huang, W., Cao, W., & Jiang, F. 2017. Heat extraction performance of EGS with heterogeneous reservoir: A numerical evaluation. International Journal of Heat and Mass Transfer, 108, 645-657.
26. Irwin, G.R., 1957. Analysis of stresses and strains near the end of a crack transversing a plate. Journal of Applied Mechanics, Transactions ASME. 24, 361-364.
27. Jeffrey, R.G., Bunger, A., Lecampion, B., Zhang, X., Chen, Z., van As, A., Allison, D.P., De Beer, W., Dudley, J.W., & Siebrits, E., 2009. Measuring hydraulic fracture growth in naturally fractured rock. Society of Petroleum Engineers, SPE-124919-MS.
28. Jiang, F., Chen, J., Huang, W., & Luo, L. 2014. A three-dimensional transient model for EGS subsurface thermo-hydraulic process. Energy, 72, 300-310.
29. Jung, R. 2013. EGS—goodbye or back to the future. In ISRM International Conference for Effective and Sustainable Hydraulic Fracturing. International Society for Rock Mechanics and Rock Engineering, ISRM-ICHF-2013-022.
30. Kelkar, S., WoldeGabriel, G., & Rehfeldt, K., 2016. Lessons learned from the pioneering hot dry rock project at Fenton Hill, USA. Geothermics, 63, 5-14.
31. Kumar, A., 1968. The effect of stress rate and temperature on the strength of basalt and granite. Geophysics, 33(3), 501-510.
32. Lockner, D., 1993. The Role of Acoustic Emission in the Study of Rock Fracture. Elsevier, pp. 883-899.
33. Lund, J.W., Freeston, D.H., & Boyd, T.L., 2011. Direct utilization of geothermal energy 2010 worldwide review. Geothermics, 40(3), 159-180.
34. Mackie, T.R., Bielajew, A.F., Rogers, D., & Battista, J.J., 1988. Generation of photon energy deposition kernels using the EGS Monte Carlo code. Physics in Medicine & Biology, 33(1), 1.
35. Nadimi, S., Forbes, B., Moore, J., Ye, Z., Ghassemi, A., & McLennan, J.D., 2019.

Experimental evaluation of effect of hydro-shearing on fracture conductivity at the Utah FORGE site. In Proceedings of 44th Workshop on Geothermal Reservoir Engineering Stanford University.

36. Mellors, R., Sherman, C., Fu, P., McLennan, J., Morris, J., Ryerson, F., & Morency, F., 2019. Potential use of distributed acoustic sensors to monitor fractures and micro-seismicity at the FORGE EGS site. In Proceedings, 44th Workshop on Geothermal Reservoir Engineering.
37. Ni, J., Liu, J., Tang, X., Yang, H., Xia, Z., & Guo, Q., 2013. The Wulian metamorphic core complex: A newly discovered metamorphic core complex along the Sulu orogenic belt, eastern China. Journal of Earth Science, 24(3), 297-313.
38. Olasolo, P., Juárez, M.C., Morales, M.P., & Liarte, I.A., 2016. Enhanced geothermal systems (EGS): A review. Renewable and Sustainable Energy Reviews, 56, 133-144.
39. Pan, S.Y., Gao, M., Shah, K.J., Zheng, J., Pei, S.L., & Chiang, P.C., 2019. Establishment of enhanced geothermal energy utilization plans: barriers and strategies. Renewable Energy, 132, 19-32.
40. Park, B.Y., Kim, K.S., Kwon, S., Kim, C., Bae, D.S., Hartley, L.J., & Lee, H. K., 2002. Determination of the hydraulic conductivity components using a three-dimensional fracture network model in volcanic rock. Engineering Geology, 66(1-2), 127-141.
41. Paterson, M.S., & Wong, T., 2005. Experimental Rock Deformation - The Brittle Field. Springer-Verlag Berlin Heidelberg.
42. Perkins, R.D., Green, S.J., & Friedman, M., 1970. Uniaxial stress behavior of porphyritic tonalite at strain rates to 103/second. In International Journal of Rock Mechanics and Mining Sciences & Geomechanics Abstracts (Vol. 7, No. 5, pp. 527-535). Pergamon.
43. Polsky, Y., Capuano, L., Finger, J., Huh, M., Knudsen, S., Mansure, A.J.C., Raymond, D., & Swanson, R., 2008. Enhanced Geothermal Systems (EGS) Well Construction Technology Evaluation Report. SAND2008-7866, Sandia National Laboratories, Albuquerque, New Mexico, 108 pp. Web. doi:10.2172/1219316.
44. Riahi, A., & Damjanac, B., 2013. Numerical study of hydro-shearing in geothermal reservoirs with a pre-existing discrete fracture network. In Proceedings of the 38th

workshop on geothermal reservoir engineering, Stanford, CA, pp. 11-13.

45. Rice, J.R., 1968. A path independent integral and the approximate analysis of strain concentration by notches and cracks. Journal of Applied Mechanics, 35(2): 379-386.
46. Shook, G.M., 2001. Predicting thermal breakthrough in heterogeneous media from tracer tests. Geothermics, 30(6), 573-589.
47. Sun, Z., Zhang, X., Xu, Y., Yao, J., Wang, H., Lv, S., Sun, Z., Huang, Y., Cai, M., & Huang, X., 2017. Numerical simulation of the heat extraction in EGS with thermal-hydraulic-mechanical coupling method based on discrete fractures model. Energy, 120, 20-33.
48. Tester, J.W., Anderson, B.J., Batchelor, A.S., Blackwell, D.D., DiPippo, R., Drake, E.M., Garnish, J., Livesay, B., Moore, M.C., & Nichols, K., 2006. The future of geothermal energy. Massachusetts Institute of Technology, 358.
49. Wang, S., Xu, W., Yan, L., Feng, X. T., Xie, W. C., & Chen, H., 2020. Experimental investigation and failure mechanism analysis for dacite under true triaxial unloading conditions. Engineering Geology, 264, 105407.
50. Wong, T., & Brace, W.F., 1979. Thermal expansion of rocks: some measurements at high pressure. Tectonophysics, 57(2-4), 95-117.
51. Wu, H., Fu, P., Morris, J.P., Mattson, E.D., Hawkins, A.J., Zhang, Y., Settgast, R.R., & Ryerson, F.J., 2019. Characterizing fracture flow in EGS Collab experiment based on stochastic modeling of tracer recovery. In 44th Workshop on Geothermal Reservoir Engineering.
52. Yao, J., Zhang, X., Sun, Z., Huang, Z., Liu, J., Li, Y., Xin, Y., Yan, X., & Liu, W., 2018. Numerical simulation of the heat extraction in 3D-EGS with thermal-hydraulic-mechanical coupling method based on discrete fractures model. Geothermics, 74, 19-34.
53. Yew, C.H., & Weng, X., 2014. Mechanics of Hydraulic Fracturing, Gulf Professional Publishing, pp. 65-67.
54. Yong, C., & Wang, C.Y., 1980. Thermally induced acoustic emission in Westerly granite. Geophysical Research Letters, 7(12), 1089-1092.
55. Zhang, X., & Hu, Q., 2018. Development of geothermal resources in China: A review.

Journal of Earth Science, 29(2), 452-467.

56. Zhao, C., Xing, J., Zhou, Y., Shi, Z., & Wang, G., 2020. Experimental investigation on hydraulic fracturing of granite specimens with double flaws based on DIC. Engineering Geology, 267, 105510.
57. Zhou, Q., Oldenburg, C.M., & Kneafsey, T.J., 2018. Modeling transport of multiple tracers in hydraulic fractures at the EGS Collab test site. In Proceedings of 43rd Workshop on Geothermal Reservoir Engineering.
58. Zhuang, X., Zhou, S., Sheng, M., & Li, G., 2020. On the hydraulic fracturing in naturally-layered porous media using the phase field method. Engineering Geology, 266, 105306.
59. Zimmermann, G., Tischner, T., Legarth, B., & Huenges, E., 2009. Pressure-dependent production efficiency of an enhanced geothermal system (EGS): stimulation results and implications for hydraulic fracture treatments. In Rock Physics and Natural Hazards (pp. 1089-1106). Birkhäuser Basel.
60. Zoback, M.D., 2010. Reservoir Geomechanics, Cambridge University Press, pp. 221-231.

Chapter 3: An integrated technique for rapid gas permeability measurement of tight rock media

Abstract

Nano-darcy level permeability measurements of porous media, such as nano-porous mudrocks, are frequently conducted with gas invasion methods into granular-sized samples with short diffusion lengths and thereby reduced experimental duration; however, these methods lack rigorous solutions and standardized experimental procedures. For the first time, we resolve this by providing an integrated technique (termed as gas permeability technique) with coupled theoretical development, experimental procedures, and data interpretation workflow. Three exact mathematical solutions for transient and slightly compressible spherical flow, along with their asymptotic solutions, are developed for early- and late-time responses. Critically, one late-time solution is for an ultra-small gas-invadable volume, important for a wide range of practical usages. Developed as applicable to different sample characteristics (permeability, porosity, and mass) in relation to the storage capacity of experimental systems, these three solutions are evaluated from essential considerations of error difference between exact and approximate solutions, optimal experimental conditions, and experimental demonstration of mudrocks and molecular-sieve samples. Moreover, a practical workflow of solution selection and data reduction to determine permeability is presented by considering samples with different permeability and porosity under various granular sizes. Overall, this work establishes a rigorous, theory-based, rapid, and versatile gas permeability measurement technique for tight media at sub-nano Darcy levels.

Highlights

- An integrated (both theory and experiments) gas permeability technique (GPT) is presented.
- Exact and approximate solutions for three cases are developed with error discussion.
- Conditions of each mathematical solution are highlighted for critical parameters.
- Essential experimental methodologies and data processing procedures are provided and evaluated.

3.1. Introduction

Shales, crystalline, and salt rocks with low permeabilities (e.g., $<10^{-17}$ m^2 or 10 micro-darcies μD) are critical components to numerous subsurface studies. Notable examples are the remediation of contaminated sites(Neuzil, 1986; Yang et al., 2015), long-term performance of high-level nuclear waste repositories (Kim et al., 2011; Neuzil, 2013), enhanced geothermal systems (Huenges, 2016; Zhang & Hu et al., 2021c), efficient development of unconventional oil and gas resources (Hu et al., 2015b; Javadpour, 2009), long-term sealing for carbon utilization and storage (Fakher et al., 2020; Khosrokhavar, 2016), and high-volume and effective gas (hydrogen) storage (Liu et al., 2015; Tarkowski, 2019). For fractured rocks, the accurate characterization of rock matrix and its permeability is also critical for evaluating the effectiveness of low-permeability media, particularly when transport is dominated by slow processes like diffusion (Ghanbarian et al., 2016; Hu et al., 2012).

Standard permeability test procedures in both steady-state and pulse-decay methods use consolidated cm-sized core-plug samples, which may contain fractures and show dual- or triple-porosity characteristics (Abdassah & Ershaghi, 1986; Bibby, 1981). The overall permeability may therefore be controlled by a few bedding-oriented or cross-cutting fractures, even if experiments are conducted at reservoir pressures (Bock et al., 2010; Gensterblum et al., 2015b; Gutierrez et al., 2000; Luffel et al., 1993). Fractures might be naturally- or artificially-induced (e.g., created during sample processing), which makes a comparison of permeability results among different samples difficult (Heller et al., 2014). Hence, methods for measuring the matrix (non-fractured) permeability in tight media, with a practical necessity of using granular samples, have attracted much attention to eliminate the sides effect of fractures (Civan

et al., 2013; Egermann et al., 2005; Heller et al., 2014; Wu et al., 2020; J. J. Zhang et al., 2020).

A GRI (Gas Research Institute) method was developed by Luffel et al. (1993) and followed by Guidry et al. (1996) to measure the matrix permeability of crushed mudrocks (Guidry et al., 1996; Luffel et al., 1993). Such a method makes permeability measurement feasible in tight and ultra-tight rocks (with permeability < 10^{-20} m^2 or 10 nano-dcarcies, nD), particularly when permeability is close to the detection limit of the pulse-decay approach on core plugs at ~10 nD (e.g., using commercial instrument of PoroPDP-200 of CoreLab). In the GRI method, helium may be used as the testing fluid to determine permeability on crushed samples at different sample sizes (e.g., within the 10-60 mesh range, which is from 0.67 mm to 2.03 mm). The limited mesh size of 20-35 (500-841 μm in diameter) was recommended in earlier works, which has led to the colloquial names of "the GRI method/size" in the literature (Cui et al., 2009; Kim et al., 2015; Peng & Loucks, 2016; Profice et al., 2012). However, Luffel et al. (Guidry et al., 1996; Luffel et al., 1993) did not document the processing methodologies needed to derive the permeability from experimental data from such a GRI method. That is, there are neither standard experimental procedures for interpreting gas pulse-decay data in crushed rock samples nor detailed mathematical solutions available for data processing in the literature (Kim et al., 2015; Peng & Loucks, 2016; Profice et al., 2012). In this work, we achieve to: (1) develop mathematical solutions to interpret gas pulse-decay data in crushed rock samples without published algorithm available as this method shares different constitutive phenomena to the traditional pulse-decay method for core plug samples in Cartesian coordinates; and (2) present associated experimental methodology to measure permeability, reliably and reproducibly, in tight and ultra-tight granular media.

We first derive the constitutive equations for gas transport in granular (unconsolidated or crushed rock) samples. Specifically, we develop three mathematical solutions which cover different experimental situations and sample properties. As each solution shows its own pros and cons, we then in detail present the error analyses for the derived exact and approximate solutions and discuss their applicable requirements and parameter recommendation for practical usages. This work aims to fill the knowledge gap of the granular rock (matrix) permeability measurement and follow-on literature by establishing an integrated methodology for reproducible measurements of nD-level permeability in tight rock media.

3.2. Mathematical solutions for gas permeability of granular samples

For a compressible fluid under unsteady-state conditions, flow in a porous medium can be expressed by the mass conservation equation:

$$\frac{\partial p}{\partial t} + \nabla \cdot (\rho \overline{v}) = 0 \tag{1A}$$

where p is the pressure, t is the time, ρ is the fluid density, and $\overline{v}$ is the Darcy velocity. In continuity equations derived for gas flow in porous media, permeability can be treated as a function of pressure through the ideal gas law. Constitutive equations are commonly established for a small pressure variation to avoid the non-linearity of gas (the liquid density to be a constant) and to ensure that pressure would be the only unknown parameter (Haskett et al., 1988). For spherical coordinates of fluid flow in porous media, assuming flow along the radial direction of each spherical solid grain, Eq. (1A) becomes

$$\frac{\partial p}{\partial t}\phi = \frac{1}{c_t}\frac{k}{\mu r^2}\frac{\partial}{\partial r}\left(r^2\frac{\partial p}{\partial r}\right) \tag{1B}$$

The gas compressibility c_t is given by

$$c_t = \frac{1}{\rho}\frac{d\,\rho}{d\,p} = \frac{1}{p} - \frac{1}{z}\frac{d\,z}{d\,p} \tag{1C}$$

In Eqs. (1B) and (1C), ϕ and k are sample porosity and permeability, r is the migration distance of fluid, μ is the fluid viscosity, and z is the gas deviation (compressibility) factor and is constant.

To correct for the non-ideality of the probing gas, we treat gas density as a function of pressure and establish a relationship between the density and the permeability through a pseudo-pressure variable (given in the 1st part of Supplemental Information SI1). Detailed steps for deriving mathematical solutions for the GPT can be found in SI2, based on heat transfer studies (Carslaw & Jaeger, 1959). The Laplace transform, in combination with the Bessel equation, is an efficient tool for solving gas transport in granular samples with low permeabilities, as applied in this study. Alternatively, other approaches, such as the Fourier analysis, Sturm-Liouville method, or Volterra integral equation of the second form may be used (Carslaw & Jaeger, 1959; Haggerty & Gorelick, 1995; Ruthven, 1984).

We applied dimensional variables to derive the constitutive equation given in Eq. (S10) for which the initial and boundary conditions are

$$\frac{\partial^2 U_s}{\partial \xi^2} + s^2 U_s = 0\Big|_{U_s=0,\xi=0} \tag{2A}$$

$$\alpha^2(U_s - 1) = \frac{3}{K_c}\left(\frac{\partial U_s}{\partial \xi} - \frac{U_s}{\xi}\right)\Big|_{\xi=1} \tag{2B}$$

where U_s and ξ represent the dimensionless values of gas density and sample scale, and s is

the transformed Heaviside operator. α in Eq. (2B) is determined by solving Eq. (S30) for its root. K_c in Eq. (1E) is a critical parameter that represents the volumetric ratio of the total void volume of the sample cell to the pore volume of the porous samples. It is similar to the storage capacity, controlling the acceptable measurement range of permeability and decay time, in the pulse-decay method proposed by Brace et al. (1968).

The fractional gas transfer for the internal (limited K_c value) and external (infinite K_c value) gas transfer of sample is given by

$$F_f = 1 - 6\sum_{n=1}^{\infty} \frac{K_c(1+K_c)e^{-\alpha_n{}^2\tau}}{9(K_c+1)+\alpha_n{}^2K_c{}^2} \tag{2C}$$

$$F_s = 1 - \frac{6}{\pi^2}\sum_{n=1}^{\infty} \frac{e^{-(n\pi)^2\tau}}{n^2} \tag{2D}$$

where F_f and F_s represent the uptake rate of gas outside and inside the sample separately as a dimensionless parameter, and τ is the Fourier number of dimensionless time. Three approximate solutions of the transport coefficient based on Eqs. (2C) and (2D) for various conditions are presented below.

The late-time solution to Eq. (2C) for a limited K_c value (called LLT hereafter) is

$$k = \frac{R_a{}^2\mu c_t\phi_f s_1}{\alpha_1{}^2} \tag{3A}$$

The late-time solution to Eq. (2D) when K_c tends to infinity (ILT hereafter) is

$$k = \frac{R_a{}^2\mu c_t\phi_f s_2}{\pi^2} \tag{3B}$$

The early-time solution to Eq. (2D) when K_c approaches infinity (IET hereafter) is

$$k = \frac{\pi {R_a}^2 \mu c_t \phi_f s_3}{36} \tag{3C}$$

In Eq. (3), R_a is the particle diameter of a sample, and s_1, s_2, and s_3 are the three exponents that may be determined from the slopes of data on double logarithmic plots. Table 1 summarizes Eqs. (3A) to (3C) and conditions under which such approximate solutions would be valid.

Table 1. Solutions schematic with difference K_c and τ values

Parameter	Symbol	Remarks		
Volume fraction[§]	K_c	Limited value for $K_c < 10$	Infinity value for $K_c > 10$	
Exact. Density fraction[£]	F	F_f	F_s	
Approx. Solution of Density fraction[*]	Eqs. (3A-3B)	Eq. (3A) (LLT)	Eq. (3C) (IET)	Eq. (3B)) (ILT)
Available Dimensionless time for Approx. solution	τ	Late-time solution $\tau > 0.024$	Early-time solution $\tau < 0.024$	Late-time solution $\tau > 0.024$

[§] It defines as the volumetric ratio of the total void volume of the sample cell to the pore volume of the porous samples, the classification between the limited and infinity value is proposed as 50 with the following analyses.
[£] The original constitutive equation for different K_c value.
[*] Eqs. (3A-3C) are three approximate solutions of density faction function F.

Base on diffusion phenomenology, Cui et al. (2009) presented two mathematical solutions similar to our Eqs. (3A) and (3C). In the work of Cui et al. (2009), however, the lack of detailed analyses of τ and K_c in the constitutive equations may deter the practical application of Eq. (3B), which is unable to cover an experimental condition of small sample mass with a greater τ (further analyzed in section 3.3). In addition to that, Cui et al. (2009) did not comprehensively assess practical applications of their two solutions, which is addressed in this study. Hereafter, we refer to the developed mathematical and experimental, gas-permeability-measurement approach holistically as gas permeability technique (GPT).

3.3. Practical usages of algorithms for the GPT

As aforementioned, mathematical solutions given in Eqs. (3A) and (3B) were deduced based on different values of K_c and τ as shown in the SI2. This means each solution holds only under specific experimental conditions, which are mostly determined by the permeability, porosity, and mass of samples, as well as gas pressure and void volume of the sample cell. In this section, the influence of parameters K_c and τ on the solution of constitutive equation is analyzed and a specific value of dimensionless time (τ = 0.024) is proposed as the criterion required to detect

the early-time regime from the late-time one for the first time in the literature. We also demonstrate that the early-time solution of Eq. (3C), which has been less considered for practical applications in previous studies, is also suitable and unique under common situations. Besides, the error of the approximate solution compared to the exact solution and their capabilities are discussed, as it helps to select an appropriate mathematical solution at small τ values. Moreover, we showcase the unique applicability and feasibility of the new solution of Eq. (3B).

3.3.1 Sensitivity analyses of the K_c value for data quality control

To apply the GPT method, appropriately selecting the parameter K_c in Eqs. (3A)-(3C) is crucial, as it is a critical value for data quality control. The dimensionless density outside the sample, U_f, is related to K_c via Eq. (S33) in the SI2. One may simplify Eq. (S33) by replacing the series term with some finite positive value and set

$$U_f - \frac{K_c}{1 + K_c} > 0 \tag{4}$$

We define $K_f = K_c/(1 + K_c)$ to interpret the density variance of the system as K_f is closely related to the dimensionless density outside the sample, U_f.

Eq. (4) shows the relationship between the U_f and K_c (Fig. 1). For $K_c > 0$, K_f falls between 0 and 1. The higher the K_f value, the less sensitive the system is to density changes. For K_c equal to 50 (not shown in Fig. 1), K_f would no longer be sensitive to K_c variations as it has already approached 98% of the dimensionless density. This means that the U_f value needs to be greater than 0.98, and this leaves only 2% of the fractional value of U_f available for

capturing gas density change. When K_c is 100, the left fractional value of U_f would be 1%. This would limit the amount of data available (the linear range in Fig. S1) for the permeability calculation, which would complicate the data processing. Thus, for the GPT experiments, a small value of K_c (less than 10) is recommended, as K_f nearly reaches its plateau beyond K_c = 10 (Fig. 1). When K_c is 10, the left fractional value of U_f is only as low as 9%.

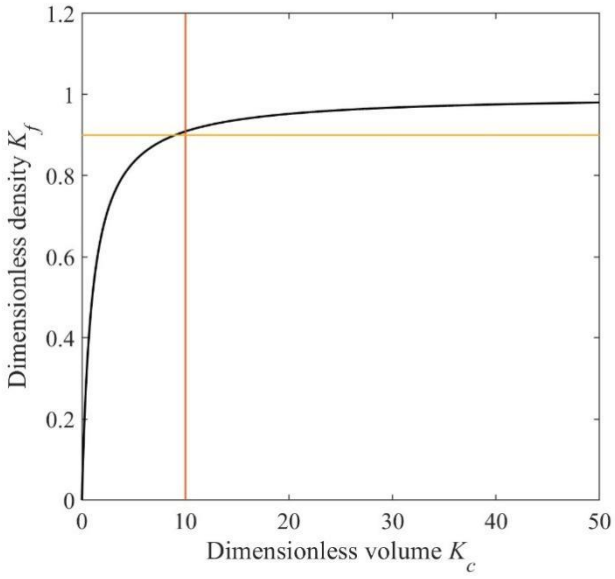

Fig. 1. Dimensionless density, K_f, as a function of dimensionless volume K_c. Recall that $K_f = K_c/(1 + K_c)$. Major variations in K_f occur for K_c < 10 indicating longer gas transmission duration with more pressure-decay data available for permeability derivation.

3.3.2 Recommendation for solution selection

The following three aspects need to be considered before selecting the appropriate solution for permeability calculation: 1) selecting early- or late-time solutions; 2) error between the approximate and exact solutions; and 3) the convenience and applicability of solutions suitable for different experiments. We will first discuss the selection criteria for early- or late-time

solutions.

Fig. 2(a) shows the exact solution of F_s with their two approximate early- and late-time solution (Table 1). Two exact solutions of F_f where K_c equals to 10 or 50 are also demonstrated in Fig. 2(a). Fig. 2(b) depicts the exact solution from F_f for different K_c values from 1 to 100 and their corresponding approximate solution for Eq. (3A). The intersection point of the solution Eq. (3B) and Eq. (3C), namely τ = 0.024 in Fig. 2(a), is used for distinguishing early- and late-time solutions.

Two notable observations can be drawn from Fig. 2(b). Firstly, the approximate solution Eq. (3A) would only be applicable at late times when τ is longer than 0.024. For $\tau < 0.024$, regardless of the K_c value, Eq. (3C) would be more precise than Eqs. (3A) and (3B) and return results close to the exact solution for both F_f and F_s. Secondly, results of Eqs. (3A) and (3B) presented in Fig. 2(a) are similar; there difference is very small especially for $K_c > 10$. Due to the fact that core samples from deep wells are relatively short in length and their void volume is small (ultra-low porosity and permeability such as in mudrocks with $k \leq 0.1$ nD), in practice, a solution for $10< K_c <100$ is the most common outcome, even if the sample cell is loaded as full as possible. Under such circumstances, the newly derived solution, Eq. (3B), becomes practical and convenient: 1) if the K_c and dimensionless time τ have not been evaluated precisely before the GPT experiment, this solution may fit most experimental situations; 2) this solution is suitable for calculation as it does not need the solution from the transcendental equation of Eq. (S30) because the denominator of α has been replaced by π. The data quality control is discussed in Section 3.4.1.

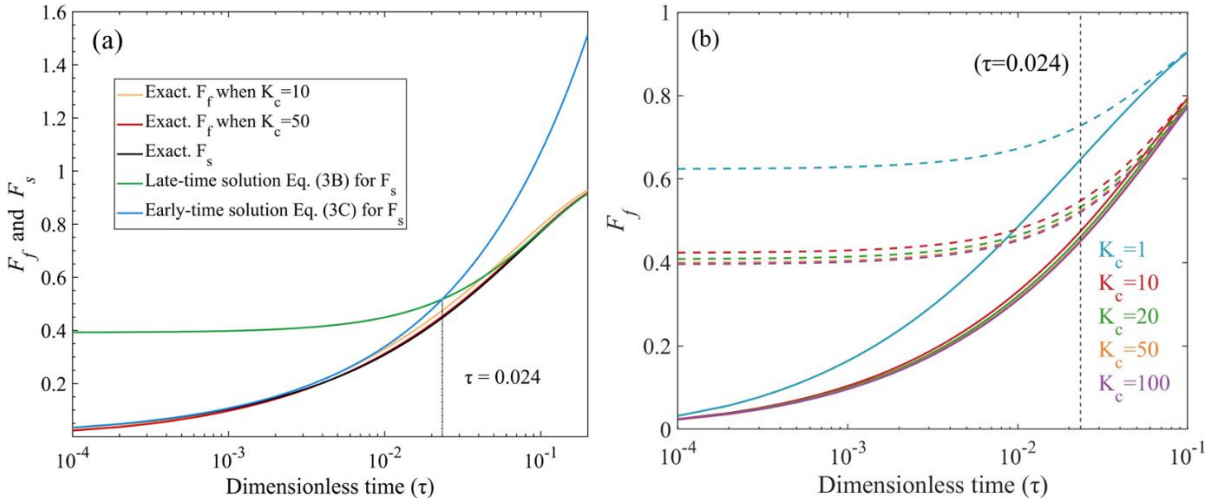

Fig. 2. Three GPT solutions with different values of τ, K_c; the dashed lines are approximate solutions without a series expansion in Fig. (2b) for F_f. Figure modified from Cui et al. (2009).

3.3.3 Applicability of the early-time solution

A small K_c value can guarantee a sufficient time for gas transfer in samples and provide enough linear data for fitting purposes. We note that the selection of the limited K_c solution of F_f, and the infinity K_c solution F_s is controlled by K_c. However, before the selection of K_c, the dimensionless time is the basic parameter to be estimated as a priori before the early- or late-time solutions are selected.

For pulse-decay methods, the early-time solution has the advantage of capturing the anisotropic information contained in reservoir rocks (Jia et al., 2019; Kamath, 1992). However, it suffers from the shortcoming of uncertainty in data for initial several seconds, which as a result is not recommended for data processing (Brace et al., 1968; Cui et al., 2009). This is due to: (1) the Joule-Thompson effect, which causes a decrease in gas temperature from the expansion; (2) kinetic energy loss during adiabatic expansion; and (3) collision between

molecules and the container wall. These uncertainties normally occur in the first 10-30 sec, shown in our experiments as a fluctuating period called "Early Stage".

However, the "Early Stage" present in pulse-decay experiments does not mean that the early-time solution is not applicable. We demonstrate the relationship between time and dimensionless time in Fig. 3 that a short dimensionless time may correspond to a long testing period of hundred to thousand seconds in experiments. This is particularly noticeable for the ultra-low permeability samples with $k \leq 0.1$ nD and small dimensionless times $\tau < 0.024$. This situation would only be applicable to early-time solution, but with data available beyond the "Early Stage" and provide available data in a long time (hundreds to thousands of seconds). For example, the early-time solution would fit ultra-low permeability samples in 600s for 0.1 nD, and at least 1000s for 0.01 nD shown in Fig. 3 in the region below the dark line. Then, using Eq. (3C), the derived permeability would be closer to its exact solution in the earlier testing time (but still after the "Early Stage"). The mudrock samples that we tested, with results presented in Section 3.5.3, exhibit low permeabilities, approximately on the order of 0.1 nD.

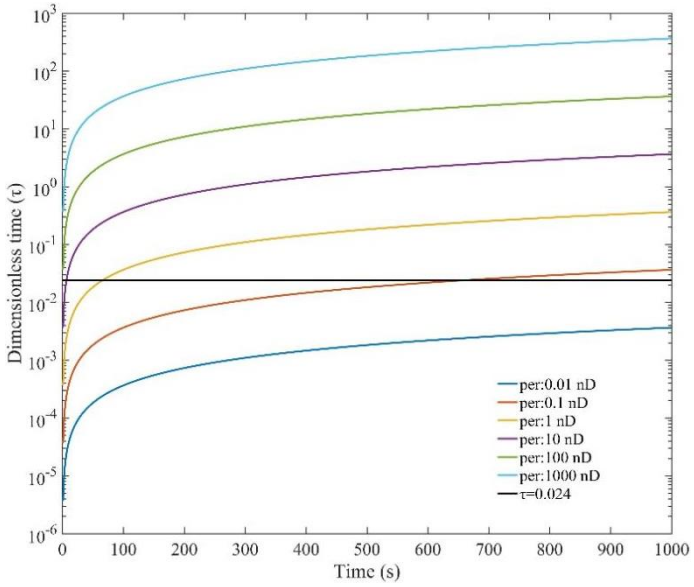

Fig. 3 Dimensionless time τ versus actual times for different permeability values trough Eq. (S14) using He gas, sample porosity of 5%, and sample diameter of 2 mm.

3.3.4 Error analyses between exact and approximate solutions

It is unpractical to use the exact solutions with their series part to do the permeability calculation; thus, only the approximate solutions are used and the error difference between the exact and approximate solutions is discussed here. The original mathematical solutions, Eqs. (S39) and (S49), are based on series expansion. For dimensionless densities F_f and F_s in Eqs. (S39) and (S49), their series expansion terms should converge. However, the rate of convergence is closely related to the value of τ. For example, from Eq. (S30), when $\tau \geq 1$, the exponent parts of U_s and U_f are at least $(2n+1)\pi^2$. Therefore, the entire series expansion term can be omitted without being influenced by K_c. In practical applications, the solutions given in Eqs. (3A)-(3C) are approximates without series expansion. In this study, we provide the diagrams of change in errors with dimensionless time in the presence of adsorption (Fig.

4).

For F_f, the error differences between the exact and approximate solutions are 3.5% and 0.37% for τ = 0.05 and 0.1 when K_c = 10, respectively. When $\tau \leq 0.024$, the error would be greater than 14.7%. Fig. 2(b) shows that F_f can be approximated as F_s when K_c is greater than 10; the error difference between F_f and F_s is quite small at this K_c value (for K_c = 10, 6.6% is the maximum error when τ = 0.01; 4.4% when τ = 0.05; and 2.9% when τ = 0.1) as shown in Fig. 4.

For F_s, the error difference is roughly the same as F_f and equal to 3.6% for τ = 0.05 and 0.38% for τ = 0.1. This verifies that newly derived Eq. (3B) is equivalent to Eq. (3A) when K_c is greater than 10. As for the evaluation of Eq. (3C), the error difference with the exact solution will increase with dimensionless time (5.1% for τ = 0.003, 9.7% for τ = 0.01, and 16% for τ = 0.024).

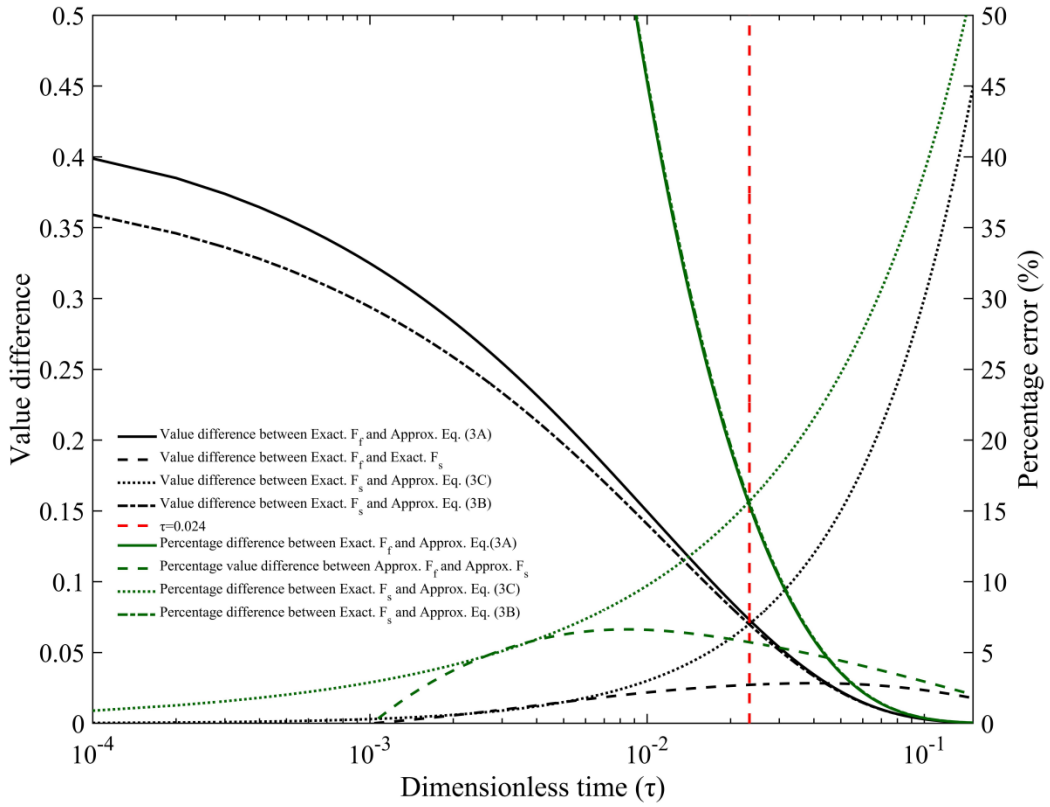

Fig. 4. Error analyses of F_f and F_s for their exact and approximate solutions

3.4. Influence of kinetic energy on gas transport behavior

3.4.1 Flow state of gas in granular samples

In the following, we apply the approximate solutions, Eqs. (3A-3C), to some detailed experimental data and determine permeability in several mudrock samples practically compatible with sample size, gases, and molecular dynamics analyses.

During the GPT, with the boundary conditions described in SI2, the pressure variation is captured after gas starts to permeate into the sample from the edge, and the model does not take into account the gas transport between particles or into any micro-fractures, if available. Thus,

the transport that conforms to the "unipore" model and occurs after the "Early Stage" (defined in Section 3.3.3) or during the "Penetration Zone" (the area between the two vertical lines in Fig. 5), should be used to determine the slope. Fig. S2 shows how to obtain the permeability result using the applicable mathematical solutions (Eqs. 3A-C). Fig. 5 shows the pressure variance with time during the experiment using sample size from 0.34 mm to 5.18 mm for sample X-1 and sample X-2. From Fig. 5, the time needed to reach pressure equilibrium after the initial fluctuation stage is 20-100 sec, and the “Penetration Zone” decreases with decreasing grain size over this time period.

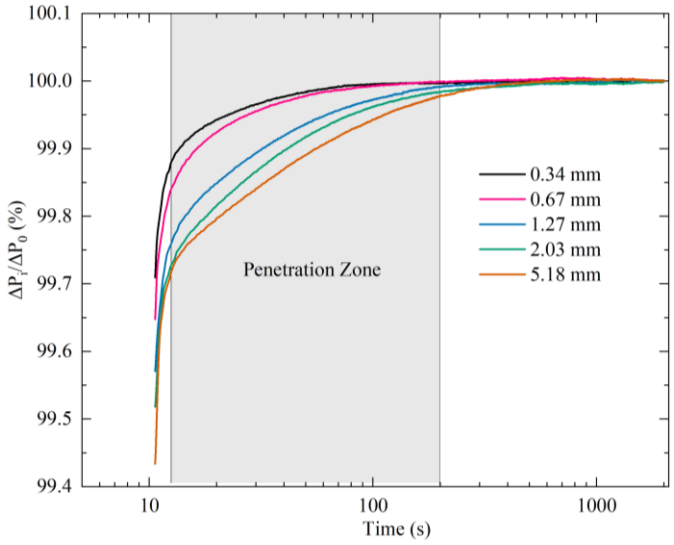

Fig. 5. Fitting region (the "Penetration Zone" in the shadowed area) for mudrock sample X-1 with different granular sizes; the penetration zone illustrating the pressure gradient mainly happens at 20 to 200 sec for this sample.

In fact, the "Penetration Zone", as an empirical period, is evaluated by the pressure change over a unit of time before gas is completely transported into the inner central part of the sample to reach the final pressure. Owing to the sample size limitation, a decreasing pressure could

cause multiple flow states (based on the Knudsen number) to exist in the experiment. The pressure during the GPT experiment varies between 50 and 200 psi (0.345 MPa to 1.38 MPa). Fig. 6 shows the Knudsen number calculated from different pressure conditions and pore diameters together with their potential flow state. Based on Fig. 6, the flow state of gas in the GPT experiments is mainly dominated by Fickian and transition diffusion. Essentially, the flow state change with pressure should be strictly evaluated through the Knudsen number in Fig. 6 to guarantee that the data in the "Penetration Zone" are always fitted with the GPT's constitutive equation for laminar or diffusive states. This helps obtain a linear trend for $ln(1-F_f)$ or ${F_s}^2$ versus time for low-permeability media. Experimentally, data from 30 to several 100 seconds are recommended for tight rocks like shales within the GPT methodology.

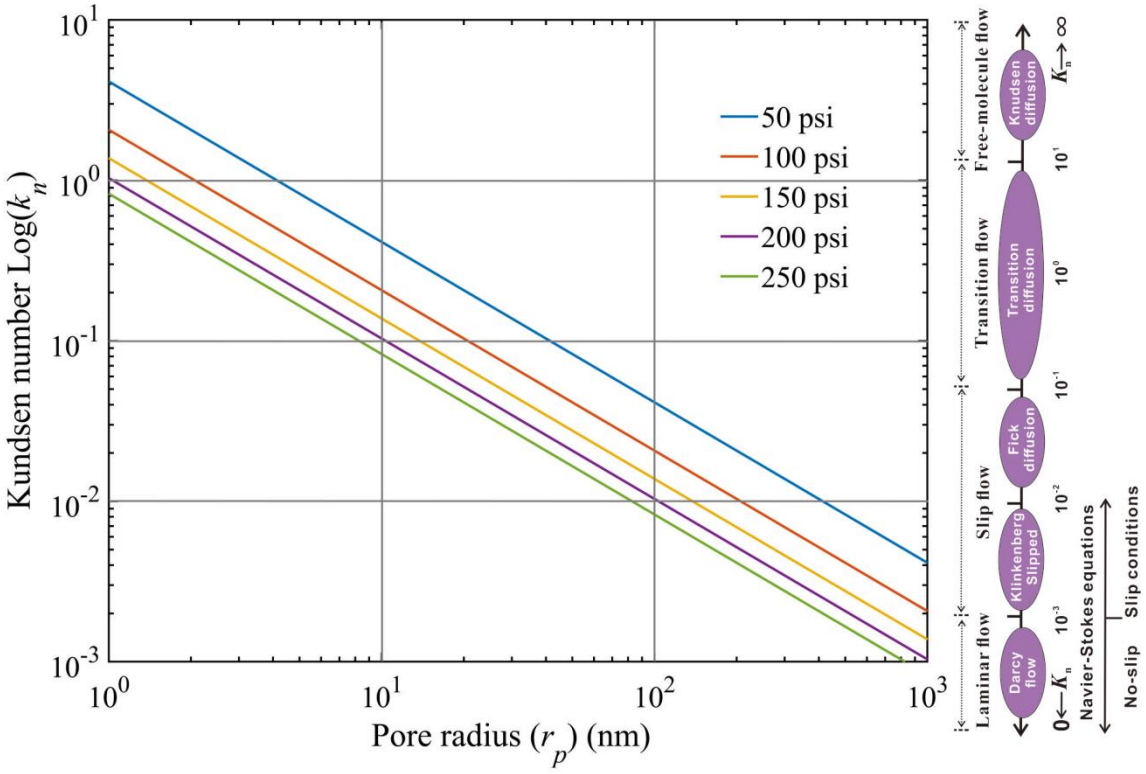

Fig. 6. Flow state of gas under diffferent testing pressures; modified from Chen & Pfender (1983)

and Roy et al. (2003) (Chen & Pfender, 1983; Roy et al., 2003).

In the GPT approach, as mentioned earlier, Eq. (S33) holds for small K_c values (e.g., < 10) so that the approximately equivalent void volume in the sample cell and sample pore volume would allow for sufficient pressure drop. It also gives time and allows the probing gas to expand into the matrix pores to have a valid "Penetration Zone" and to determine the permeability. Greater values of K_c would prevent the gas flow from entering into a slippage state as the pressure difference would increase with increasing K_c. However, large pressure changes would result in a turbulent flow (Fig. 6), which would cause the flow state of gas to be no longer valid for the constitutive equation of the GPT. Overall, the GPT solutions would be applicable to the gas permeability measurement, based on the diffusion-like process, from laminar flow to Fickian diffusion, after the correction of the slippage effect.

3. 3.4.2 Pressure decay behavior of four different probing gases

We used three inert gases, including He, N_2, and Ar, and one sorptive gas i.e., CO_2 (Busch et al., 2008), to compare the pressure drop behavior for sample size with an average granular diameter of 0.675 mm. Results for the mudrock sample X-2 are presented in Fig. 7. Among the three inert gases, helium and argon required the shortest and longest time to reach pressure equilibrium (i.e., He<N_2<Ar), respectively. In terms of pressure drop, argon exhibited the most significant decrease. In a constant-temperature system, the speed (or rate) at which gas molecules move is inversely proportional to the square root of their molar masses. Hence, it is reasonable that helium (with the smallest kinetic diameter of 0.21 nm) has the shortest equilibrium time. However, the pressure drop is more critical than the time needed to reach

equilibrium for the GPT, as the equilibrium time does not differ much (basically within 10 seconds for a given sample weight, except for the adsorptive CO_2). Argon may provide a wider range of valid Penetration Zones in a short time scale for its longest decay time except for adsorbed gas of CO_2; a choice of inert and economical gas is suggested for the GPT experiments.

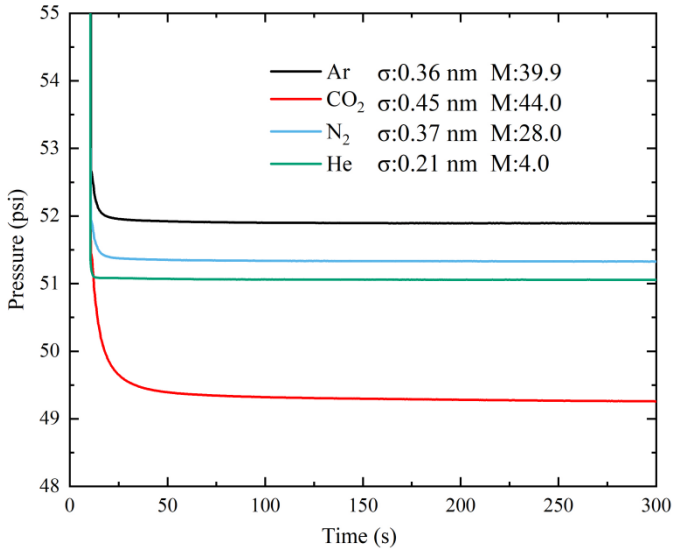

Fig. 7. Measured pressure decay curves from mudrock Sample X-2 for gases of different molecular diameters σ and molecular weights M (g/mol).

Fig. 7 shows that the pressure decay curve of the adsorptive gas CO_2 is different from those of the inert gases used in this study. CO_2 has a slow equilibrium process due to its large molar mass, and the greatest pressure drop among the four gases due to its adsorption effect. This additional flux needs to be taken into account to obtain an accurate transport coefficient. Accordingly, multiple studies including laboratory experiments (Pini, 2014) and long-term field observations (Haszeldine et al., 2006; Lu et al., 2009) were carried out to assess the sealing efficiency of mudrocks for CO_2 storage. In fact, the GPT can supply a quick and effective way

to identify the adsorption behavior of different mudrocks for both laminar-flow and diffusion states.

3. 3.4.3 Pressure decay behavior for different granular sizes

We compared the pressure drop behavior of gas in the mudrock Sample X-1 with different granular sizes (averaged from 0.34 mm to 5.18 mm) using the same sample weight and K_c. Results based on the experimental data shown in Fig. 8 indicate that a larger-sized sample would provide more data to be analyzed for determining the permeability. This is because the larger the granular size, and (1) the larger the pressure drop, (2) the longer the decay time as Fig. 8 demonstrates. This is consistent with the simulated results reported by Profice et al. (2012).

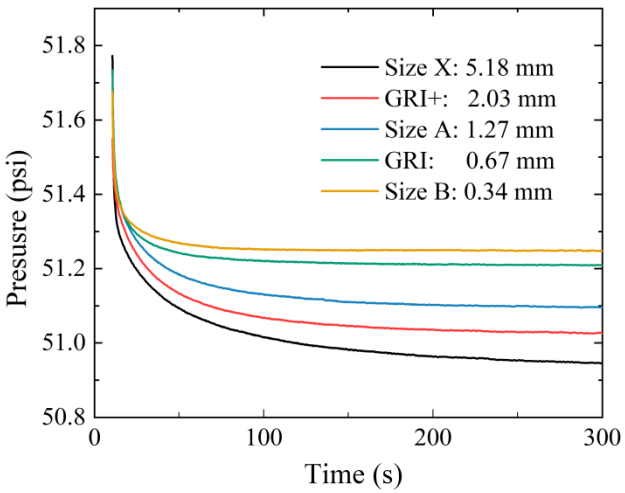

Fig. 8. Pressure decay curves measured by helium on sample X-1 with five different granular sizes. The intra-granular porosity was 5.8% independently measured by mercury intrusion porosimetry.

Table 2. Permeability results from the methods of GPT and SMP-200 for X-1.

Granular size (mm)	SMP-200 (nD) [§]	GPT test 1 (nD)[£]	GPT test 2 (nD)[£]	Average value (nD)[£]	Fitting duration (s)	Solution type	Dimensionless time	Particle density (g/cm^3)

5.18	-	1.17	1.17	1.17	50-100	ILT	0.023-0.027	2.631
2.03	14.2	0.45	0.41	0.43	50-100	LLT	0.026-0.028	2.626
1.27	-	0.10	0.10	0.10	30-60	ILT	CR*	2.673
0.67	0.65	0.08	0.04	0.06	30-60	LLT	CR*	2.658
0.34	-	0.02	-	0.02	30-60	IET	CR*	2.643

§ The results are from the SMP-200 using the GRI default method.

£ The results are from the GPT method we proposed.

* CR means the conflict results that the verified dimensionless time does not confirm the early- or late-time solutions using the solved permeability. For example, the verified dimensionless time would be > 0.024 using the early-time solution solved result and vice versa.

As reported in Table 2, the permeability values measured by the GPT method are one or two orders of magnitude greater than those measured by the SMP-200 instrument. The built-in functions of SMP-200 can only be used for two default granular sizes (500-841 μm for GRI and 1.70-2.38 mm for what we call GRI+) to manually curve-fit the pressure decay data and determine the permeability. The GRI method built in the SMP-200 only suggests the fitting procedure for data processing without publicly available details of underlying mathematics. The intra-granular permeabilities of mudrocks sample X-1 vary from 0.02 to 1.17 nD for five different granular sizes using the GPT. With the same pressure decay data selected from 30 to 200 sec, the permeability results for GRI and GRI+ sample sizes from the SMP-200 fitting are 0.65 and 14.2 nD, as compared to 0.06 and 0.43 nD determined by the GPT using the same mean granular size. Our results are consistent with those reported by Peng & Loucks (2016) who found two to three orders of magnitude differences between the GPT and SMP-200 methods (Peng & Loucks, 2016).

There exist several issues associated with granular samples with diameters smaller than on average 1.27 mm. First, the testing duration is short, and second, there would not be sufficient pressure variation analyzed in Fig. 8. Both may cause significant uncertainties in the

permeability calculation and, therefore, make samples with diameters smaller than 1.27 mm unfavorable for the GPT method, particularly extra-tight (sub-nD levels) samples, as there is almost no laminar or diffusion flow state to be captured. The greater pressure drop for larger-sized granular samples would result in greater pressure variation and wider data region compared to smaller granular sizes (see Figs. 6 and 9). Although samples of large granular sizes may potentially contain micro-fractures, which complicate the determination of true matrix permeability (Heller et al., 2014), the versatile GPT method can still provide size-dependent permeabilities for a wide range of samples (e.g., from sub-mm to 10 cm diameter full-size cores) (Ghanbarian, 2022a, 2022b). Besides, the surface roughness of large grains may also complicate the determination of permeability, which need to pay attention to (Devegowda, 2015; Rasmuson, 1985; Ruthven & Loughlin, 1971). Overall, our results demonstrated that sample diameters larger 2 mm are recommended for the GPT to determine the nD permeability of tight mudrocks, while smaller sample sizes may produce uncertain results.

4.4 Practical recommendations for the holistic GPT

Here, we evaluate the potential approximate solution for tight rock samples using frequently applied experimental settings by considering the critical parameters, such as sample mass, porosity, and estimated permeability (as compiled in Fig. 9 showing the dimensionless time versus porosity). Based on the results presented in Figs. 3 and 6, only $t < 200$s is dominant and critical for the analyses of dimensionless time and penetration zone. Thus, we take 200s and use helium to calculate the dimensionless time. Another critical parameter to assure enough decay data is the sample diameter greater than 2 mm. Thus, we only show the dimensionless

time versus porosity for sample diameter greater than the criteria of 2 mm.

Fig. 9 demonstrates that the sample permeability has dominant control on the early- or late-solution selection, and we decipher a concise criterial for three solutions selection. We classify the dimensionless time versus porosity relationship into three cases. Firstly, among the curves shown in Fig. 9, only that corresponding to k = 0.1 nD and sample diameter of 2 mm stays below the dashed line representing τ = 0.024. Therefore, the early time solution is appropriate for tight samples with permeabilities less than 0.1 nD (as shown in the analyses of Section 3.4.3, which also conforms to the situation of the molecular sieve sample that we tested in SI3). Secondly, for permeabilities greater than 10 nD (the curve is above the line of τ = 0.024), the new derived late-time solution, Eq. (3B), is recommended as it is more convenient for mathematical calculation without the consideration of transcendental functions. The reason is that the sample cell can be filled as much as possible (~90% of the volume) with samples and solid objects. However, as the tight rock hardly presents a large value of porosity, the small K_c value is difficult to be achieved with an inconsequential influence between Eq. (3B) and Eq. (3A). Lastly, in the case of permeability around 1 nD, the value of porosity would be critical in the selection of the early- or late-time solutions, as shown in Fig. 9.

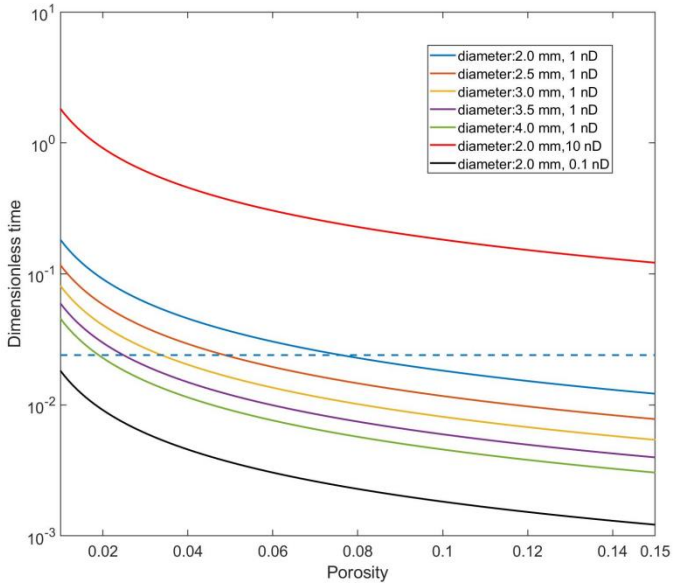

Fig. 9. Holistic GPT to explore the appropriate solution based on diameter, permeability, and porosity of samples. The legend shows the diameter of granular sample and permeability, along with a dashed line for dimensionless time of 0.024, while regions above and below this value fit for the late- and early-time solutions, respectively.

3.5. Conclusions

In the present work, we solved fluid flow state equation in granular porous media and provided three exact mathematical solutions along with their approximate ones for practical applications of low permeability measurements. The mathematical solutions for the transport coefficient in the GPT were derived for a spherical coordinate system, applicable from laminar flow to slippage corrected Fickian diffusion. Of the three derived solutions, one is valid during early times when the gas storage capacity K_c approaches infinity, while the other two are late-time solutions to be valid when K_c is either small or tends towards infinity. We evaluated the derived solutions for a systematic measurement of extra-low permeabilities in granular media

and crushed rocks using experimental methodologies with the data processing procedures. We determined the error for each solution by comparing with the exact solutions presented in the SI. The applicable conditions for such solutions of the GPT were investigated, and we provided the selection strategies for three approximate solutions based the range of sample permeability. In addition, a detailed utilization of GTP was given to build up the confidence in the GPT method through the molecular sieve sample, as it enables a rapid permeability test for ultra-tight rock samples in just tens to hundreds of seconds, with good repeatability.

Nomenclature

B_{ij} Correction parameter for viscosity, constant

c_t Fluid compressibility, Pa^{-1}

D Diffusion coefficient, m^2/s

F_f Uptake rate of gas outside the sample, dimensionless

F_s Uptake rate in the sample, dimensionless

f_1 Intercept of Eq. (S40), constant

J Physical flux, unit for certain physical phenomenon

K_a Apparent transport coefficient defined as Eq. (S9), m^2/s

K_c Ratio of gas storage capacity of the total void volume of the system to the pore (including adsorptive and non-adsorptive transport) volume of the sample, fraction

K_f Initial density state of the system, fraction

k Permeability, m^2

k_s Permeability defined as Eq. (S8), $m^2/(pa{\cdot}s)$

L Coefficient, unit for certain physical transport phenomenon

M Molar mass, kg/kmol

M_m Molar mass of the mixed gas, kg/kmol

$M_{i,j}$ Molar mass for gas i or j, kg/kmol

M_s Total mass of sample, kg

N Particle number, constant

p Pressure, Pa

p_{cm} Virtual critical pressure of mixed gas, Pa

p_p Pseudo-pressure from Eq. (S1), Pa/s

R_a Particle diameter of sample, m

R Universal gas constant, 8.314 J/(mol·K)

r Diameter of sample, m

s_1 Slope of Eq. (S40), constant

s_2 Slope of function $Ln(1 - F_s)$, constant

s_3 Slope of function ${F_s}^2$, constant

T Temperature, K

T_{cm} Virtual critical temperature for mixed gas, K

t Time, s

U_f Dimensionless density of gas outside the sample, dimensionless

U_s Dimensionless density in grain, dimensionless

U_∞ Maximum density defined as Eq. (S37), dimensionless

V_1 Cell volume in upstream of pulse-decay method, m^3

V_2 Cell volume in downstream of pulse-decay method, m^3

V_b Bulk volume of sample, m^3

V_c Total system void volume except for sample bulk volume, m^3

$\overline{v}$ Dacian velocity in pore volume of porous media, m/s

X Pressure force, Pa

$y_{i,j}$ Molar fraction for gas i or j, fraction

z Gas deviation (compressibility) factor, constant

Greek Letters:

α_n The nth root of Eq. (S30), constant

μ Dynamic viscosity, pa·s or $N{\cdot}s/m^2$

$\mu_{i,j}$ Dynamic viscosity for gas i or j, pa·s or $N{\cdot}s/m^2$

μ_{mix} Dynamic viscosity of mixture gas, pa s or N s/m^2

μ_p Correction term for the viscosity with pressure, pa s or N s/m^2

ξ Dimensionless radius of sample, dimensionless

ρ Density of fluid, kg/m^3

ρ_0 Average gas density on the periphery of sample, kg/m^3

ρ_1 Gas density in reference cell, kg/m^3

ρ_2 Gas density in sample cell, kg/m^3

ρ_b Average bulk density for each particle, kg/m^3

ρ_f Density of gas changing with time outside sample, $kg{\cdot}m^{-3}{\cdot}s^{-1}$

$\rho_{f\infty}$ Maximum value of ρ_f defined as Eq. (S38), $kg{\cdot}m^{-3}{\cdot}s^{-1}$

ρ_p Pseudo-density from Eq. (S1), $kg{\cdot}m^{-3}{\cdot}s^{-1}$

ρ_s Density of gas changing with time in sample, kg·m^{-3}·s^{-1}

ρ_{ps} Pseudo-density of gas changing with time in sample, kg·m^{-3}·s^{-1}

ρ_{pf} Pseudo-density of gas changing with time outside sample, kg·m^{-3}·s^{-1}

ρ_{p2} Initial pseudo-density of gas in sample, kg·m^{-3}·s^{-1}

ρ_{p0} Average pseudo-density of gas on sample periphery, kg·m^{-3}·s^{-1}

ρ_{rm} Relative density to the mixed gas, kg·m^{-3}·s^{-1}

ρ_{sav} Average value ofρ_{sr}defined as Eq. (S47), kg·m^{-3}·s^{-1}

ρ_{sr} Average value of pseudo-density of sample changing with diameter, kg·m^{-3}·s^{-1}

$\rho_{s\infty}$ Maximum value of ρ_{sr} defined as Eq. (S46), kg·m^{-3}·s^{-1}

τ Dimensionless time, dimensionless

ϕ Sample porosity, fraction

ϕ_f Total porosity ($\phi_f = \phi_a + \phi_b$) occupied by both free and adsorptive fluids, fraction

Supporting Information (SI)

SI1. Consideration of Non-linearity of Gas and Solutions for a Mixed Gas State

For gas flow, we can use a pseudo-pressure variable to linearize Eq. (1D) as μ and c_t are functions of pressure. Thee pseudo-pressure p_p is defined as (Haskett et al., 1988)

$$p_p = 2\int_{p_0}^{p} \frac{p}{\mu z} d\,p \tag{S1}$$

By combining Eq. (S1) with the ideal gas law, the pseudo-density may be expressed as

$$\rho_p = \frac{pM}{RT} = \frac{p^2 M}{\mu z RT} \tag{S2}$$

Because viscosity and compressibility do not change significantly (less than 0.7%) between 200 psi and atmospheric pressures, Eq. (S2) can be simplified to

$$\rho_p = \frac{p^2 M}{RT} \tag{S3}$$

Thus, the density change is replaced by the pseudo-density for a precise calibration by using pressure squared.

During the GPT experiment, different gases in the reference and sample cells may complicate the hydrodynamic equilibrium of gas, and consequently the expression of transport phenomena, as the viscosity and gas compressibility are in a mixed state. Therefore, during the GPT experiment when a different gas exists between the reference and sample cells a, a mixed viscosity should be used after the gas in reference cell is released into the sample cell. The viscosity of mixture μ_{mix} under pressure in Eqs. (3A)-(3C) can be calculated from (Brokaw, 1968; Sutherland, 1895)

$$\mu_{mix} = \sum \frac{\mu_i}{1+\frac{1}{y_i}\left(\sum_{\substack{j=1 \\ j\neq i}}^{n} B_{ij} y_j\right)} + \mu_p \tag{S4}$$

B_{ij} is a correction parameter independent of gas composition and can be expressed as

$$B_{ij} = \frac{[1 + (\frac{\mu_i}{\mu_j})^{0.5}(\frac{M_j}{M_i})^{0.5}]^2}{2\sqrt{2}(1 + \frac{M_j}{M_i})^{0.5}} \tag{S5}$$

in which μ_p is the correction term for the viscosity variation as its changes with pressure and given by

$$\mu_p = 1.1 \times 10^{-8}\left(e^{1.439\rho_{rm}} - e^{-1.111{\rho_{rm}}^{1.858}}\right) \times {M_m}^{0.5} \cdot \frac{{P_{cm}}^{\frac{2}{3}}}{{T_{cm}}^{\frac{1}{6}}} \tag{S6}$$

SI2. Gas Transport in GPT

From Eq. (1D), the transport of gas in the GPT with the "unipore" model under a small pressure gradient in a spherical coordinate system with laminar flow is based on the Darcy-type relation. Because the transfer rate of the fluid is proportional to the concentration gradient, this process can be expressed as:

$$\frac{\partial \rho_p}{\partial t} = \frac{k}{c_t \phi_f \mu}\left(\frac{2}{r}\frac{\partial \rho_p}{\partial r} + \frac{\partial^2 \rho_p}{\partial r^2}\right) \tag{S7}$$

We set

$$k_s = \frac{k}{\mu} \tag{S8}$$

$$K_a = \frac{k_s}{c_t \phi_f} \tag{S9}$$

Then, Eq. (S7) becomes:

$$\frac{\partial \rho_p}{\partial t} = K_a \left(\frac{2}{r} \frac{\partial \rho_p}{\partial r} + \frac{\partial^2 \rho_p}{\partial r^2} \right) \text{ or } \frac{\partial}{\partial t}(\rho_p r) = K_a \frac{\partial^2}{\partial r^2}(\rho_p r) \tag{S10}$$

We next introduce the following dimensionless variables:

$$U_s = \frac{r}{R} \frac{(\rho_{ps} - \rho_{p2})}{(\rho_{p0} - \rho_{p2})} \tag{S11}$$

$$U_f = \frac{\rho_{pf} - \rho_{p2}}{\rho_{p0} - \rho_{p2}} \tag{S12}$$

$$\xi = \frac{r}{R} \tag{S13}$$

$$\tau = \frac{K_a t}{R^2} \tag{S14}$$

where ρ_1 and ρ_2 are the gas density in the reference and sample cells, and ρ_0 is the gas density outside the connected pore volume (the gas has flowed from the reference into sample cells but not into samples), and ρ_0 is given by

$$\rho_0 = \frac{V_1 \rho_1 + (V_2 - V_b)\rho_2}{V_c} \tag{S15}$$

where V_1 is the reference cell volume, V_2 is the sample cell volume, V_b is the bulk volume of the sample, V_c is the total void volume of the system minus V_b where $V_c = V_1 + V_2 - V_b$.

If the bulk density of the sample is ρ_b and the total mass of the sample is M_s, then the total number of sample particles N is:

$$N = \frac{M_s}{\frac{4}{3}\pi {R_a}^3 \rho_b} \tag{S16}$$

Based on Darcy's law, the gas flow into a sample Q is:

$$Q = -4\pi R^2 \left(k_s \frac{\partial p}{\partial r}\right) N = -\frac{3}{R}\frac{M_s}{\rho_b} k_s \frac{\partial p}{\partial r} \tag{S17}$$

According to mass conservation and in combination with Eq. (S17), for $t > 0$ and $r = R_a$, we have

$$-\frac{3}{R} V_b K_a c_t \phi_f \frac{\partial p}{\partial r} \rho_s = V_c \frac{\partial \rho_f}{\partial t} \tag{S18}$$

Substituting Eq. (1C) into Eq. (S18), the boundary condition of Eq. (S10), for ξ =1, is:

$$-\frac{3}{R} V_b K_a \phi_f \frac{\partial \rho_s}{\partial r} = V_c \frac{\partial \rho_f}{\partial t} \tag{S19}$$

Substituting dimensionless variables into Eq. (S10) yields:

$$\frac{\partial U_s}{\partial \tau} = \frac{\partial^2 U_s}{\partial \xi^2} \tag{S20}$$

By defining parameter K_c as:

$$K_c = \frac{V_c}{V_b \phi_f} \tag{S21}$$

the boundary condition of Eq. (S19) becomes:

$$\frac{\partial U_f}{\partial \tau} = -\frac{3}{K_c}\left(\frac{\partial U_s}{\partial \xi} - \frac{U_s}{\xi}\right) \tag{S22}$$

From Eq. (S21), K_c represents the ratio of gas storage capacity of the total void volume of system to the pore volume (including both adsorption and non-adsorption volume) of sample.

The initial condition of Eq. (S20), for $\tau = 0$, is:

$$0 \le \xi < 1, U_s = 0 \tag{S23}$$

For $\tau > 0$:

$$\xi = 0, U_s = 0 \tag{S24}$$

$$\xi = 1, U_s = U_f = 1 \tag{S25}$$

$$\frac{\partial U_s}{\partial \tau} = \frac{\partial^2 U_s}{\partial \xi^2}, 0<\xi < 1 \tag{S26}$$

Replacing the Heaviside operator $p = \partial/\partial\tau$ as $p = -s^2$. Eq. (S20) and Eq. S(22) then become:

$$\frac{\partial^2 U_s}{\partial \xi^2} + s^2 U_s = 0\Big|_{U_s=0,\xi=0} \tag{S27}$$

$$\alpha^2(U_s - 1) = \frac{3}{K_c}\left(\frac{\partial U_s}{\partial \xi} - \frac{U_s}{\xi}\right)\Big|_{\xi=1} \tag{S28}$$

For these first- and second-order ordinary differential equations, we can solve Eqs. (S27) and (S28) as:

$$U_s = \frac{\alpha^2 \sin \alpha \xi}{\frac{3}{K_c}(\sin \alpha - \alpha \cos \alpha) + \alpha^2 \sin \alpha} \tag{S29}$$

In Eq. (S29), α_n are the roots of Eq. (S30):

$$\tan \alpha = \frac{3\alpha}{3 + \alpha^2 K_c} \tag{S30}$$

Defining the numerator and denominator of Eq. (S29) as functions $f(\alpha)$ and $F(\alpha)$, U_s can be expressed as:

$$U_s = \underset{\alpha\to 0}{F}\frac{f(\alpha)}{F(\alpha)} + 2\sum_{n=1}^{\infty}\frac{f(\alpha_n)}{\alpha_n F'(\alpha_n)} e^{-{\alpha_n}^2 \tau} \tag{S31}$$

SI2-1: Solution for the Limited K_c Value

Under the condition of limited K_c value, Eq. (S20) is solved with the boundary condition of $0 < \xi < 1$ at time t, and the gas state on the grain surface is initially at equilibrium with the gas outside. Using the Laplace transform, Eq. (S31) is given as (the Laplace transform part can be found in APPENDIX V of Carslaw & Jaeger, 1959) (Carslaw & Jaeger, 1959):

$$U_s = \frac{\xi K_c}{K_c + 1} + 6 \sum_{n=1}^{\infty} \frac{sin\, \xi\, \alpha_n}{sin\, \alpha_n} \frac{K_c e^{-{\alpha_n}^2 \tau}}{9(K_c + 1) + {\alpha_n}^2 {K_c}^2} \tag{S32}$$

As the pressure transducer detects the pressure in the reference cell, with the boundary condition $U_f = U_s|_{\xi=1}$, we can calculate U_f as:

$$U_f = \frac{K_c}{1 + K_c} + 6 \sum_{n=1}^{\infty} \frac{K_c e^{-{\alpha_n}^2 \tau}}{9(K_c + 1) + {\alpha_n}^2 {K_c}^2} \tag{S33}$$

For a convenient expression of α_n through logarithmic equation, Eq. (S33) can be transformed as:

$$\left(1 - U_f\right)(1 + K_c) = 1 - 6 \sum_{n=1}^{\infty} \frac{K_c(1 + K_c) e^{-{\alpha_n}^2 \tau}}{9(K_c + 1) + {\alpha_n}^2 {K_c}^2} \tag{S34}$$

The left side of Eq. (S34) clearly has a physical meaning for the state of gas transport outside the sample, and we define $(1 - U_f)(1 + K_c)$ as F_f, which is less than, but infinitely close to, 1. Parameter F_f represents (1) the fraction of final gas transfer of V_c which has taken place by time *t*, which can be interpreted as the net change in the density of gas at time *t* to time infinity as Eq. (S35), or (2) as the fractional approach of the gas density to its steady-state in terms of dimensionless variables as Eq. (S36).

$$F_f = \frac{\rho_{p0} - \rho_{pf}}{\rho_{p0} - \rho_{f\infty}} \tag{S35}$$

Or:

$$F_f = \frac{1 - U_f}{1 - U_\infty} = \frac{\rho_{p0} - \rho_{pf}}{\rho_{p0} - \rho_{p2}}(1 + K_c) \tag{S36}$$

where for $\tau \to \infty$, the result of U_f and $\rho_{f\infty}$would tend to be the limiting value:

$$U_\infty = U_s = U_f \xi = \frac{\xi K_c}{1 + K_c}\Big|_{\xi=1} \tag{S37}$$

$$\rho_{f\infty} = \frac{V_1\rho_1 + (V_2 - V_s)\rho_2}{V_1 + V_2 - V_s} = \frac{K_c}{1 + K_c}\left(\rho_{p0} - \rho_{p2}\right) + \rho_{p2} \tag{S38}$$

Thus, Eq. (S34) can be expressed as:

$$F_f = 1 - 6\sum_{n=1}^{\infty} \frac{K_c(1 + K_c)e^{-{\alpha_n}^2\tau}}{9(K_c + 1) + {\alpha_n}^2{K_c}^2} \tag{S39}$$

For calculating the permeability, Eq. (S39) can be linearized as a function of time as there are no variables other than the exponential part:

$$ln(1 - F_f) = f_1 - s_1 t \tag{S40}$$

where f_1 is the intercept for the y-axis of function (S40):

$$f_1 = Ln[\frac{6K_c(1 + K_c)}{9(1 + K_c) + {\alpha_1}^2{K_c}^2}] \tag{S41}$$

The slope s_1 can be captured by the fitted line of the linear segment, and α_1 is the first solution of Eq. (S30):

$$s_1 = \frac{{\alpha_1}^2 K_a}{{R_a}^2} \tag{S42}$$

Thus, the permeability can be calculated as:

$$k = \frac{{R_a}^2 \mu c_t \phi_f s_1}{{\alpha_1}^2} \tag{S43}$$

SI2-2: Solution for K_c Goes to Infinity

When V_c has an infinite volume compared to the void volume in a sample, which means that the density of gas in V_c would be kept at ρ_{p0}, and α would approach $n\pi$ in Eq. (S30), then Eq. (S32) can be transformed as:

$$U_s = \xi + \frac{2}{\pi}\sum_{n=1}^{\infty}(-1)^n \frac{sin\, n\, \pi\xi}{n} e^{-(n\pi)^2\tau} \tag{S44}$$

In this situation, $U_f = 1$, and as the gas density would be maintained at the initial state at ρ_{p0}, it would be a familiar case in diffusion kinetics problems with the uptake rate of F_f to be expressed as F_s in V_b (Barrer, 1941):

$$F_s = \frac{\rho_{s\mathrm{av}}}{\rho_{s\infty}} \tag{S45}$$

where $\rho_{s\mathrm{av}}$ is the average value of ρ_{sr} in the grain, and $\rho_{s\infty}$ is the maximum value of ρ_{sr}:

$$\rho_{sr} = \rho_{ps} - \rho_{p2},\ \ \rho_{s\infty} = \rho_{p0} - \rho_{p2} \tag{S46}$$

The value of ρ_{sr} in the grain is:

$$\rho_{sav} = \frac{3}{R^3}\int_0^R \rho_{sr} r^2\, d\, r \tag{S47}$$

Then F_s becomes:

$$F_s = \frac{3}{R^3}\int_0^R \frac{U_s}{\xi} r^2\, d\, r \tag{S48}$$

Substituting Eq. (S44) into Eq. (S48), we can calculate:

$$F_s = 1 - \frac{6}{\pi^2}\sum_{n=1}^{\infty}\frac{e^{-(n\pi)^2\tau}}{n^2} \tag{S49}$$

Similar to Eq. (S39), Eq. (S49) can also be linearized to calculate the permeability in τ from the fitted slope. For $\tau \geq 0.08$, Eq. (S49) can be reduced as:

$$F_s = 1 - \frac{6}{\pi^2}e^{-\pi^2\tau} \tag{S50}$$

When t is small enough (for $\tau \leq 0.002$), Eq. (S49) can be transformed into Eq. (S51).

$$F_s = 6\sqrt{\frac{\tau}{\pi}} \tag{S51}$$

As F_s is a special solution of F_f with the case of K_c goes to infinity, we can arrive at:

$$F_s = F_f = \left(1 - U_f\right)(1 + K_c) \tag{S52}$$

For testing the ultra-low permeability rocks using granular samples whenK_c goes to infinity, Eq. (S50) and Eq. (S51) can be selected using different τ values.

From the fitted slope s_2 of function $ln(1 - F_s)$ from Eq. (S50), we can then derive the permeability:

$$k = \frac{{R_a}^2\mu c_t\phi_f s_2}{\pi^2} \tag{S53}$$

The results of Eq. (S53) are very similar to Eq. (S43) as the first solution for Eq. (S30) is very close to π.

From the fitted slope s_3 of function ${F_s}^2$ from Eq. (S51), we can derive the permeability:

$$k = \frac{\pi{R_a}^2\mu c_t\phi_f s_3}{36} \tag{S54}$$

SI3. A Case of Data Processing for GPT

We show here an illustration of the data processing procedure for the GPT with a molecular sieve sample (https://www.acsmaterial.com/molecular-sieves-5a.html). This material consists of grains of 2 mm in Diameter with a porosity of 26.28%, and a uniform pore-throat size of 5Å in Diameter, with a particle density of 2.96 g/cm^3. For a 45 g sample, the K_c value is 19.4 from Eq. (S21), and therefore 4.9% of the density ratio $(1 - K_f)$ is available for mass transfer from Eq. (4).

The experimental data were captured under a strict temperature control and unitary-gas environment, along with a precise measurement of barometric pressure. The experiment was run twice, and after the data were collected, 1) we made a rough evaluation of the "Penetration Zone" of this sample based on Figs. 5-6. For this molecular sieve sample, the "Penetration Zone" is shown in Fig. S1, and the mass transfer in unit time more conforming to a linear state (shown as Fig. 5) over a large time range, especially at 100-300s; 2) data in the selected range (100-300s) were fitted respectively for the slope from Fig. S2, then slopes were compiled in Table SI3-1; 3) permeabilities were calculated using the slope of the fitted curve, and all results for LLT, ILT and IET are also shown in Table SI3-1; 4) the results were checked with their dimensionless times to verify whether the early- or late-time solutions were used correctly. Table SI3-1 clearly shows that the results of IET should be selected for this sample, as the dimensionless time is less than 0.024. Note that the data fluctuation shown here was from a high resolution ($\pm$0.1% for 250 psi) pressure sensor without undergoing a smoothing process; meanwhile, for data in the 100-200, 200-300, and 300-400 seconds of experimental duration,

100, 200, and 300 seconds respectively were used to calculate the dimensionless times for the results in Table SI3-1.

In addition, the validity of the permeability obtained needs to be verified by using the time interval employed in data fitting and the calculated permeability results to calculate the τ (Table SI3-1). If the dimensionless time is less than 0.024 (as occurred for the case of molecular sieve), the IET solution is selected; if the dimensionless time is greater than 0.024 and K_c is greater than 10, the ILT solution is used; if τ is greater than 0.024 and K_c is less than 10, then the LLT solution is employed. However, for sample sizes smaller than 1.27 mm, Conflicting Results (described in Table 1) occur, and results from this situation are not recommended due to poor data quality.

Table SI3-1. Permeability results of molecular sieve from LLT, IET and ILT

Fitting range (s)	LLT (m^2)	τ -LLT	IET(m^2)	τ -IET	ILT (m^2)	τ -ILT	Slope-LLT	Slope-IET	Slope-ILT
100-200	5.60E-22	0.004	1.02E-21	0.007	5.00E-22	0.003	0.0004	0.0007	0.0004
200-300	4.20E-22	0.006	5.81E-22	0.008	3.75E-22	0.005	0.0003	0.0004	0.0003
300-400	2.80E-22	0.006	4.36E-22	0.009	2.50E-22	0.005	0.0002	0.0003	0.0002

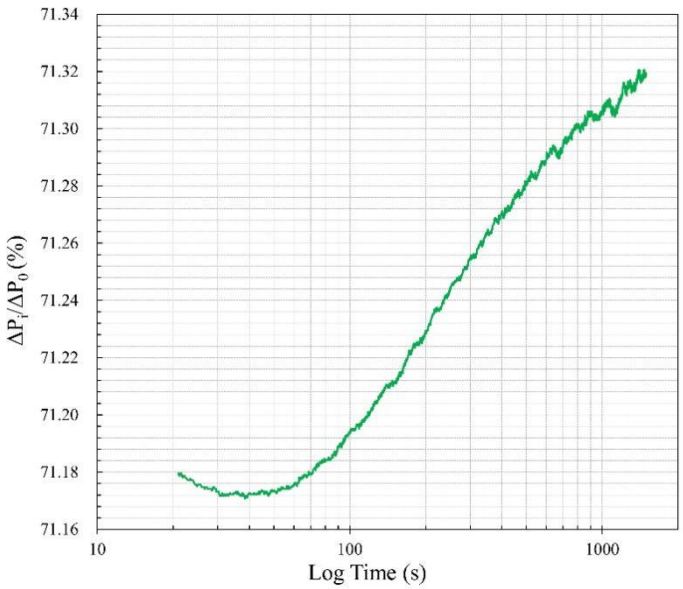

Fig. S1. Unit pressure change varying with experimental time.

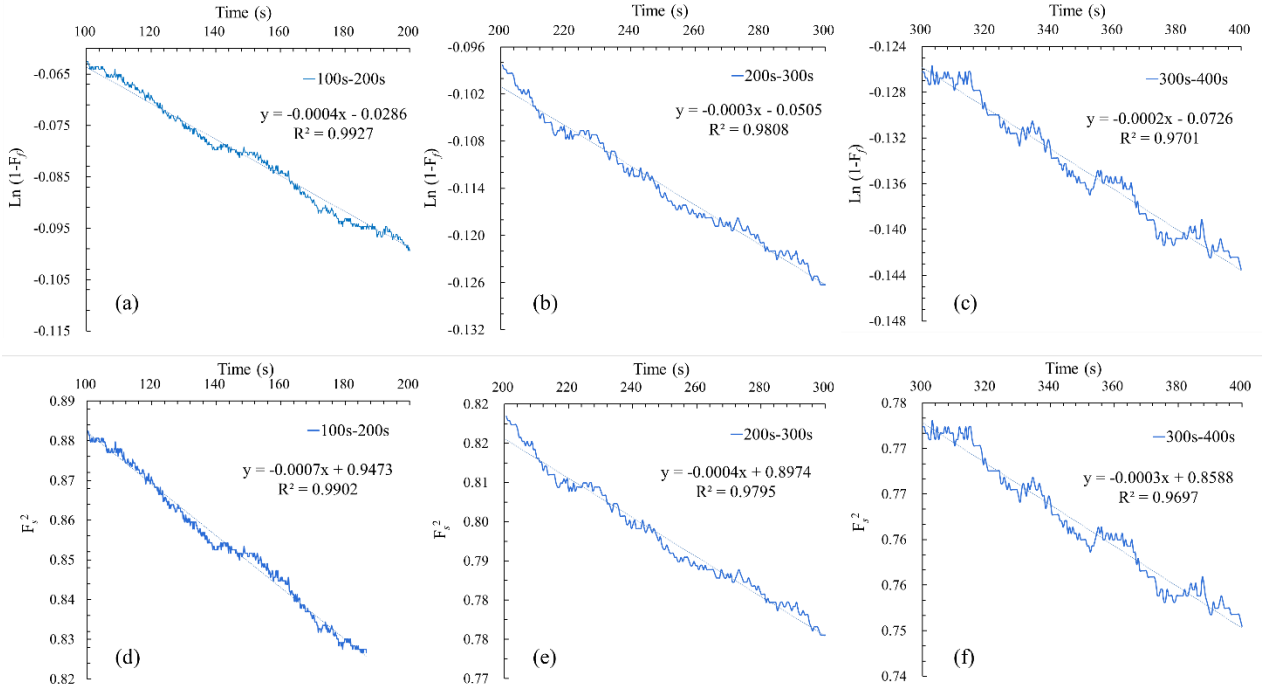

Fig. S2. Fitted slopes for each solution; (a) to (c) are results of LLT and ILT, while (d) to (f) of IET.

SI4. Equipment and samples

The experimental setup in the GPT presented in this study is based on the GRI-95/0496 protocols (Guidry et al., 1996) and the SMP-200 guidelines from Core Laboratories with the gas expansion approach (shown in Fig. S3). In this work, gases (He, Ar, N_2, or CO_2) with different molecular sizes and sorption capacities were tested using two shale core samples (X1, X2) from an oil-producing lacustrine formation in the Songliao Basin, China. X1 is used for sample size study where X2 used for experiment with different gas. Also, we used the molecular sieve to exhibit the practical utilization of the GPT method in SI3. We gently crushed

the intact samples with mortar and ground to different granular sizes from 0.34 mm to 5.18 mm through a stack of sieves (named here as Size X: 8 mm to #8 mesh; GRI+: #8-#12 mesh; Size A: #12-#20 mesh; GRI: #20-#35 mesh; Size B: #35-#80 mesh).

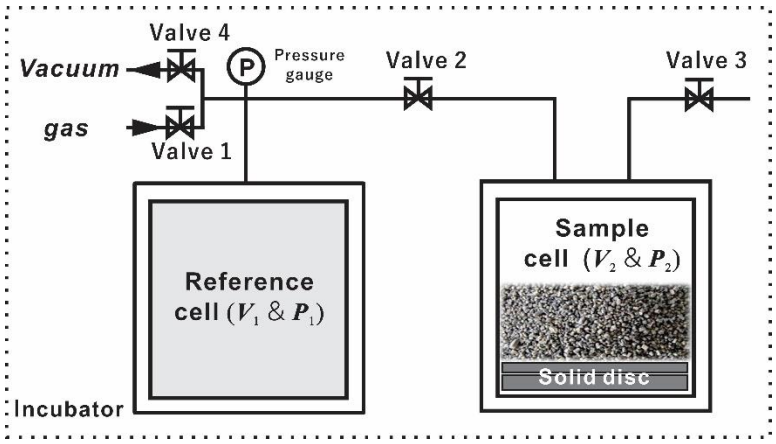

Fig. S3. Scheme of the GPT experiment for granular samples with all the cells and supplies placed inside an incubator for temperature control.

After loading each sample, related accessories (e.g., solid discs or balls for volume control; and hence porosity, sample mass, and solution-related) were placed below samples inside the cell (Fig. S3). Next, valves 1 and 3 were closed, then valves 2 and 4 were opened for air evacuation. Using a precise pressure gauge connected to the reference cell shown in Fig. S3 we monitored changes in the pressure. The evacuation time typically lasted at least 15-30 min, and then the system was allowed to stabilize for another 15 min. As the moisture content of the samples significantly influences the final vacuum, the samples were placed into the sample cell immediately after removal from the drying oven set at 60^{o}C for two days and cooling in a low-humidity desiccator.

The experiments were conducted at the temperature of 35°C by placing the SMP-200 inside an incubator equipped with a high precision temperature-humidity sensor to monitor changes.

This is to ensure that the system temperature was always stable (0.05°C over at least 45 mins of experimental duration). For temperature monitoring, after evacuation, we closed valves 3 and 4 followed by opening valves 1 and 2 (shown in Fig. S3) and monitoring the heat convection and conduction in the system with the pressure gauge. Normally, the sample was placed inside the sample cell in less than 30 sec after opening the incubator and remained at least 45 min for the gas pressure to stabilize before the pressure decay test. After the pressure was stabilized (0.005 psi for an experimental pulse pressure of 200 psi), it was deemed that there was no appreciable additional flow due to temperature variation in the system, as indicated by the rebound of the pressure decay curve. After reaching a unitary gas condition and stable temperature in the GPT experiment, valves 2 and 4 were closed, and the reference cell was filled with the probing gas (mostly non-reactive helium) at 200 psi. Valve 2 was then opened to release the pressure in the reference cell into the void volume in the sample cell, and the pressure decay for both reference and sample cells were recorded over time.

SI5. Experimental conditions

We performed leakage tests by measuring the pressure variation with non-porous solids, such as steel balls, as any leakage would cause pressure variations and, accordingly, errors in permeability measurements of tight porous samples (Heller et al., 2014). Before the data from porous samples were analyzed, the leakage pressure from the steel ball experiment was subtracted from the sample data to correct the modest (<5% of the pressure levels used for permeability analyses) leakage effect.

The need for a unitary gas environment (a single gas used in both reference and sample cells)

is needed to successfully measure permeability via the GPT method. The relative movement of gas molecules in the mass transfer process is driven by the gas density gradient in the system. During gas transport, the pressure variance was recorded and used to obtain the permeability coefficient. However, when the gas in both cells is different, e.g., helium in the reference and air in the sample cells, the mathematical analysis requires a complicated correction accounting for the mean molar mass and the average gas dynamic viscosity of the gas mixture. In this study, we present the calculation with the viscosity of mixed gases for the GPT in the SI1. Since the mixed gas environment is not recommended, air evacuation should be used for a well-controlled unitary gas environment in the GPT.

A stable temperature is another critical point to ensure the success of the GPT experiment. A sensitive pressure transducer in combination with the ideal gas law, used to establish the relationship between pressure and gas volume change, would be a much more convenient and precise way than the gas flow meter to determine the gas permeability considering the measurement accuracy. According to Amonton's law (Gao et al., 2004), the kinetic energy of gas molecules is determined by the temperature, and any changes would alter the molecular collision force causing a pressure variation and a volumetric error. The GPT experiments were run two or three times on the same sample, and the sample skeletal density at the end of the experiment were obtained to check the overall indication of leakage and temperature control. The experimental data with relatively large and stable skeletal density (mostly the last run, from small but appreciable pressure change to reach stable values) were used.

References

1. Abdassah, D., & Ershaghi, I. (1986). Triple-porosity systems for representing naturally fractured reservoirs. Spe Formation Evaluation, 1(02), 113-127.
2. Barrer, R. M. (1941). Diffusion in and through solids. Рипол Классик.
3. Bibby, R. (1981). Mass transport of solutes in dual-porosity media. Water Resources Research, 17(4), 1075-1081.
4. Bock, H., Dehandschutter, B., Martin, C. D., Mazurek, M., De Haller, A., Skoczylas, F., & Davy, C. (2010). Self-sealing of fractures in argillaceous formations in the context of geological disposal of radioactive waste
5. Brace, W. F., Walsh, J. B., & Frangos, W. T. (1968). Permeability of granite under high pressure. Journal of Geophysical Research, 73(6), 2225-2236. http://doi.org/10.1029/JB073i006p02225
6. Brokaw, R. S. (1968). Viscosity of gas mixtures (Vol. 4496). National Aeronautics and Space Administration.
7. Busch, A., Alles, S., Gensterblum, Y., Prinz, D., Dewhurst, D. N., Raven, M. D., Stanjek, H., & Krooss, B. M. (2008). Carbon dioxide storage potential of shales. International Journal of Greenhouse Gas Control, 2(3), 297-308.
8. Carslaw, H. S., & Jaeger, J. C. (1959). Conduction of heat in solids.
9. Chen, X., & Pfender, E. (1983). Effect of the Knudsen number on heat transfer to a particle immersed into a thermal plasma. Plasma Chemistry and Plasma Processing, 3(1), 97-113.
10. Civan, F., Devegowda, D., & Sigal, R. F. (2013, 2013-1-1). Critical evaluation and

improvement of methods for determination of matrix permeability of shale. Paper presented at the.

11. Cui, X., Bustin, A., & Bustin, R. M. (2009). Measurements of gas permeability and diffusivity of tight reservoir rocks: different approaches and their applications. Geofluids, 9(3), 208-223.
12. Devegowda, D. (2015, 2015-1-1). Comparison of shale permeability to gas determined by pressure-pulse transmission testing of core plugs and crushed samples. Paper presented at the.
13. Egermann, P., Lenormand, R., Longeron, D. G., & Zarcone, C. (2005). A fast and direct method of permeability measurements on drill cuttings. Spe Reservoir Evaluation & Engineering, 8(04), 269-275.
14. Fakher, S., Abdelaal, H., Elgahawy, Y., & El-Tonbary, A. (2020, 2020-1-1). A Review of Long-Term Carbon Dioxide Storage in Shale Reservoirs. Paper presented at the.
15. Gao, J., Luedtke, W. D., Gourdon, D., Ruths, M., Israelachvili, J. N., & Landman, U. (2004). Frictional forces and Amontons' law: from the molecular to the macroscopic scale: ACS Publications.
16. Gensterblum, Y., Ghanizadeh, A., Cuss, R. J., Amann-Hildenbrand, A., Krooss, B. M., Clarkson, C. R., Harrington, J. F., & Zoback, M. D. (2015). Gas transport and storage capacity in shale gas reservoirs – A review. Part A: Transport processes. Journal of Unconventional Oil and Gas Resources, 12, 87-122. http://doi.org/https://doi.org/10.1016/j.juogr.2015.08.001
17. Ghanbarian, B. (2022a). Estimating the scale dependence of permeability at pore and core

scales: Incorporating effects of porosity and finite size. Advances in Water Resources, 161, 104123.

18. Ghanbarian, B. (2022b). Scale dependence of tortuosity and diffusion: Finite-size scaling analysis. Journal of Contaminant Hydrology, 245, 103953.
19. Ghanbarian, B., Hunt, A. G., & Daigle, H. (2016). Fluid flow in porous media with rough pore-solid interface. Water Resources Research, 52(3), 2045-2058.
20. Guidry, K., Luffel, D., & Curtis, J. (1996). Development of laboratory and petrophysical techniques for evaluating shale reservoirs. Final technical report, October 1986-September 1993: ResTech Houston, Inc., TX (United States).
21. Gutierrez, M., Øino, L. E., & Nygaard, R. (2000). Stress-dependent permeability of a de-mineralised fracture in shale. Marine and Petroleum Geology, 17(8), 895-907.
22. Haggerty, R., & Gorelick, S. M. (1995). Multiple-rate mass transfer for modeling diffusion and surface reactions in media with pore-scale heterogeneity. Water Resources Research, 31(10), 2383-2400.
23. Haskett, S. E., Narahara, G. M., & Holditch, S. A. (1988). A method for simultaneous determination of permeability and porosity in low-permeability cores. Spe Formation Evaluation, 3(03), 651-658.
24. Haszeldine, S., Lu, J., Wilkinson, M., & Macleod, G. (2006). Long-timescale interaction of CO2 storage with reservoir and seal: Miller and Brae natural analogue fields North Sea. Greenhouse Gas Control Technology, 8
25. Heller, R., Vermylen, J., & Zoback, M. (2014). Experimental investigation of matrix permeability of gas shalesExperimental Investigation of Matrix Permeability of Gas Shales.

Aapg Bulletin, 98(5), 975-995.

26. Hu, Q., Ewing, R. P., & Dultz, S. (2012). Low pore connectivity in natural rock. Journal of Contaminant Hydrology, 133, 76-83. http://doi.org/https://doi.org/10.1016/j.jconhyd.2012.03.006
27. Hu, Q., Ewing, R. P., & Rowe, H. D. (2015). Low nanopore connectivity limits gas production in Barnett formation. Journal of Geophysical Research: Solid Earth, 120(12), 8073-8087. http://doi.org/10.1002/2015JB012103
28. Huenges, E. (2016). Enhanced geothermal systems: Review and status of research and development (743-761). Elsevier.
29. Javadpour, F. (2009). Nanopores and apparent permeability of gas flow in mudrocks (shales and siltstone). Journal of Canadian Petroleum Technology, 48(08), 16-21.
30. Jia, B., Tsau, J., Barati, R., & Zhang, F. (2019). Impact of Heterogeneity on the Transient Gas Flow Process in Tight Rock. Energies, 12(18), 3559.
31. Kamath, J. (1992). Evaluation of accuracy of estimating air permeability from mercury-injection data. Spe Formation Evaluation, 7(04), 304-310.
32. Khosrokhavar, R. (2016). Shale gas formations and their potential for carbon storage: opportunities and outlook. Mechanisms for Co2 Sequestration in Geological Formations and Enhanced Gas Recovery, 67-86.
33. Kim, C., Jang, H., & Lee, J. (2015). Experimental investigation on the characteristics of gas diffusion in shale gas reservoir using porosity and permeability of nanopore scale. Journal of Petroleum Science and Engineering, 133, 226-237. http://doi.org/https://doi.org/10.1016/j.petrol.2015.06.008

34. Kim, J., Kwon, S., Sanchez, M., & Cho, G. (2011). Geological storage of high level nuclear waste. Ksce Journal of Civil Engineering, 15(4), 721-737.
35. Liu, W., Li, Y., Yang, C., Daemen, J. J., Yang, Y., & Zhang, G. (2015). Permeability characteristics of mudstone cap rock and interlayers in bedded salt formations and tightness assessment for underground gas storage caverns. Engineering Geology, 193, 212-223.
36. Lu, J., Wilkinson, M., Haszeldine, R. S., & Fallick, A. E. (2009). Long-term performance of a mudrock seal in natural CO2 storage. Geology, 37(1), 35-38.
37. Luffel, D. L., Hopkins, C. W., & Schettler Jr, P. D. (1993, 1993-1-1). Matrix permeability measurement of gas productive shales. Paper presented at the.
38. Neuzil, C. E. (1986). Groundwater flow in low-permeability environments. Water Resources Research, 22(8), 1163-1195.
39. Neuzil, C. E. (2013). Can shale safely host US nuclear waste? Eos, Transactions American Geophysical Union, 94(30), 261-262.
40. Peng, S., & Loucks, B. (2016). Permeability measurements in mudrocks using gas-expansion methods on plug and crushed-rock samples. Marine and Petroleum Geology, 73, 299-310.
41. Pini, R. (2014). Assessing the adsorption properties of mudrocks for CO2 sequestration. Energy Procedia, 63, 5556-5561.
42. Profice, S., Lasseux, D., Jannot, Y., Jebara, N., & Hamon, G. (2012). Permeability, porosity and klinkenberg coefficien determination on crushed porous media. Petrophysics, 53(06), 430-438.
43. Rasmuson, A. (1985). The effect of particles of variable size, shape and properties on the

dynamics of fixed beds. Chemical Engineering Science, 40(4), 621-629.

44. Roy, S., Raju, R., Chuang, H. F., Cruden, B. A., & Meyyappan, M. (2003). Modeling gas flow through microchannels and nanopores. Journal of Applied Physics, 93(8), 4870-4879.
45. Ruthven, D. M. (1984). Principles of adsorption and adsorption processes. John Wiley & Sons.
46. Ruthven, D. M., & Loughlin, K. F. (1971). The effect of crystallite shape and size distribution on diffusion measurements in molecular sieves. Chemical Engineering Science, 26(5), 577-584.
47. Sutherland, W. (1895). XXXVII. The viscosity of mixed gases. The London, Edinburgh, and Dublin Philosophical Magazine and Journal of Science, 40(246), 421-431.
48. Tarkowski, R. (2019). Underground hydrogen storage: Characteristics and prospects. Renewable and Sustainable Energy Reviews, 105, 86-94.
49. Wu, T., Zhang, D., & Li, X. (2020). A radial differential pressure decay method with micro-plug samples for determining the apparent permeability of shale matrix. Journal of Natural Gas Science and Engineering, 74, 103126.
50. Yang, M., Annable, M. D., & Jawitz, J. W. (2015). Back diffusion from thin low permeability zones. Environmental Science & Technology, 49(1), 415-422.
51. Zhang, J. J., Liu, H., & Boudjatit, M. (2020). Matrix permeability measurement from fractured unconventional source-rock samples: Method and application. Journal of Contaminant Hydrology, 103663.
52. Zhang, T., Hu, Q., Chen, W., Gao, Y., Feng, X., & Wang, G. (2021). Analyses of True-Triaxial Hydraulic Fracturing of Granite Samples for an Enhanced Geothermal System.

Lithosphere, 2021(Special 5)

53. Zhang, T., Zhou, W., Hu, Q., Xu, H., Zhao, J., & Zhang, C. (2021). A pulse-decay method for low permeability analyses of granular porous media: Mathematical solutions and experimental methodologies.

Chapter 4: Shale wettability elucidation using SANS contrast-matching: Heterogeneity and overturning at different pore intervals

Abstract

Wetting properties significantly influence the fluid flow and mass transport in shale, but it is difficult to locally and non-destructively identify the wettability at different sub-nano-pore scales. In this work, based on the small angle neutron scattering (SANS) experiments, a dynamic contrast-matching technique was employed by using various deuterated chemical liquids (hydrophilic, lipophilic, and amphiphilic in nature) for pore-space variation quantification and wettability identification. We report that (1) shale possesses a complex and dynamic wettability for different ranges of pore diameters with a general trend that nanopores are more amiable to oil than water; (2) antecedent contact with a specific liquid could convert the initial wetting status (e.g., from water-wet to oil-wet or vice versa); and (3) a physical matrix expansion & swelling can be induced by the contact with organic solvents, manifesting a changing pore size distribution. The SANS method and contrast- matching technique showcase their practical utilization in elucidating the interplay of pore structure and wetting characteristics in confined nano-pores space.

4.1. Introduction

Fluid flow and mass transport in porous rocks are known to be controlled by their inherent pore structure characteristics (Hu et al., 2015a; Javadpour et al., 2007; Wu et al., 2017). The detailed structural configuration at microscopic and mesoscopic scales, including both geometrical and topological characteristics, are critical to a wide variety of applications of porous materials within the context of energy, resource, and environmental stewardship (Chaudhary et al., 2011; Monge et al., 2017; Speight, 2012). Taking shale as an example, there is an emerging interest in its fluid distribution and flow in nano-confined space around the fine-grained minerals and organic matter (OM). The intrinsic structural characteristics, such as permeability, pore connectivity, and wettability (Loucks et al., 2012; Prakash & Ghosh, 2022), are known to have a profound impact on the energy geosciences and engineering applications of shales, such as sustainable petroleum development and long-term storage performance for gases and nuclear waste (Bustin et al., 2008; Soeder, 1988; Sondergeld et al., 2010). As a result, understanding the microscale wetting properties and its connection with transport behaviors at macroscopic scales is of enormous interest to the emerging fields of unconventional resources and underground carbon/hydrogen storage (Gensterblum et al., 2015a; Hu et al., 2015a; Orangi et al., 2011; Ross & Bustin, 2009).

Small-angle neutron scattering (SANS) is a unique method for wetting behavior characterization of tight porous media (Baker & Heller, 2009; Radliński et al., 2000; Radlinski & Hinde, 2002). The contrast-matching (variation) technique of SANS (Bahadur et al., 2018; Mileeva et al., 2012), for structural studies of multicomponent hydrogen-rich porous systems is particularly advantageous, since additional information about the wettability-related open

pores, microstructurally distorted structure, and chemical sorption can be obtained by labeling the hydrogen atoms of different fluids (gases or liquids) to highlight their scattering contribution and heterogeneous distribution in space (Debye, 1947; Debye et al., 1957). Moreover, because the scattered neutrons in the small angle and ultra-small angle range render a full range of spatial structure information from angstrom to micrometer scales, collectively, they are superior for the total pore space quantification in porous media with a wide range of pore sizes (Brumberger, 2013; Guinier, 1994).

In this work, we start by elucidating the fundamental theory of SANS contrast matching available for hydrocarbon-rich rock, then perform compatible contrast matching experiments using multiple fluids for pore size and wettability characterization. The objectives of this work are to enable a better interpretation of the (U)SANS data to elucidate the complex pore structure and dynamic wetting characteristics at the confined nanopore space of shale.

4.2. Samples and Experiments

Typical lacustrine shale samples from East China were selected for the wetting behavior characterization (Table 1). They were chosen with the same value of vitric reflectance R_o but in different total organic carbon (TOC) under different depths. The information about mineral composition was obtained by X-ray diffraction (XRD), maturity was quantified by microspectrophotometer Model QDI302, and total organic carbon (TOC) was obtained through Leco CS230 Series Carbon/Sulfur Analyzer. The contact angle was measured for wettability using SL200KS automated axisymmetric drop-shape analyzer with the same liquids used for contrast-matching (i.e., hydrophilic fluid – deionized water, lipophilic fluid – a mixture of

decane, and toluene at a volume ratio of 2:1).

Table 1. Samples and their basic properties

Sample ID with depth (m)	R_o[§] (%)	TOC before SE[£] (wt.%)	TOC after SE (wt.%)	Composition[*] (wt.%)							
				Quartz	Ortho clase	Plagio clase	Calcite	Ankerite	Analcime-C	Clays	Pyrite
3825	1.05±0.06	1.07	1.08	12.86	9.89	10.19	6.83	23.15	11.08	24.93	–
4093	1.06±0.07	1.67	1.58	12.68	10.42	23.11	14.36	20.06	–	17.70	–
2964	1.02±0.05	2.91	2.46	11.94	6.12	4.76	15.05	36.21	3.1	19.90	–
4048	1.03±0.06	3.98	2.76	10.66	9.60	20.07	11.62	23.33	–	12.96	0.78

[§] Unit for R_o is the % of reflected light at the specified wavelength from a vitrinite maceral immersed in oil.

[£] SE: solvent extraction. The TOC data for sample 3825 after SE could be abnormal with the slight increase.

[*] Components percentages have been normalized into 100% of volume fraction with the added TOC as volume fraction reflecting the absolute scattering intensity of (U)SANS.

For the SANS tests, data were obtained from SANS beam station at the Chinese Spallation Neutron Source (CSNS) in China, and the BL-6 Extended q-Range (EQ-SANS) Diffractometer at Spallation Neutron Source (SNS) of Oak Ridge National Laboratory (ORNL) in the US. The applied q-range was from 0.0044 to 0.59 $Å^{-1}$, and 0.00429 to 0.74 $Å^{-1}$, respectively. Table 2 presents the contrast matching strategies, showcasing the hydrophilic (deionized water H_2O), lipophilic (n-decane $CH_3(CH_2)_8CH_3$ and toluene C_7H_8 at a volume ratio of 2:1), and amphiphilic (dimethyl methanamide C_3H_7NO) liquids. In this experiment, the volumetric fraction for different liquids was transformed into corresponding mass fraction calculated with their density and weighted by a balance with a resolution of 0.01 mg, for a precise liquid volume control. Hydrophilic, lipophilic, and amphiphilic liquids are abbreviated as H, L, and A. SI is the self-imbibition (spontaneous imbibition of fluid by the porous medium without any external drive) under atmosphere using H, L, and A, while HS is the high-pressure saturation for each liquid. HCS is the process of high-pressure saturation (70 MPa), centrifugation and SI. For example, H-L means that the sample was initially saturated with liquid H under high pressure, centrifuged, and then subjected to SI using liquid L. Meanwhile, the term of solvent extraction

is abbreviated as SE. In Table 2, the mineral composition of the samples is presented both before and after the SE process.

Table 2. Contrast-matching strategies and sample scattering length density (SLD)

Sample ID	Sample SLD ($\times 10^{10}$ cm^{-2})											
	SE	Non-SE	SI			HS			HCS			
	Dry	Dry	H	L	A	H	L	A	H-L	L-H	A-L	A-H
3825	3.9659	3.9473										
4093	4.0631	4.0400										
2964	4.0173	4.0134										
4048	4.1156	4.1124										

For the SLD calculations, as the measure XRD and TOC data is the mass fraction, we transfer their mass fraction into the volume percentage of ϕ_m to be 100% in total using the mineral density. The total SLD of ρ^* can be added by each minerals using the formula of $\rho^* = \sum \rho_m \phi_m$, While ρ_m is the minerals SLD which referred from the NIST website available at https://www.ncnr.nist.gov/resources/activation/. Subsequently, the SLD of the samples will be computed for interpreting the SANS data. Regarding Table 2, the SLD of the dry sample (contrast matching samples) and the SE sample were determined independently.

4.3. Methodologies of contrast matching technique

The zero average contrast-matching technique employs a specific hydrogen-deuterium ratio to mask neutron signals in the connected pore space in the matrix. This technique has been widely used since the 1980s (Hammouda, 2010b; Melnichenko, 2016; Price & Skold, 1987). For structural studies of rocks using contrast-matching of (U)SANS, we are concerned about two aspects of phase state in samples: the space volume and particle size distribution (PSD) of shale. After the contrast-matching, the pore space in samples will be a variable parameter needed for the Deby invariant function calculation.

In 1957, Debye et al. (Debye et al., 1957) introduced the correlation function of $\gamma(r)$ for random scatterers, delineating the scattering length density correlation based on the inverse Fourier transformation of the absolute scattering intensity. The $\gamma(r)$ function can be expressed as the density-density correlation function as Eq. 1A or the inversed Fourier transformation of absolute scattering with $I_A(q) = FT(\gamma(r))$ as Eq. (1B).

$$\gamma(r) = \begin{cases} \frac{1}{V}\int \rho(r')\rho(r'+r)dr' & \text{(A)} \\ \frac{1}{(2\pi)^3}\int I_A(q)\, e^{-iqr} d(q^3) & \text{(B)} \end{cases} \quad (1)$$

where $I_A(q)$ is the absolute scattering intensity, q is the scattering vector, V is the system volume, $\rho(r')$ and $\rho(r)$ is the scattering length density at the point specified by the vector r' and r, respectively.

Then, Debye et al. (1957) elucidated the normalized correlation function of $\gamma_0(r)$ defined as:

$$\gamma_0(r) = \frac{\gamma(r) - \gamma(\infty)}{\gamma(0) - \gamma(\infty)} \quad (2)$$

where $\gamma(\infty)$ denotes the invariant function characterized by two points that are infinitely distant from each other. In Eq. 2, the difference between $\gamma(\infty)$ and $\gamma(0)$, termed as $< \eta^2 >$, can be treated as a invariant parameter and calculated through $< \rho^2 >$ minus $< \rho >^2$. For isotropic system, $< \eta^2 >$ can be expressed in one dimension as Eq. 3

$$< \eta^2 > = \frac{1}{2\pi^2}\int I(q) q^2 dq \quad (3)$$

For the Porod invariant function, the invariant $\overline{\eta^2}$ in Eq. 4 represents the integral of the

intensity over the reciprocal space. $\overline{\eta^2}$ The quantity $\overline{\eta^2}$ represents the second moment of the scattering intensity and is related to the mean square of the Scattering Length Density (SLD, irrespective of the aggregation of pores (Debye et al., 1957).

$$\overline{\eta^2} = \frac{1}{2\pi}\int I_A(q)q^2 = \phi_1\phi_2(\rho_1 - \rho_2)^2 \tag{4}$$

Fig. 1 shows the basic principles of Eq. 4 for volume fraction quantification through the Porod invariant function. ϕ_1 and ϕ_2 in Eq. 4 represent the two phase's volume fraction in the sample, corresponding to the matrix and void space volume of rock, respectively. In the context of the rock system, Fig. 1a displays the sample's pore spaces prior to contrast-matching. In contrast, Fig. 1b showcases the sample post contrast-matching, where the blue-colored pore spaces are filled with the contrast-matching liquid. And the scattering intensity before and after the contrast matching will be measured as $I_{A,1}(q)$ and $I_{A,2}(q)$, respectively.

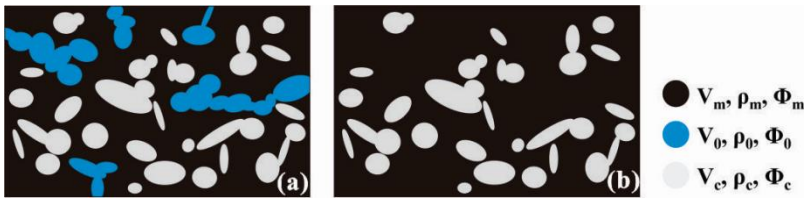

Figure 1. Porod invariant interpretation for different dispersity and volume situations. V_m, V_a, and V_{na} represent the shale matrix, accessible, and non-accessible pore spaces.

Regardless of the deuterated liquid used for liquid immersion, after contrast matching, the sample remains as binary systems being identified by the average SLD difference between the matrix and pore space, as the prerequisite of using the Porod invariant function calculation (Debye et al., 1957; Mastalerz et al., 2012b). In contrast-matching experiments, the unpredictable penetration volume of deuterated liquid complicates SLD determination.

However, the $< \eta^2 >$ will denote us an averaged SLD change before and after contrast matching (named as $< \eta^2 >_b$ and $< \eta^2 >_a$, separately) based on Eq. 3, which can be calculated as:

$$\begin{cases} < \eta^2 >_b = \phi_m(1-\phi_m){\rho_m}^2 \\ < \eta^2 >_a = \phi_{na}(1-\phi_{na})^3{\rho_m}^2 \end{cases} \quad (4)$$

where ϕ is the porosity, ρ is the SLD, the subscript of m, a, and na denote the properties in the matrix, accessible, and non-accessible pore spaces of the rock system, respectively.

From the invariant function of Eq. 4, we can derive Eq. 5 to accurately obtain the deuterated volume of ϕ_a. Among them, we assume $I_{A,1}(q)$ and $I_{A,2}(q)$ were obtained with the same q range and testing conditions (the same wavelength, detector distance setting, and background)

$$\frac{\int I_{A,2}(q)q^2}{\int I_{A,1}(q)q^2} = \frac{\phi_{na}(1-\phi_{na})^3}{\phi_m(1-\phi_m)} \cong \frac{\phi_{na}}{\phi_{na}+\phi_a} \quad (5)$$

For the SLD calculation, we designated the sample's matrix SLD as ρ_m, and treated the SLD of air to be approximately at zero; therefore, the total SLD contrast $\Delta\rho$ will be ρ_m. The average total SLD of ρ^* conforms to the linear superposition as $\rho^* = \sum \rho_i\phi_i$. Here, ϕ_i is the volumetric fraction for each component of shale matrix. After contrast-matching, the volume V_a in Fig. 1a had been saturated with a fraction of ϕ_a, then, based on the equation of $\rho^* = \sum \rho_i\phi_i$, the new average SLD difference between matrix and void space became $\rho^* = \rho_m(1+\phi_a)$, and a precise ϕ_a can be determined from Eq. 5, then the actual SLD can be obtained and used for consequent volume interpretation.

4.4. Results and discussion

4.4.1 Anisotropic analyses

Shale is deposited in anisotropic ways as strata stress for σ_1 (maximum stress), σ_2 (middle stress), and σ_3 (minimum stress) are different with normally $\sigma_1 > \sigma_2 \cong \sigma_3$ (Zhang & Hu et al., 2021b; Zoback et al., 2003). Thus, in terms of pore heterogeneity, for a profile perpendicular (vertical) to the strata layer, pores are hardly rounded in two-dimensions as the compaction is controlled by σ_1; while for direction parallel the layer direction, pores could be more rounded since $\sigma_2 \cong \sigma_3$ (Jaeger et al., 2009; Zoback et al., 2003). The two-dimensional patterns for the four samples depicted in Fig. 2 show structures originating from the rock, either in a vertical (V direction) or parallel (P direction) orientation relative to the bedding layer.

The measuring structure direction has been marked in Fig. 2. The overall trend is that the pore structure from the P direction is less heterogeneous (the two-dimensional data pattern tends to be more rounded) than in the V direction for all four shale samples. Among them, Sample 4093 seems to be the most heterogeneous one for both directions, unlike Sample 4048, which is more homogeneous in the P than V direction as the two-dimensional pattern has been stretched in a more significant way. Moreover, detailed information from the two-dimensional pattern from Sample 3825-V was extracted and shown in Fig. 2a-d. Fig. 2a is the most frequently used SANS scattering curve after the average azimuthal in all directions cross the section. This relies on an assumption of homogeneity for the samples. However, a sliced annulus area (between two white dash lines of Sample 3825-V) shows that the intensity would fluctuate and change to be almost two times larger (from 22 cm^{-1} to 42 cm^{-1}) if the sample exhibits homogeneity in all three dimensions. The scattering intensity in Fig. 6c-d of V and P directions exhibit different curve pattern and fractal (slope) behavior.

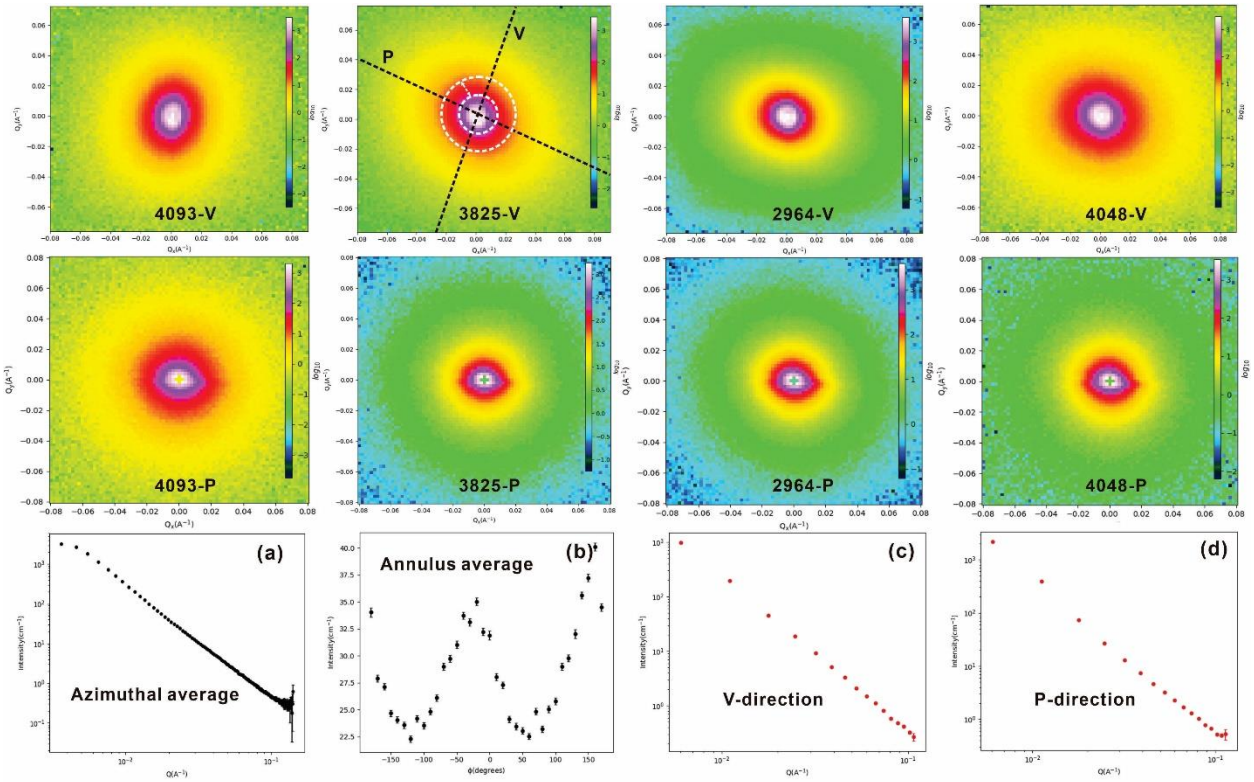

Figure 2. Anisotropic analyses from 1D and 2D scattering patterns of (U)SANS.

4.4.2 Data interpretation and porosity before and after the contrast matching

As aforementioned, four samples were measured with dry, solvent extraction, SI, HS, and HCS states. All the measured data were compiled into Fig. 3a-b. The increased incoherent scattering brings out the effects of the lower fractal dimension in the high q region, as being judged for its smaller slope. Besides, the background after the high-pressure compression (HC) is more obvious than the self-immersion (SI) samples, as the scattering intensity at high q for HC sample exhibits higher intensity compared with SI sample, indicating that more liquids seem to migrate into (smaller) pore spaces.

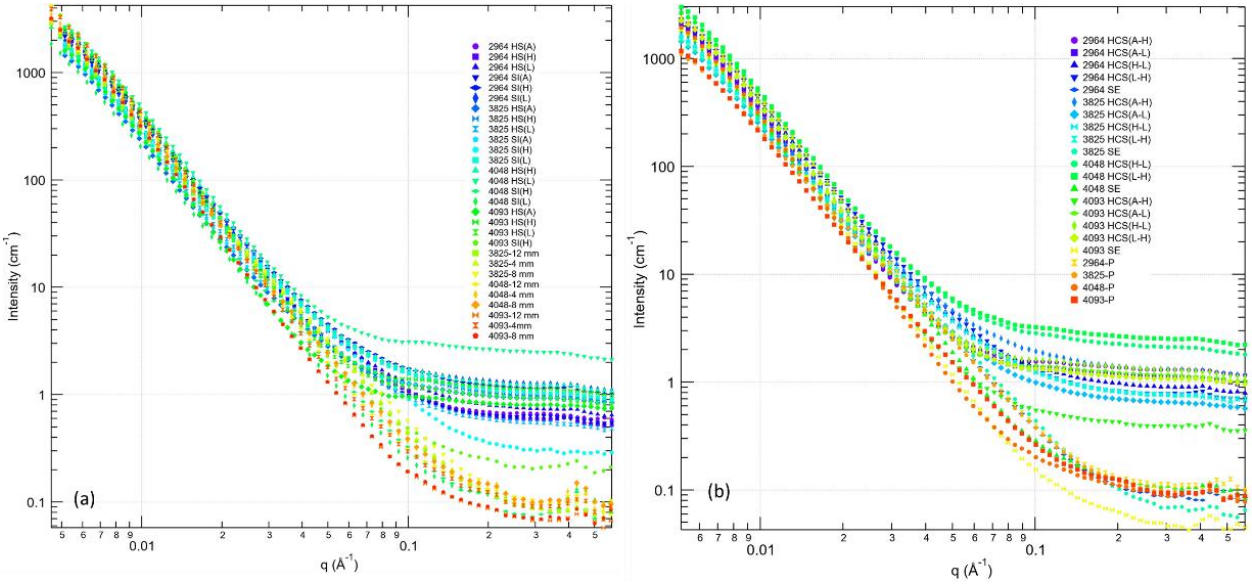

Figure 3. Compiled scattering patterns of SANS for experiments presented in Table 1 for (a) data before centrifugation and the dry sample at different thicknesses in the V direction; and (b) data after centrifugation and for the samples in the P direction after solvent extraction. The contrast-matching increases the incoherent scattering in the background up to ten times, with the background intensity to be 0.1 cm^{-1} for the dry samples, while 1 cm^{-1} for contrast matching samples.

Mathematically, the absolute scattering intensity of $I_A(q)$ in Fig. 3 can be expressed as

$$I_A(q) = \frac{1}{V}\left\langle \left| \sum_{i=1}^{N_p} e^{iq\cdot r_i} \sum_j b_{ij} e^{iq\cdot x_j} \right|^2 \right\rangle \tag{6}$$

where N_p is the total particle number. The position vector r_i and x_j represent the scattering center of particle i, and the particle relative to the scattering center particle i. Terms b is the scattering length for atom j in particle i, and V is the sample volume across the beam. Specifically, vector x_j represents the position information for each single atom in the particle, while r_i detonates the spatial correlation for particles' relative position. For Eq. 6, the form

factor $P(q)$ gives the expression of $\left|\sum_j b_{ij} e^{iq \cdot x_j}\right|^2$ which contains information about the contrast, volume, and shape of particles. While the particles' relative position can be expressed as the structural factor $S(q)$ to represent the summation of $\left|\sum_{i=1}^{N_p} e^{iq \cdot r_i}\right|^2$. Taking the measure absolute intensity into the derived formula of Eq. 5 and using the polydisperse spherical pore model (Radlinski, 2006) in Nika package provided by Jan Ilavsky (Ilavsky, 2012), the porosity was calculated and compiled in the histogram for saturated (Fig. 4) and centrifuged-saturated samples (Fig. 5).

Notably, the porosity depicted in Figs. 4 and 5 corresponds to the liquid non-accessible space of ϕ_{na} as marked in Fig. 1 after the contrast matching (except the dry and solvent-extracted samples), and a smaller porosity value would indicate a better transport ability for a certain liquid. Several features can be revealed from the analyses of the deuterated liquid for L, H, and A immersion test before centrifugation in Fig. 4. First, V-direction samples have a larger representative elemental volume (the smallest volume over which a measurement can be made that will yield a value representative of the whole sample) value (the SANS intensity has been normalized with the sample volume) than the P-direction samples since the P-direction sample porosity is significantly lower than the V-direction samples for 2964, 3825, 4048, and 4093. Secondly, the porosity values for samples are in the order of 2964 > 3825 > 4048 > 4093. The porosity for Samples 2964, 3825, 4048, and 4093 are 7.8%, 4.9%, 4.3%, and 4.0%, with the non-accessible porosity at 51.3%, 57.1%, 37.2%, and 40.0%, respectively. Thirdly, the wettability characteristics of liquid-shale systems exhibit an order of A > L > H, which conforms well to the independent liquid-air contact angle tests that the sample is more amiable

to oil than water as shown in Fig. 6, the contact angle values of H range from 16–76° (typically 16–19°) and L from 13–18°, indicating that these samples are in the intermediate wettability state between water and oil-wet but more towards oil-wet.

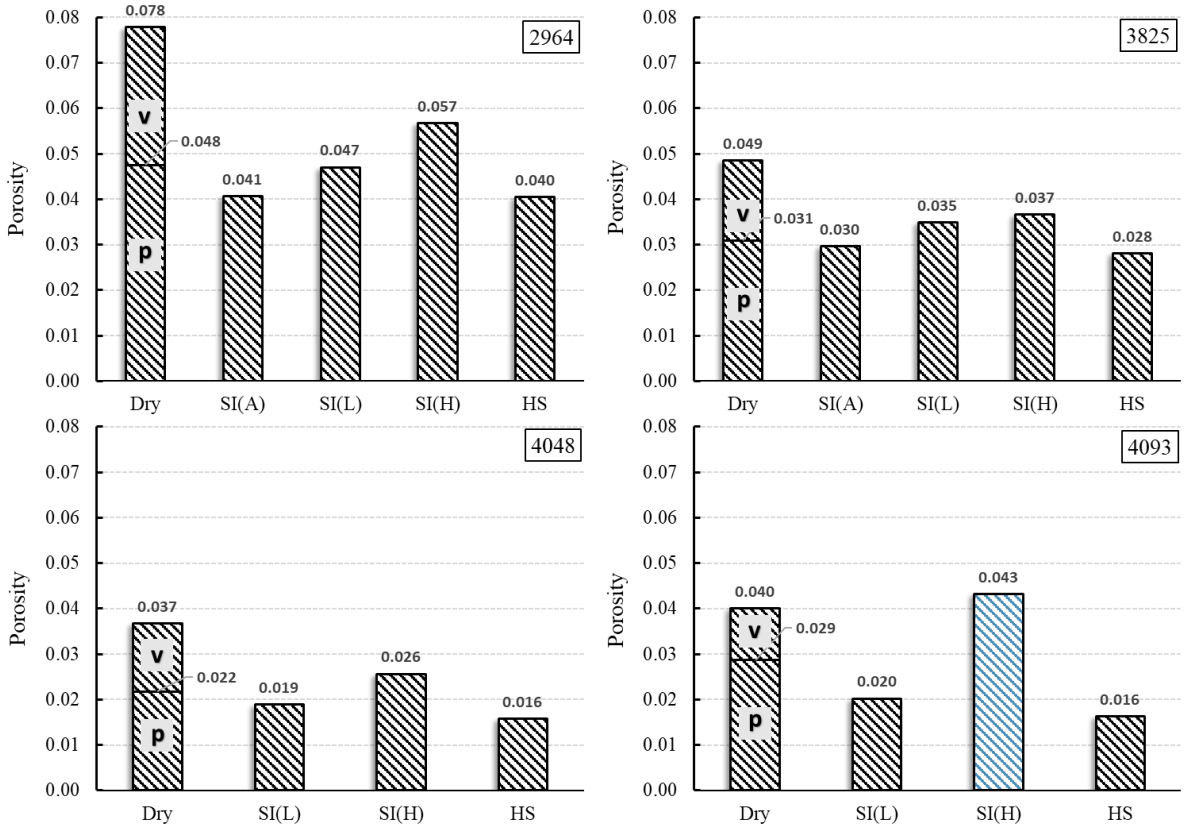

Figure 4. Porosity values for dry and deuterated samples before centrifugation for V and P testing direction. The SI(A), SI(L), SI(H), and HS samples were taken from V-direction. The blue color column shows abnormal data from an exorbitant porosity, which has not been considered for follow-on analyses.

Fig. 5 presents the results of the centrifuged-saturated samples for three distinct deuterated liquids. Notably, SI(A) was compromised for Samples 4048 and 4093 due to sample breakage Meanwhile, no distinct patterns appear for Sample 4093, probably owing to its small porosity value. Two significant conclusions have been made. Firstly, enhancement effects are evident

from the second immersion of HCS(A-L) and HCS(A-H) compared with the first immersion of SI(L) and SI(H). That is, with the pre-existing liquid A, the sample immerses more L and H than in the first SI run, with increases of 2.3% (29.5% of total porosity) for L and 1.9% (24.4% of total porosity) for H in Sample 2964, and increases of 0.5% (10.2% of total porosity) for L and 0.9% (20.0% of total porosity) for H in Sample 3825. Secondly, also the most significant one, is that the pre-existing liquid could play a reversal (overturning) role in the sample's wettability. For example, from the comparison with HCS(H-L) and HCS(A-H) for Samples 2964 and 3825, the sample with liquid H immersed more volume than sample contacted with liquid L, which became more hydrophilic (different from the samples' original wettability) after the H was changed to A while L was changed to H. The results indicate that during the liquid migration in the shale matrix, a pre-contact of the amphiphilic liquid (like using the amphiphilic fracturing fluid) would potentially modify the wettability and hence the movement of hydrophilic and lipophilic liquids in the reservoir; which provide a meaningful potential technique for wettability modification for enhanced oil and gas recovery.

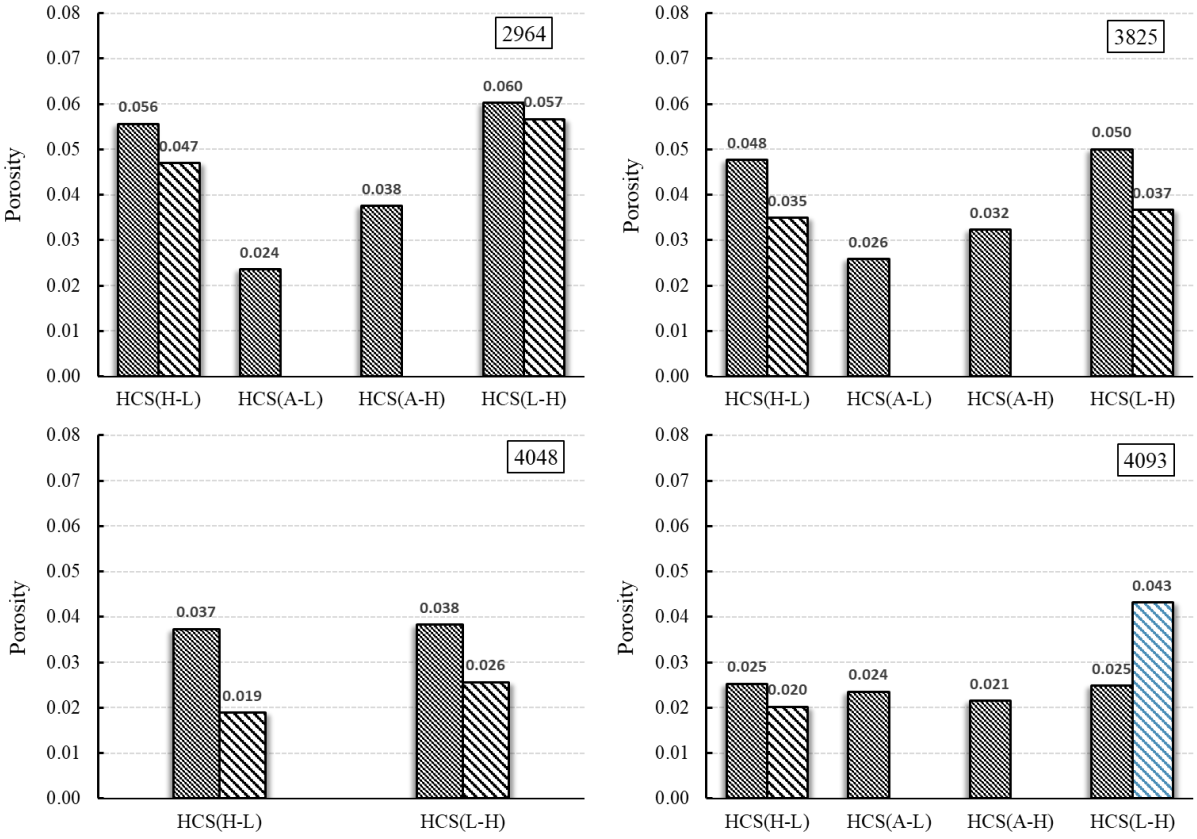

Figure 5. Porosity results for dry and contrast matching samples after centrifugation; the second column in HCS(H-L) and HCS(L-H) is the non-centrifuged value of SI(L) and SI(H) in Fig. 8a. The blue color column shows abnormal data from an exorbitant porosity, which has not been considered for follow-on analyses.

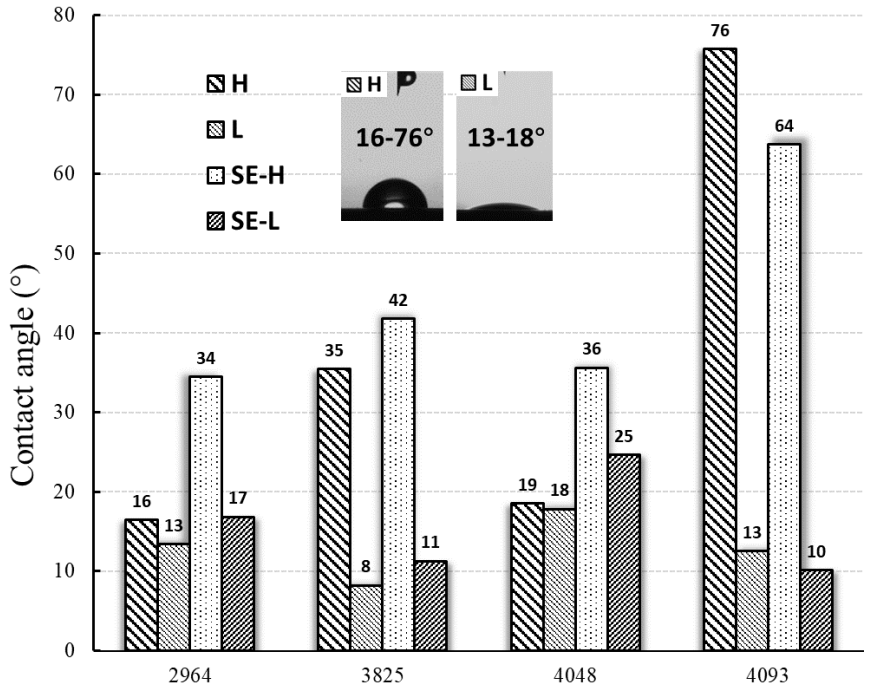

Figure 6. The contact angle for samples tested before and after solvent extraction, using liquids H and L.

4.4.3 Space heterogeneity with different wetting behavior

In this section, we elucidate and interpret porosity across various pore intervals to enhance understanding of fluid distribution and movement heterogeneity in multiphase systems, as illustrated in Figs. 7-8. Fig. 7 shows that, for four samples, the self-immersion of H-liquid tends to appear at the intervals of 5-100 nm, while L-liquid prefers the interval of 50-100 nm. Based on the contact angle analyses, the results for L across the four samples show minimal variation, ranging between 13° and 18°. In contrast, for H-liquid, there is a noticeable difference: Samples 2964 and 4048 register at 16° and 19°, respectively, whereas Samples 3825 and 4093 measure at 35° and 76°, respectively. Since nanopores are predominantly found in the OM, they

facilitate the easy movement of L-liquid into the shale's smaller pores. This results in localized heterogeneity in liquid distribution. Meanwhile, we notice that fluid can be self-migrated into the pore spaces under 20 nm if the sample is strongly wet for fluid L, or even H; on the contrary, after the H-liquid contact angle increases to 35° and 76° for Samples 3825 and 4093, the accessible volume from self-immersion (V_a in Fig. 5) changes dramatically that hardly any fluid movement can be observed at 5-20 nm and also 20-50 nm, where H only appears in pore diameters of 50-100 nm.

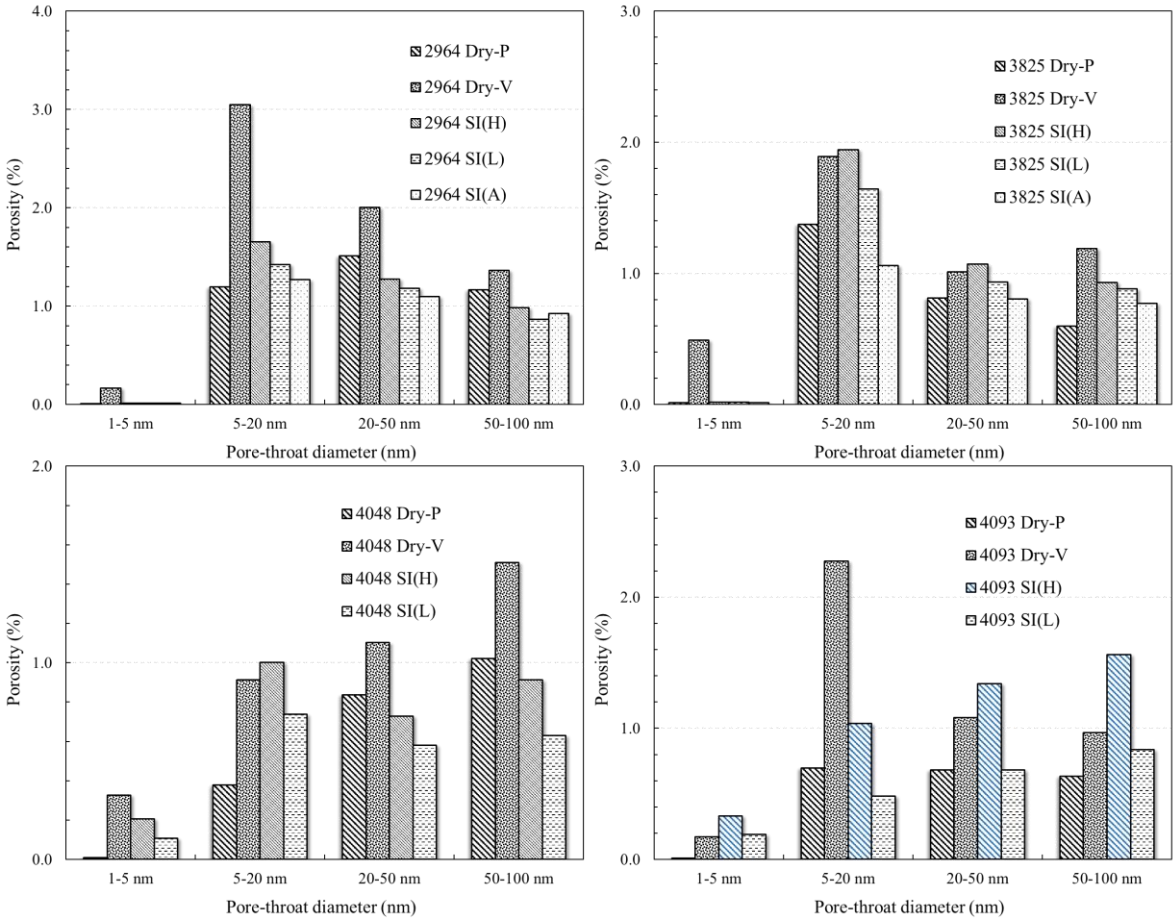

Figure 7. Porosity distribution in the different pore size ranges; some of the SI(H) porosity is slightly higher (less than 0.1%~0.2%) than the dry sample for Samples 3825 and 4048, which will be analyzed

further in section 4.4.3 for swelling mechanism.

The centrifuged-saturated sample exhibits changes in local pore distribution with several notable features. Compared with Fig. 6, more complicated behavior is observed in Fig. 8. After exposure to liquid A, there is a notable increase in fluid immersion compared to the dry sample, particularly in Samples 2964 and 3825. The primary reduction in volume is observed in the 5-20 nm range, which is associated with OM-hosted pores. (Boyd et al., 1988; Tissot et al., 1974). Similar to the phenomena of wettability turn-over between HCS(H-L) and HCS(A-H) for Samples 2964 and 3825, within the 5-20 nm pore diameter range, a significant amount of liquid is absorbed, making HCS(A-H) more receptive than HCS(H-L).

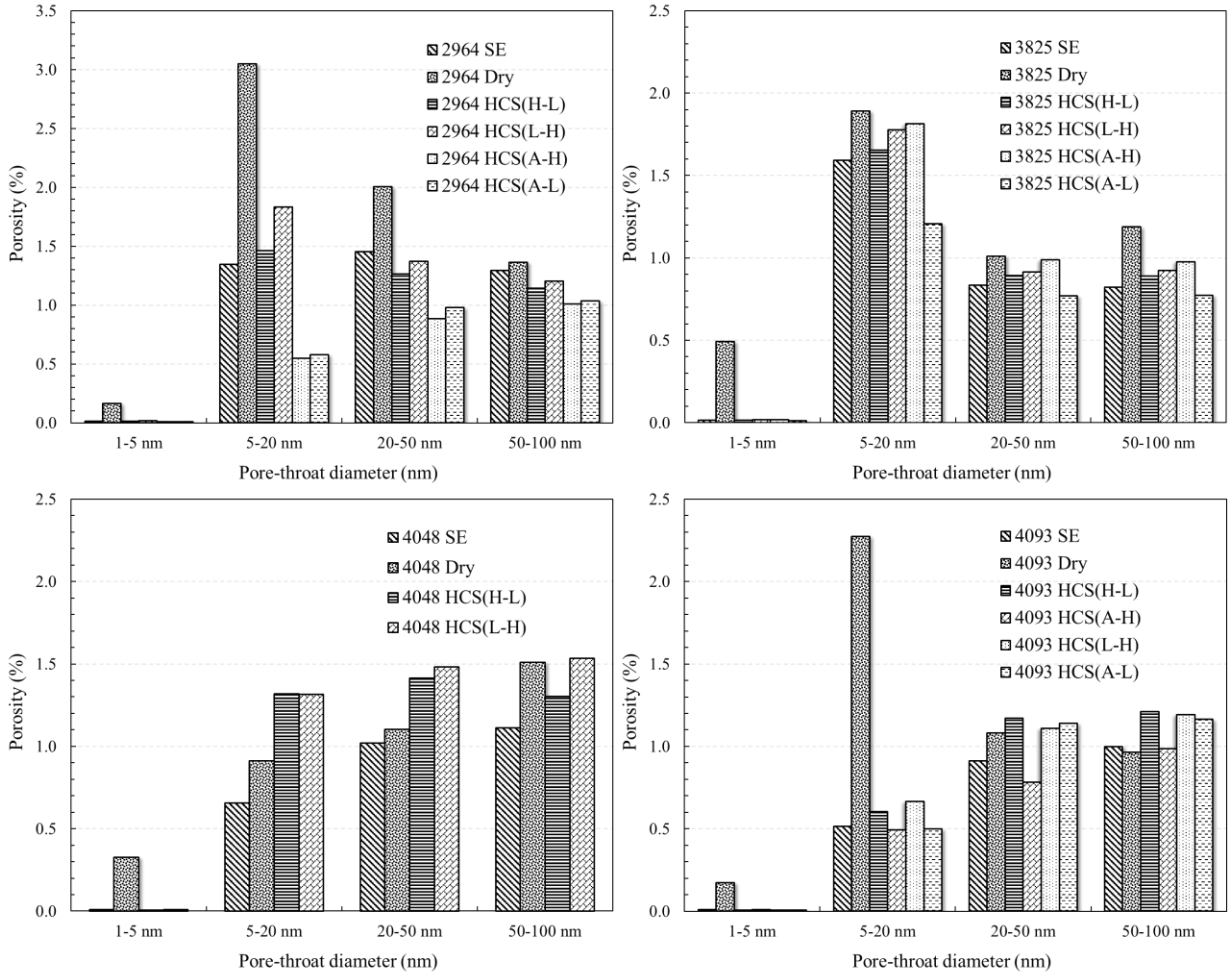

Figure 8. Porosity distribution within the different pore intervals before and after the contrast matching with various liquids.

4.4.3 Wetting mechanism and sample swelling

The wetting behavior characterization is essential in petroleum exploration, especially for shale with mixed wettability at micron scales. Wettability can influence oil production, oil and water ratio, and residual oil saturation at post-production (Roshan et al., 2016; Wu et al., 2017). With multiple wettability concepts, we take the definition from Berg in 1993 (Berg, 1993) that "wettability refers to the response evinced when a liquid is brought into contact with a solid

surface initially in contact with a gas or another liquid," which means that the wettability behavior changes in the process of liquid spreading over the surface, the migration of liquid in the porous medium, and the displacement between liquid (Abdallah et al., 1986; Feder, 2013).

The fluid-solid wetting behavior is different from that in fluid-fluid interactions. Specifically, the primary driving force for two-fluid phase flow in porous media is the capillary force that rises from the surface between the second fluid and the first one, and the pressure difference of the driving force p_1 and p_2 can be expressed as the prominent Eq.(7) (Feder, 2013):

$$|p_1 - p_2| = \sigma(\frac{1}{R_x} + \frac{1}{R_y}) \quad (7)$$

where σ is the surface tension, R_x and R_y are two radii of curvature changing at the pore surface which controlled by contact angle. For a detailed description, see Feder (2013), page 43.

The surface energy is determined by the dispersion (van der Waals) forces for the surface tension, a changing surface tension typically happens with the alteration of the fluid cohesion, for instance, under changing temperature or pressure conditions. However, surface tension is determined by the polarity of leading minerals in the multi-mineral phased shale system, which would be influenced and complicated by the uneven distribution of mineral composition in the local area of micron ranges (Treiber & Owens, 1972). As demonstrated in Figs. 7 and 8, SANS has successfully revealed the dynamic and heterogeneous wetting behavior with the merit of distribution discrimination using contrast matching at the sub-mm sample and down to 1 nm pore-matrix scales.

Besides, sample swelling was observed after solvent extraction and high-pressure saturation,

and we interpret this from two aspects. (We like to emphasize again that the porosity values of HSC or H are the volume of ϕ_a as shown in Fig. 1, only the dry and SE samples represent the actual porosity value.) On the one hand, except for Sample 2964, the HSC values in Fig. 8 closely align with the dry values, more so than the initial SI values presented in Fig. 6. On the other hand, the solvent-extracted porosity is significantly lower than the dry sample, which is contrary to the intuitive. Specifically, the liquid immersed volume is almost close to the total dry porosity, which is unrealistic as approximately 50% of pore spaces are isolated for these four samples. In specific, the new liquid absorbed volume should not exceed the total porosity, owning to the existence of the isolated pores. Thus, the increased ϕ_0, or the decreasing porosity after solvent extraction, indicates a possible matrix swelling in the sample after the solvent extraction and the high-pressure saturation using deuterated liquids. The decreasing porosity of solvent-extracted samples has also been mentioned in previous studies by accounting for the irreversible dilation effect, which tends to happen in shale samples with low TOC and high clay-minerals contents.

The solvent extraction treatment will mobilize the saturated, aromatic, resin, and asphaltene in shale samples (DiStefano et al., 2016). However, no consistent formula for asphaltene has been put forward in the literature which bring the difficulties for the SLD calculation, as it contains various components, as shown by previous studies (Adams, 2014; Lagaly et al., 2006; Sheu, 2002). For contrast-matching, samples were immersed in the organic solvent for long hours to days. The soak time for SI of the dry sample and high-pressure saturation was 12 h, while SE was five days. Since a larger C/H ratio will control the SLD more substantially (Radliński et al., 2000). a more prolonged extraction will lead to heavier hydrocarbon with a

large C/H ratio being dissolved and migrated off. However, owing to a low percentage of TOC (except for Sample 4048), the solvent extraction did not mobilize much OM, as evidenced by the TOC results post-SE presented in Table 1. Thus, the OM percentage has not changed much, and samples remained with roughly the same SLD value before and after the solvent extraction. However, it is certain that the long duration and high-pressure condition of the sample and organic solvent contact lead to the phenomena of sample dilation. We attribute the dilation to matrix dilation manners of clay minerals and describe the dilation from physical and chemical reactions aspects as discussed below.

The physical interactions between clays and the organic solvent can be categorized into three aspects (DiStefano et al., 2016; Kowalska et al., 1994). The first one is organic adsorption, which is controlled by Coulombic forces and shown in the interlayer of clay minerals as intercalation (Jaynes & Boyd, 1990; Kowalska et al., 1994). The second is the polar interactions induced by hydrogen bonding and governed by electrons (DiStefano et al., 2016). While the third one is the hydrophilicity of bentonite group clays and their expansion when exposed to water. The reduced fluid movement in HCS(H-L) compared to HCS(A-L) can be attributed to the third mechanism. This mechanism posits that water molecules surround the cations situated between mineral strata and attached to the outer surfaces of clays. These embedded water molecules, by coordinating with metal cations, influence the electron transfer mechanisms, potentially hindering the interactions between clays and organic solvents. (DiStefano et al., 2016). In addition to the physical reactions, the chemical reaction principles (Kowalska et al., 1994) between clays and organic solvent are described as (1) complex molecular structure, such as weight and chain length, (2) multiple functional groups present in the organic molecules,

such as hydrophobic groups, positively charged groups, negatively charged groups, electronegative groups, and pi bonds, and (3) configuration of the organic molecules (e.g., kerogen, bitumen, hydrocarbons) and aqueous phase as presented by Kowalska et al. (1994) (Kowalska et al., 1994). Based on the physical and chemical reaction principles, the partial dissolution of OM will occur which will result in a smaller pore diameter or even a variation of the PSD due to the matrix dilation as observed by DiStefano et al. in 2016 (DiStefano et al., 2016), with the physical mechanism is the essential reason for causing the decreased porosity after solvent extraction or the HCS operation.

4.5. Conclusions

Nanopore structure and wettability is of great significant for fluid distribution and movement in confined pore space of shale. Based on the (U)SANS method and contrast-matching technique, we investigated shale pore structure and wettability using multiple wetting fluids with sophisticated testing strategies. The theoretical principles of SANS applicable for hydrogen-rich geological media were discussed together with the Debye invariant function.

From the analyses, the researched shale samples show a complex wetting behavior. Specifically, distinct wettability has been observed across different pore ranges, manifesting intricate wetting characteristics.; and the antecedent wetting status can be converted (changing from water-wet to oil-wet or vice versa) because of subsequent liquid contact. Besides, swelling of the shale matrix could change the PSD, which is mainly induced by physical interaction of fluid-shale. The overall trend is that nanopores (especially for 5-20 nm) are more wettable for oil than water. The pre-existing liquid film is essential in reinforcing or converting the

wettability of original sample, indicating a practical application for petroleum recovery. Also, shales show complicated and heterogeneous wetting behavior, such as that the strongly hydrophilic & lithophilic samples, and strongly hydrophilic & weakly lithophilic samples behave differently at different pore ranges after liquid immersion.

References

1. Abdallah, W., Buckley, J. S., Carnegie, A., Edwards, J., Herold, B., Fordham, E., Graue, A., Habashy, T., Seleznev, N., & Signer, C. (1986). Fundamentals of wettability. Technology, 38(1125-1144), 268.
2. Adams, J. J. (2014). Asphaltene adsorption, a literature review. Energy & Fuels, 28(5), 2831-2856.
3. Bahadur, J., Ruppert, L. F., Pipich, V., Sakurovs, R., & Melnichenko, Y. B. (2018). Porosity of the Marcellus Shale: A contrast matching small-angle neutron scattering study. International Journal of Coal Geology, 188, 156-164.
4. Baker, G. A., & Heller, W. T. (2009). Small-angle neutron scattering studies of model protein denaturation in aqueous solutions of the ionic liquid 1-butyl-3-methylimidazolium chloride. Chemical Engineering Journal, 147(1), 6-12.
5. Benmouna, M., & Hammouda, B. (1997). The zero average contrast condition: Theoretical predictions and experimental examples. Progress in Polymer Science, 22(1), 49-92.
6. Berg, J. (1993). Wettability. CRC Press.
7. Boyd, S. A., Lee, J., & Mortland, M. M. (1988). Attenuating organic contaminant mobility by soil modification. Nature, 333(6171), 345-347.
8. Brumberger, H. (2013). Modern aspects of small-angle scattering (Vol. 451). Springer Science & Business Media.
9. Bustin, R. M., Bustin, A. M., Cui, A., Ross, D., & Pathi, V. M. (2008, 2008-1-1). Impact of shale properties on pore structure and storage characteristics. Paper presented at the.
10. Chaudhary, A. S., Ehlig-Economides, C., & Wattenbarger, R. (2011, 2011-1-1). Shale oil

production performance from a stimulated reservoir volume. Paper presented at the.

11. Debye, P. (1947). Molecular-weight determination by light scattering. The Journal of Physical Chemistry, 51(1), 18-32.
12. Debye, P., Anderson, H. R., & Brumberger, H. (1957). Scattering by an Inhomogeneous Solid. II. The Correlation Function and Its Application. Journal of Applied Physics, 28(6), 679-683. http://doi.org/10.1063/1.1722830
13. DiStefano, V. H., McFarlane, J., Anovitz, L. M., Stack, A. G., Gordon, A. D., Littrell, K. C., Chipera, S. J., Hunt, R. D., Lewis Sr, S. A., & Hale, R. E. (2016). Extraction of organic compounds from representative shales and the effect on porosity. Journal of Natural Gas Science and Engineering, 35, 646-660.
14. Feder, J. (2013). Fractals. Springer Science & Business Media.
15. Gensterblum, Y., Ghanizadeh, A., Cuss, R. J., Amann-Hildenbrand, A., Krooss, B. M., Clarkson, C. R., Harrington, J. F., & Zoback, M. D. (2015). Gas transport and storage capacity in shale gas reservoirs–A review. Part A: Transport processes. Journal of Unconventional Oil and Gas Resources, 12, 87-122.
16. Guinier, A. (1994). X-ray diffraction in crystals, imperfect crystals, and amorphous bodies. Courier Corporation.
17. Hammouda, B. (2010). Analysis of the Beaucage model. Journal of Applied Crystallography, 43(6), 1474-1478.
18. Hu, Q., Ewing, R. P., & Rowe, H. D. (2015). Low nanopore connectivity limits gas production in Barnett formation. Journal of Geophysical Research: Solid Earth, 120(12), 8073-8087. http://doi.org/10.1002/2015JB012103

19. Ilavsky, J. (2012). Nika: software for two-dimensional data reduction. Journal of Applied Crystallography, 45(2), 324-328.
20. Jaeger, J. C., Cook, N. G., & Zimmerman, R. (2009). Fundamentals of rock mechanics. John Wiley & Sons.
21. Javadpour, F., Fisher, D., & Unsworth, M. (2007). Nanoscale gas flow in shale gas sediments. Journal of Canadian Petroleum Technology, 46(10)
22. Jaynes, W. F., & Boyd, S. A. (1990). Trimethylphenylammonium-smectite as an effective adsorbent of water soluble aromatic hydrocarbons. Journal of the Air & Waste Management Association, 40(12), 1649-1653.
23. Kowalska, M., Güler, H., & Cocke, D. L. (1994). Interactions of clay minerals with organic pollutants. Science of the Total Environment, 141(1-3), 223-240.
24. Lagaly, G., Ogawa, M., & Dékány, I. (2006). Clay mineral organic interactions. Developments in Clay Science, 1, 309-377.
25. Loucks, R. G., Reed, R. M., Ruppel, S. C., & Hammes, U. (2012). Spectrum of pore types and networks in mudrocks and a descriptive classification for matrix-related mudrock pores. Aapg Bulletin, 96(6), 1071-1098.
26. Mastalerz, M., He, L., Melnichenko, Y. B., & Rupp, J. A. (2012). Porosity of coal and shale: Insights from gas adsorption and SANS/USANS techniques. Energy & Fuels, 26(8), 5109-5120.
27. Melnichenko, Y. B. (2016). Small-Angle Scattering from Con ned and Interfacial Fluids. Springer.
28. Mileeva, Z., Ross, D. K., Wilkinson, D., King, S. M., Ryan, T. A., & Sharrock, H. (2012).

The use of small angle neutron scattering with contrast matching and variable adsorbate partial pressures in the study of porosity in activated carbons. Carbon, 50(14), 5062-5075.

29. Monge, M., Gil-Alana, L. A., & de Gracia, F. P. (2017). US shale oil production and WTI prices behaviour. Energy, 141, 12-19.
30. Orangi, A., Nagarajan, N. R., Honarpour, M. M., & Rosenzweig, J. (2011, 2011-1-1). Unconventional shale oil and gas-condensate reservoir production, impact of rock, fluid, and hydraulic fractures. Paper presented at the.
31. Prakash, R., & Ghosh, S. (2022). Effect of jump in wettability on the hydrodynamics of liquid–liquid two-phase flow in a straight mini capillary tube. Chemical Engineering Journal, 435, 135194.
32. Price, D., & Skold, K. (1987). Neutron scattering. Academic Press.
33. Radlinski, A. P. (2006). Small-angle neutron scattering and the microstructure of rocks. Reviews in Mineralogy and Geochemistry, 63(1), 363-397.
34. Radliński, A. P., Boreham, C. J., Lindner, P., Randl, O., Wignall, G. D., Hinde, A., & Hope, J. M. (2000). Small angle neutron scattering signature of oil generation in artificially and naturally matured hydrocarbon source rocks. Organic Geochemistry, 31(1), 1-14. http://doi.org/https://doi.org/10.1016/S0146-6380(99)00128-X
35. Radlinski, A. P., & Hinde, A. L. (2002). Small angle neutron scattering and petroleum geology. Neutron News, 13(2), 10-14. http://doi.org/10.1080/10448630208218477
36. Roshan, H., Al-Yaseri, A. Z., Sarmadivaleh, M., & Iglauer, S. (2016). On wettability of shale rocks. Journal of Colloid and Interface Science, 475, 104-111.
37. Ross, D. J. K., & Bustin, R. M. (2009). The importance of shale composition and pore

structure upon gas storage potential of shale gas reservoirs. Marine and Petroleum Geology, 26(6), 916-927. http://doi.org/10.1016/j.marpetgeo.2008.06.004

38. Sheu, E. Y. (2002). Petroleum asphaltene properties, characterization, and issues. Energy & Fuels, 16(1), 74-82.
39. Soeder, D. J. (1988). Porosity and permeability of eastern Devonian gas shale. Spe Formation Evaluation, 3(1), 116-124.
40. Sondergeld, C. H., Ambrose, R. J., Rai, C. S., & Moncrieff, J. (2010, 2010-1-1). Micro-structural studies of gas shales. Paper presented at the.
41. Speight, J. G. (2012). Shale oil production processes. Gulf Professional Publishing.
42. Tissot, B., Durand, B., Espitalie, J., & Combaz, A. (1974). Influence of nature and diagenesis of organic matter in formation of petroleum. Aapg Bulletin, 58(3), 499-506.
43. Treiber, L. E., & Owens, W. W. (1972). A laboratory evaluation of the wettability of fifty oil-producing reservoirs. Society of Petroleum Engineers Journal, 12(06), 531-540.
44. Wu, K., Chen, Z., Li, J., Li, X., Xu, J., & Dong, X. (2017). Wettability effect on nanoconfined water flow. Proceedings of the National Academy of Sciences, 114(13), 3358-3363.
45. Zhang, T., Hu, Q., Chen, W., Gao, Y., Feng, X., & Wang, G. (2021). Analyses of True-Triaxial Hydraulic Fracturing of Granite Samples for an Enhanced Geothermal System. Lithosphere, 2021(Special 5)
46. Zoback, M. D., Barton, C. A., Brudy, M., Castillo, D. A., Finkbeiner, T., Grollimund, B. R., Moos, D. B., Peska, P., Ward, C. D., & Wiprut, D. J. (2003). Determination of stress orientation and magnitude in deep wells. International Journal of Rock Mechanics and

Mining Sciences, 40(7-8), 1049-1076.4

Chapter 5: Conclusions

This dissertation presents the poromechanics studies of rock media regarding the rock properties of wettability, permeability, and failure behavior under fluid-solid coupling processes. Chapter 2 provides analyses of true-triaxial hydraulic fracturing of granite samples for an enhanced geothermal system to describe the methodologies for true triaxial hydraulic fracturing tests, the thermal behavior and hydraulic properties of samples, and the thermal effects & indoor experimental indication for field development. Chapter 3 presents an integrated technique for rapid gas permeability measurement of tight rock media, by discussing the mathematical solutions for gas permeability of granular samples, practical usages of algorithms for the Gas Permeability Tester (GPT), and the influence of kinetic energy on gas transport behavior. Chapter 4 delves into the elucidation of shale wettability using Small Angle Neutron Scattering (SANS) contrast-matching to investigate the heterogeneity and overturning at different pore intervals, providing insights into the anisotropic analyses, porosity before and after the contrast matching, and space heterogeneity with different wetting behavior. In summary, the integrated research presented in this dissertation contributes to the improved understanding of complex rock systems.

For future studies, the jump discontinuity phenomena and the permeability scale dependent effect will be analyzed based on the continuum mechanism. Moreover, the combined (U)SANS with the self-designed high-pressure cell will be used to perform the poroelastic study regarding the fluid-solid coupling process, for the better understanding of fracture abundant matrix properties during the hydraulic fracturing.